

Multimodal approach for the numerical simulation of
ultrasonic guided waves in cylindrical structures of
non-constant thickness

Christian Höhne

October 16, 2016

Multimodal approach for the numerical simulation of
ultrasonic guided waves in cylindrical structures of
non-constant thickness

Von der Fakultät für Maschinenbau, Elektro- und Energiesysteme
der Brandenburgischen Technischen Universität Cottbus-Senftenberg
zur Erlangung des akademischen Grades eines

Doktors der Ingenieurwissenschaften

genehmigte Dissertation

vorgelegt von:

Diplom Physiker

Christian Höhne

geboren am 27.7.1983 in Luckenwalde

Vorsitzender: Dr.-Ing. Bernd Beirow

Gutachter: Prof. Dr.-Ing. Ennes Sarradj

Gutachter: Univ. Prof. Dipl.-Ing. Dr. techn. Manfred Kaltenbacher

Tag der mündlichen Prüfung: 29.09.2016

Acknowledgement

The research described in this thesis was conducted at the Federal Institute for Materials Research and Testing (Bundesanstalt für Materialforschung und -prüfung) BAM Berlin.

First and foremost I want to express my gratitude to Prof. Dr.-Ing. Ennes Sarradj from the TU-Berlin (formerly working at the BTU-Cottbus) for supporting the submission of this thesis and agreeing to become my doctorate supervisor as well as Univ. Prof. Dipl.-Ing. Dr. techn. Manfred Kaltenbacher from the TU-Wien for acting as second reviewer of this thesis and Dr.-Ing. Bernd Beirow from the BTU-Cottbus for accepting to be the chairman of the Board of Examiners.

Furthermore, I would like to thank my supervisor at the Federal Institute for Materials Research and Testing Dr.-Ing. Jens Prager for his support throughout this research project as well as his helpful suggestions and remarks regarding this thesis and Dr. rer. nat. Hauke Gravenkamp for various valuable discussions during the course of this work which contributed greatly to further improvements.

I thank Prof. Dr. rer. nat. habil. Marc Kreutzbruck and Dipl.-Ing. Thomas Heckel for giving me the chance to conduct this research project at the Federal Institute for Materials Research and Testing and lending their continuous support.

My colleagues M.Sc. Fabian Krome and Dipl.-Phys. Maxim Daschewski deserve special acknowledgement for interesting exchanges of knowledge on various topics.

Last but not least, I would like to thank my parents Marion Höhne and Hans-Jürgen Höhne for all their support and continuous encouragement throughout my academic career up to this point.

Abstract

Guided waves hold great potential for applications in the field of ultrasonic nondestructive testing. Examples of possible applications are the ultrasonic testing and structural health monitoring of wheelset-axles as used in trains. Depending on the particular type, these axles can be described as either thick cylindrical rods or thick walled hollow cylinders with varying thickness.

Wheelset-axles are safety relevant components that have to be inspected on a regular basis. The use of guided waves would allow a full inspection while accessing only the front faces of the axle, thus potentially speeding up the inspection procedure. In order to develop such an inspection technique, however, detailed knowledge of wave propagation through the axle is required.

Established mesh-based procedures, like the finite element method, could be used to simulate guided wave propagation in such structures. However, due to the size of the axle itself and the comparatively fine mesh that is dictated by the wavelengths usually applied in ultrasonic testing, these mesh-based procedures would be very expensive in terms of computation times. The multimodal approach seems to be a very promising alternative that can be expected to provide results significantly faster.

The multimodal method uses the guided wave modes of a corresponding waveguide with a constant cross-section as basis in which the local sound field at any given position in a waveguide with varying thickness can be expressed. Thereby the numerical effort is reduced to solving the one dimensional differential equations that govern the evolution of the coefficients in the mode spectrum along the waveguide. Once the sound field has been calculated, a time dependence can easily be included, which allows the simulation of pulse propagation through the waveguide.

In this thesis, the multimodal approach, as described for the calculation of Lamb-waves in plates with non-constant thickness, is extended to other types of elastic waveguides such as cylindrical rods and thick walled hollow cylinders. For the sake of simplicity, investigations are restricted to axially symmetric wave modes. The results obtained with the multimodal approach are validated against FEM-simulations. It is shown that the multimodal method potentially holds a great advantage in terms of computation time over commercially available software based on the finite element method. Finally, the multimodal method is evaluated with respect to possible future applications on wheelset-axles.

Zusammenfassung

Geführte Wellen besitzen ein großes Potential für Anwendungen im Bereich der zerstörungsfreien Ultraschallprüfung. Beispiele möglicher Anwendungen sind die Ultraschallprüfung oder Zustandsüberwachung von Radsatzwellen, wie sie in Zügen verwendet werden. Abhängig vom jeweiligen Typ können diese Radsatzwellen als Vollzylinder oder dickwandige Hohlzylinder beschrieben werden.

Radsatzwellen sind sicherheitsrelevante Bauteile, die regelmäßig geprüft werden müssen. Die Verwendung geführter Wellen würde ausgehend von den Stirnflächen eine Prüfung des gesamten Bauteilvolumens ermöglichen. Dieser Umstand kann potentiell verwendet werden um den Prüfprozess zu beschleunigen. Zur Entwicklung eines entsprechenden Prüfverfahrens sind jedoch Kenntnisse über die Details der Ausbreitung geführter Wellen innerhalb der Radsatzwellen notwendig.

Etablierte Verfahren, wie die Finite-Elemente-Methode, können für die Simulation der Ausbreitung geführter Wellen in derartigen Strukturen verwendet werden. Aufgrund der Abmessungen der Radsatzwelle, der in der Ultraschallprüfung gebräuchlichen Wellenlängen und der sich daraus ergebenden notwendigen Größe und Anzahl der Elemente, wäre dabei allerdings mit einem großen Zeitaufwand zu rechnen. Der Multimodalansatz scheint eine vielversprechende Alternative darzustellen, welche im Stande ist Simulationen wesentlich schneller durchzuführen.

Die Multimodalansatz basiert darauf, das lokale Schallfeld in einem Wellenleiter variierender Dicke in einer Basis von geführten Wellenmoden eines korrespondierenden Wellenleiters konstanter Dicke darzustellen. Der numerische Aufwand reduziert sich dadurch auf die Lösung der eindimensionalen Differenzialgleichungen, welche die Entwicklung der Koeffizienten im Modenspektrum entlang des Wellenleiters beschreiben. Nachdem das Schallfeld bestimmt wurde, kann der Lösung mit geringem Aufwand eine Zeitabhängigkeit hinzugefügt werden, was die Simulation der Ausbreitung von Ultraschallpulsen durch den Wellenleiter ermöglicht.

In der vorliegenden Dissertation wird ein Multimodalansatz zur Bestimmung von Lamb-Moden in Platten nicht-konstanter Dicke auf andere Arten elastischer Wellenleiter, wie Vollzylinder und dickwandige Hohlzylinder, erweitert. Zur Vereinfachung der notwendigen Herleitungen wird dabei eine Einschränkung auf axialsymmetrische Moden getroffen. Die Ergebnisse werden durch Vergleich mit FEM-Simulationen validiert. Es wird gezeigt, dass der Multimodalansatz in Bezug auf die benötigte Rechenzeit potentiell große Vorteile gegenüber, auf der Finiten-Elemente Methode basierender, kommerziell verfügbarer Software bietet. Abschließend wird der Multimodalansatz in Hinblick auf mögliche zukünftige Anwendungen in Bezug auf Radsatzwellen bewertet.

Contents

1	Introduction	3
1.1	Motivation	3
1.2	Problem	4
1.3	Contribution of this thesis	5
2	Theory and Fundamentals	7
2.1	Guided waves in plates and cylinders	7
2.1.1	Displacement and stress in plates	7
2.1.2	Displacement and stress in cylindrical rods	11
2.1.3	Displacement and stress in hollow cylinders	13
2.2	The effect of a varying cross-section	15
2.3	Concept of the multimodal method	16
2.4	Determination of complex wave numbers	17
2.4.1	Spectral decomposition for symmetric Lamb-waves	20
2.4.2	Spectral decomposition for antisymmetric Lamb-waves	21
2.4.3	Computing the dispersion curves	21
3	Implementation for plates	25
3.1	Plates with symmetrically and asymmetrically varying thickness	25
3.2	Solving the differential equations	30
3.2.1	Transforming the coupled differential equations	30
3.2.2	Solving the Riccati matrix differential equation	31
3.2.3	Solving the linear differential equation	33
3.3	On the accuracy of wave numbers	33
3.3.1	Estimate of relative error	33
3.3.2	Anomaly in the modes of lowest order	34
3.3.3	Achieving the required accuracy	34
3.4	Concerning Cutoffs	35
3.4.1	Regular Cutoffs	36
3.4.2	Irregular Cutoffs	37
3.5	Pulse Propagation	37
3.6	Reproduction of previously published results	38

4	Adaptation to cylindrical structures	41
4.1	Dispersion relations of axially symmetric guided waves	41
4.1.1	Cylindrical rods	42
4.1.2	Hollow cylinders	43
4.2	Multimodal method	45
4.2.1	Cylindrical rods	47
4.2.2	Hollow cylinders	50
5	Simulation results	55
5.1	Plates	55
5.1.1	Plates with symmetrically varying thickness	55
5.1.2	Plates with asymmetrically varying thickness	59
5.2	Cylindrical rods	60
5.3	Hollow cylinders	66
5.4	Efficiency compared to FEM	69
5.4.1	Simulations in plates	70
5.4.2	Simulations in cylindrical rods	71
6	Conclusions and future work	73
6.1	Evaluation of the multimodal approach	73
6.2	Possible application in structural health monitoring and non-destructive testing of wheelset-axles	75
6.3	Outlook	77
A	Dispersion relation of hollow cylinders	79
B	Derivation of matrix elements in N_1 and N_4	81
B.1	Plates	81
B.2	Cylindrical rods	85
B.3	Hollow Cylinders	89
C	Analytical expressions for Q_1 and Q_2	95
	Nomenclature	97
	Bibliography	101
	List of publications from this work	107
	List of Figures	109
	List of Tables	113

Chapter 1

Introduction

1.1 Motivation

Wheelset-axles as used in trains are safety relevant components that have to be inspected on a regular basis. Ultrasonic inspection of wheelset axles carried out by manual scanning on a non dismantled set of axles usually takes up to two hours [1]. Over the last ten years, automated inspection systems have been fielded which make extensive use of phased array probes, thereby improving the inspection quality without further increasing inspection time (see e.g. [2]). However, all of those techniques require to temporarily decommission the entire train in order to access the axles for a full inspection.

The use of guided waves allows the inspection of large volumes of a structure from a single sensor position which holds great potential for applications in ultrasonic testing and structural health monitoring [3–7]. With an inspection technique based on the utilization of guided waves, the entire wheelset-axle could be evaluated accessing only the front faces. This would eliminate the necessity to access the axle over its full length and thus holds great potential for significantly improving the efficiency of the inspection procedure.

In recent years some research on the ultrasonic inspection of wheelset-axles by use of guided waves has been conducted at the Federal Institute for Materials Research and Testing in Berlin, Germany [8–10]. While ultrasonic inspection with guided waves is sensitive to changes within the axle itself, a classification of these changes or defect localization is complicated by the complexity of the measured signals [9, 10]. This complexity arises from the fact that at the frequencies usually used in ultrasonic testing several guided wave modes will be excited as well as from the generally dispersive nature of guided waves. While this can partially be compensated by use of mode selective excitation any advanced inspection technique based on guided waves will require a detailed knowledge of guided wave propagation within the waveguide which has to be obtained by numerical simulations [7]. These simulations would provide the foundation for a modal decomposition of measured signals thus improving the reliability of structural health

monitoring by allowing more advanced algorithms for feature extraction [10].

1.2 Problem

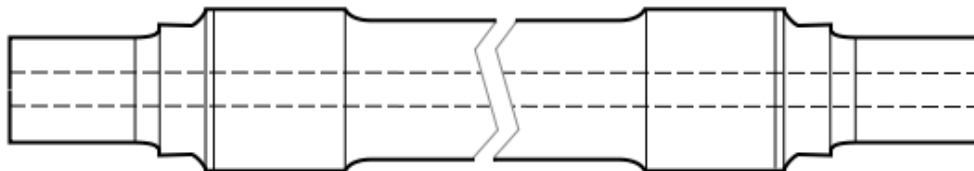


Figure 1.1: General layout of a wheelset-axle as used in trains.

Wheelset-axes can be described as thick walled hollow cylinders with non-constant thickness. The general layout is illustrated in Figure 1.1. As we can see, the axle is in fact a hollow cylinder with constant inner and piecewise constant outer radius with transitions between different outer radii being continuous. At these changes in thickness, a single incident wavemode will couple to other propagating modes [11]. Furthermore, total reflections of modes will occur at cut-off cross-sections i.e. a thickness at which the nature of a particular mode switches from propagating (real wave number) to evanescent (complex wave number) [12]. Because of these properties we can state that guided wave propagation through a wheelset-axle is not trivial and the measured signal that has to be evaluated will have a certain complexity even if perfect mode selective excitation was applied in its initial generation.

Preliminary works on the simulation of guided waves in hollow cylinders showed that the use of commercially available simulation tools based on the Finite Element Method (FEM) for these simulations would be extremely expensive in terms of computation time [8]. This arises from the overall dimension of the axle which is about 2 m in length and several cm thick in combination with comparatively small wavelengths of a few mm which dictate a corresponding mesh size. Since FEM can not be considered to be a suitable method to systematically carry out a large number of numerical simulations of guided wave propagation in wheelset-axes, an alternative approach had to be found.

A significant improvement in terms of efficiency of numerical simulations was achieved with the Scaled Boundary Finite Element Method (SBFEM) which was derived by Song et al. [13–15] and further developed e.g. in the work of Gravenkamp [16]. However, as of now the SBFEM can not be used to simulate waveguides with varying thickness and since the outer radius varies continuously in a wheelset-axle, a simple coupling of several waveguides of different but constant thickness would be insufficient. A promising alternative was presented by Pagneux and Maurel in 2006 [17] with the utilization of a multimodal method to calculate the propagation of Lamb-modes in a plate with symmetrically varying thickness. Since this method reduces the numerical effort to solving a

set of ordinary differential equations along the direction of mode propagation, it can be expected to be significantly faster than any mesh-based approach like FEM. While the multimodal method has been expanded and improved (e.g. [18–25]), the focus of this work was on its use in aeroacoustic applications instead of simulations of wave propagation in elastic waveguides.

1.3 Contribution of this thesis

The main focus of this thesis will be on adapting the multimodal method as described in [17] to cylindrical rods and thick walled hollow cylinders with varying thickness in order to make it applicable to the simulation of ultrasonic guided waves in wheelset-axles. This includes the extension of the multimodal method itself as well as the calculation of complex dispersion curves in these structures.

The remainder of this thesis is structured as follows. Chapter 2 contains a brief summary of the mathematical description of guided waves in plates and cylinders as well as a discussion of the effect of varying cross-sections, the basic ideas of the multimodal method and the procedure used to calculate complex dispersion curves.

In Chapter 3 the implementation for plates with varying thickness will be recapitulated in more detail, highlighting points that require particular attention. Descriptions of the methods used for solving the differential equations, improving the calculated wave numbers to the required accuracy and the treatment of cutoffs will be provided. The implementation is tested by reproducing the simulation results that were published by Pagneux and Maurel in [17].

The adaptation of the multimodal approach and the calculation of complex wave numbers to cylindrical rods and thick walled hollow cylinders will be described in Chapter 4, while simulation results obtained with the multimodal method and their comparison with FEM simulations will be shown in Chapter 5.

Finally an evaluation of the multimodal method, a discussion of remaining open problems and an outlook on possible future development will be given in Chapter 6.

Chapter 2

Theory and Fundamentals

2.1 Guided waves in plates and cylinders

Solving the elastic wave equation for an infinite solid medium (i.e. without applying any boundary conditions) yields solutions for longitudinal and shear waves (see e.g. [26]). If the solid medium is restricted to a finite structure, the geometrical constraints that are imposed on the wave propagation enforce a superposition of vertical and horizontal movements. As a result, depending on frequency, material parameters and boundary conditions, complicated displacement fields are formed which propagate along the structure and are referred to as guided waves [27]. Although the term guided waves is often associated with thin structures (i.e. the thickness being of the same order of magnitude as the wavelength) it should be noted that in principle any set of boundary conditions that does not allow to regard the solid medium as infinite or semi-infinite will impose guided wave solutions on the elastic wave equation.

While early works on wave propagation in cylindrical bars were conducted by Pochhammer [28] and Chree [29], a mathematical description of guided waves in plates, including their dispersion relation, was provided by Horace Lamb in 1917 [30]. Similar descriptions of guided waves have been provided for cylindrical rods (e.g. by Zemanek [31]) and for thick walled hollow cylinders in the works of Gazis [32–34] and Greenspon [35–37]. In this section, we will briefly recapitulate the most important steps in the description of guided waves in these structures.

2.1.1 Displacement and stress in plates

For the mathematical description of Lamb-waves, we will essentially follow the path laid out in [30]. The elastic properties of a linear elastic medium are described by the 4-dimensional ($3 \times 3 \times 3 \times 3$) elastic tensor \mathbf{C} which links the 3×3 stress ($\boldsymbol{\sigma}$) and strain ($\boldsymbol{\epsilon}$) tensor by the generalized Hooke's Law [38]

$$\boldsymbol{\sigma} = \mathbf{C}\boldsymbol{\epsilon}. \tag{2.1}$$

Using symmetries, \mathbf{C} can be written in a simplified 2-dimensional 6×6 representation. For isotropic materials this representation contains only two independent entries and can be written in terms of the Lamé constants λ and μ as

$$\mathbf{C} = \begin{pmatrix} \lambda + 2\mu & \lambda & \lambda & 0 & 0 & 0 \\ \lambda & \lambda + 2\mu & \lambda & 0 & 0 & 0 \\ \lambda & \lambda & \lambda + 2\mu & 0 & 0 & 0 \\ 0 & 0 & 0 & \mu & 0 & 0 \\ 0 & 0 & 0 & 0 & \mu & 0 \\ 0 & 0 & 0 & 0 & 0 & \mu \end{pmatrix}. \quad (2.2)$$

The elements of the stress tensor are defined as

$$\sigma_{ij} = \frac{\text{force in } i\text{-direction}}{\text{area with surface normal in } j\text{-direction}}. \quad (2.3)$$

For a 3-dimensional Cartesian coordinate system this reads

$$\boldsymbol{\sigma} = \begin{pmatrix} \sigma_{xx} & \sigma_{xy} & \sigma_{xz} \\ \sigma_{xy} & \sigma_{yy} & \sigma_{yz} \\ \sigma_{xz} & \sigma_{yz} & \sigma_{zz} \end{pmatrix}. \quad (2.4)$$

The strain tensor is defined as

$$\boldsymbol{\epsilon} = \frac{1}{2} (\text{grad}(\vec{u}) + (\text{grad}(\vec{u}))^T) \quad (2.5)$$

where $\vec{u} = (u_x, u_y, u_z)^T$ denotes the displacement vector. In 3-dimensional Cartesian coordinates (2.5) yields

$$\boldsymbol{\epsilon} = \begin{pmatrix} \epsilon_{xx} & \epsilon_{xy} & \epsilon_{xz} \\ \epsilon_{xy} & \epsilon_{yy} & \epsilon_{yz} \\ \epsilon_{xz} & \epsilon_{yz} & \epsilon_{zz} \end{pmatrix} = \frac{1}{2} \begin{pmatrix} 2\partial_x u_x & \partial_y u_x + \partial_x u_y & \partial_z u_x + \partial_x u_z \\ \partial_x u_y + \partial_y u_x & 2\partial_y u_y & \partial_z u_y + \partial_y u_z \\ \partial_x u_z + \partial_z u_x & \partial_y u_z + \partial_z u_y & 2\partial_z u_z \end{pmatrix}. \quad (2.6)$$

Using (2.2) we can derive the following wave equation for the displacement vector

$$\rho \partial_t^2 \vec{u} = \mu \vec{\nabla}^2 \vec{u} + (\lambda + \mu) \vec{\nabla}(\vec{\nabla} \cdot \vec{u}). \quad (2.7)$$

With the Helmholtz decomposition

$$\vec{u} = \vec{\nabla}\Phi + \vec{\nabla} \times \vec{H} \quad (2.8)$$

equation (2.7) translates into

$$\partial_t^2 \Phi = \frac{\lambda + 2\mu}{\rho} \vec{\nabla}^2 \Phi \quad (2.9)$$

and

$$\partial_t^2 H_j = \frac{\mu}{\rho} \left(\vec{\nabla}^2 \vec{H} \right)_j \quad (2.10)$$

with $j = x, y, z$.

In order to describe the plate we use a plane strain approximation in z -direction thus restricting all further calculations to the xy -plane. Furthermore, we assume x as the direction of wave propagation and position the upper and lower plate surface at $y = h/2 = \bar{h}$ and $y = -h/2 = -\bar{h}$ respectively. The remaining components of the displacement vector follow directly from (2.8)

$$u_x = \partial_x \Phi + \partial_y H_z \quad (2.11)$$

and

$$u_y = \partial_y \Phi - \partial_x H_z. \quad (2.12)$$

As we can see, solving the wave equations for the scalar potential Φ and the z -component of the vector potential \vec{H} will be sufficient. If we assume that the wave is only restricted by the geometric boundaries in y -direction and can otherwise freely propagate in space and time, we can set the time- and x -dependence of Φ and H_z to $e^{i\omega t}$ and e^{ikx} respectively¹. The wave equation (2.9) is then simplified to

$$\partial_y^2 \Phi = \left(k^2 - \frac{\omega^2 \rho}{\lambda + 2\mu} \right) \Phi = (k^2 - k_L^2) \Phi = \bar{\alpha}^2 \Phi \quad (2.13)$$

where k_L denotes the wave number corresponding to the longitudinal wave of an infinite linear elastic medium (see e.g. [26]). The full solution to (2.9) is then described by

$$\Phi = e^{ikx} (A_1 e^{\bar{\alpha}y} + B_1 e^{-\bar{\alpha}y}) e^{i\omega t}. \quad (2.14)$$

A similar calculation yields

$$H_z = e^{ikx} (A_2 e^{\bar{\beta}y} + B_2 e^{-\bar{\beta}y}) e^{i\omega t}. \quad (2.15)$$

with

$$\bar{\beta}^2 = k^2 - k_T^2 = k^2 - \omega^2 \rho / \mu \quad (2.16)$$

where k_T denotes the wave number corresponding to the transverse wave of an infinite linear elastic medium (see e.g. [26]). Using (2.14) and (2.15) in (2.11) and (2.12), we obtain

$$u_x = e^{ikx} \left(ik (A_1 e^{\bar{\alpha}y} + B_1 e^{-\bar{\alpha}y}) + \bar{\beta} (A_2 e^{\bar{\beta}y} - B_2 e^{-\bar{\beta}y}) \right) e^{i\omega t} \quad (2.17)$$

and

$$u_y = e^{ikx} \left(\bar{\alpha} (A_1 e^{\bar{\alpha}y} - B_1 e^{-\bar{\alpha}y}) + ik (A_2 e^{\bar{\beta}y} + B_2 e^{-\bar{\beta}y}) \right) e^{i\omega t}. \quad (2.18)$$

We now follow the procedure given in [30] and divide the solutions into two distinct cases. The first case are solutions where the displacement u_x is symmetric with respect to $y = 0$. These solutions will be referred to as symmetric Lamb-modes or S -modes. The second case are solutions where the displacement u_x is antisymmetric with respect to $y = 0$. These solutions will be referred to as antisymmetric Lamb-modes or A -modes.

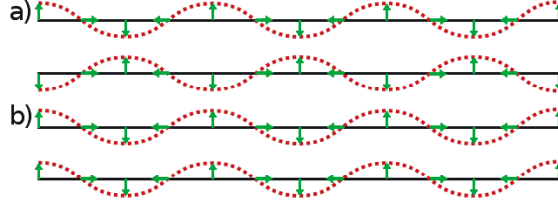


Figure 2.1: Illustration of displacements in a) symmetric Lamb-modes (S -modes) and b) antisymmetric Lamb-modes (A -modes).

Both cases are illustrated in Figure 2.1 with the solid black lines marking the plate surfaces, the dotted red lines illustrating their deformation, the vertical green arrows indicating displacement in y -direction and the horizontal green arrows indicating displacement in x -direction.

For a symmetric displacement field u_x we find $A_1 = B_1 = A$ and $A_2 = -B_2 = B$ and thus for S -modes

$$u_x = (ikA \cosh(\bar{\alpha}y) + \bar{\beta}B \cosh(\bar{\beta}y)) e^{i(kx+\omega t)} \quad (2.19)$$

and

$$u_y = (\bar{\alpha}A \sinh(\bar{\alpha}y) - ikB \sinh(\bar{\beta}y)) e^{i(kx+\omega t)}. \quad (2.20)$$

Using Hooke's Law (2.1) and (2.6), we find the following expressions for those elements of the stress tensor (2.4) which remain under a plane strain approximation

$$\sigma_{xx} = \mu \left(-(k^2 + 2\bar{\alpha}^2 - \bar{\beta}^2)A \cosh(\bar{\alpha}y) + 2ik\bar{\beta}B \cosh(\bar{\beta}y) \right) e^{i(kx+\omega t)} \quad (2.21)$$

$$\sigma_{xy} = \mu \left(2ik\bar{\alpha}A \sinh(\bar{\alpha}y) + (k^2 + \bar{\beta}^2)B \sinh(\bar{\beta}y) \right) e^{i(kx+\omega t)} \quad (2.22)$$

$$\sigma_{yy} = \mu \left((k^2 + \bar{\beta}^2)A \cosh(\bar{\alpha}y) - 2ik\bar{\beta}B \cosh(\bar{\beta}y) \right) e^{i(kx+\omega t)} \quad (2.23)$$

where σ_{xy} and σ_{yy} are stresses on surfaces with surface normal in y -direction. In order to determine the yet unknown coefficients A and B we will use the boundary condition of traction free surfaces meaning that (2.22) and (2.23) have to vanish at $y = \bar{h}$ and $y = -\bar{h}$. The resulting system of equations for A and B can be written in the vectorized form

$$\begin{pmatrix} 2ik\bar{\alpha} \sinh(\bar{\alpha}\bar{h}) & (k^2 + \bar{\beta}^2) \sinh(\bar{\beta}\bar{h}) \\ (k^2 + \bar{\beta}^2) \cosh(\bar{\alpha}\bar{h}) & 2ik\bar{\beta} \cosh(\bar{\beta}\bar{h}) \end{pmatrix} \begin{pmatrix} A \\ B \end{pmatrix} = 0 \quad (2.24)$$

which has non-trivial solutions if the determinant of the matrix is zero. As condition for a vanishing determinant of the matrix in (2.24) we find

$$\frac{\tanh(\bar{\beta}\bar{h})}{\tanh(\bar{\alpha}\bar{h})} = \frac{4k^2\bar{\alpha}\bar{\beta}}{(k^2 + \bar{\beta}^2)^2} \quad (2.25)$$

¹It should be noted that the combination of $e^{i\omega t}$ and e^{ikx} actually constitutes left going modes while right going modes would be described either by $e^{-i\omega t}$ and e^{ikx} or $e^{i\omega t}$ and e^{-ikx} .

which is of course the dispersion relation given in [30] for symmetric Lamb-modes. If we remember the definitions of $\bar{\alpha}$ and $\bar{\beta}$ that were given in (2.13) and (2.16), it is clear to see that (2.25) can indeed be seen as a function $k(\omega)$. Except for a normalization factor, the expressions (2.19)-(2.20) and (2.21)-(2.23) are fully determined for each pair of frequency ω and wave number k that satisfies the dispersion relation (2.25).

For an antisymmetric displacement field u_x we find $A_1 = -B_1 = A$ and $A_2 = B_2 = B$. The remaining steps are identical to those for S -modes. The expressions for displacement and stress components of A -modes are

$$u_x = (ikA \sinh(\bar{\alpha}y) + \bar{\beta}B \sinh(\bar{\beta}y)) e^{i(kx+\omega t)} \quad (2.26)$$

$$u_y = (\bar{\alpha}A \cosh(\bar{\alpha}y) - ikB \cosh(\bar{\beta}y)) e^{i(kx+\omega t)}. \quad (2.27)$$

$$\sigma_{xx} = \mu (-(k^2 + 2\bar{\alpha}^2 - \bar{\beta}^2)A \sinh(\bar{\alpha}y) + 2ik\bar{\beta}B \sinh(\bar{\beta}y)) e^{i(kx+\omega t)} \quad (2.28)$$

$$\sigma_{xy} = \mu (2ik\bar{\alpha}A \cosh(\bar{\alpha}y) + (k^2 + \bar{\beta}^2)B \cosh(\bar{\beta}y)) e^{i(kx+\omega t)} \quad (2.29)$$

and

$$\sigma_{yy} = \mu ((k^2 + \bar{\beta}^2)A \sinh(\bar{\alpha}y) - 2ik\bar{\beta}B \sinh(\bar{\beta}y)) e^{i(kx+\omega t)} \quad (2.30)$$

with the dispersion relation

$$\frac{\tanh(\bar{\beta}\bar{h})}{\tanh(\bar{\alpha}\bar{h})} = \frac{(k^2 + \bar{\beta}^2)^2}{4k^2\bar{\alpha}\bar{\beta}}. \quad (2.31)$$

2.1.2 Displacement and stress in cylindrical rods

The mathematical description of guided wave modes essentially follows the outline of those for Lamb-waves. A detailed derivation can be found e.g. in [31] and shall not be repeated in full length here. Since the aim of this work is only to apply the multimodal approach to axially symmetric modes in cylindrical structures, we will restrict the discussion of displacement and stress in cylindrical rods to those thus limiting the description to the rz -plane.

For cylindrical geometry, the displacement vector is $\vec{u} = (u_r, u_\varphi, u_z)^T$. The elastic tensor for isotropic materials (2.2) and the definitions of stress (2.3) and strain tensor (2.5) as well as the Helmholtz decomposition of \vec{u} (2.8) and the wave equations (2.7), (2.9) and (2.10) remain valid but the nabla operator $\vec{\nabla}$ and gradient of a vector field have to be expressed in cylindrical coordinates. Stress and strain tensor now take the form (compare e.g. [32, 33]²)

$$\boldsymbol{\sigma} = \begin{pmatrix} \sigma_{rr} & \sigma_{r\varphi} & \sigma_{rz} \\ \sigma_{r\varphi} & \sigma_{\varphi\varphi} & \sigma_{\varphi z} \\ \sigma_{rz} & \sigma_{\varphi z} & \sigma_{zz} \end{pmatrix} \quad (2.32)$$

²Note that in [32] $\epsilon_{\varphi\varphi}$ is in fact given as $(\partial_r u_\varphi + u_r)/r$ instead of $(\partial_\varphi u_\varphi + u_r)/r$. The derivation of $\text{grad}(\vec{u})$ in cylindrical coordinates performed during the course of this research project leads to the latter expression which is used in this thesis. Expressions for other elements of the strain tensor given in [32] and [33] are in accordance with the results presented here.

and

$$\epsilon = \begin{pmatrix} \partial_r u_r & \frac{\partial_\varphi u_r}{2r} + \frac{r}{2} \partial_r \left(\frac{u_\varphi}{r} \right) & \frac{\partial_z u_r + \partial_r u_z}{2} \\ \frac{\partial_\varphi u_r}{2r} + \frac{r}{2} \partial_r \left(\frac{u_\varphi}{r} \right) & \frac{\partial_\varphi u_\varphi + u_r}{r} & \frac{\partial_z u_\varphi}{2} + \frac{\partial_\varphi u_z}{2r} \\ \frac{\partial_z u_r + \partial_r u_z}{2} & \frac{\partial_z u_\varphi}{2} + \frac{\partial_\varphi u_z}{2r} & \partial_z u_z \end{pmatrix}. \quad (2.33)$$

In circumferential direction the solutions of (2.9) and (2.10) will in general resemble standing waves $\cos(n\varphi)$ and $\sin(n\varphi)$ where n denotes the circumferential order of the respective mode. Assuming axially symmetric solutions ($n=0$) and free propagation in time and in z -direction, the wave equation for the Helmholtz potentials (2.9) and (2.10) take the form

$$\frac{1}{r} \partial_r (r \partial_r \Phi) = \alpha^2 \Phi \quad (2.34)$$

$$\frac{1}{r} \partial_r (r \partial_r H_r) - \frac{H_r}{r^2} = \beta^2 H_r \quad (2.35)$$

$$\frac{1}{r} \partial_r (r \partial_r H_\varphi) - \frac{H_\varphi}{r^2} = \beta^2 H_\varphi \quad (2.36)$$

$$\frac{1}{r} \partial_r (r \partial_r H_z) = \beta^2 H_z \quad (2.37)$$

with

$$\alpha^2 = -\bar{\alpha}^2 = k_L^2 - k^2 = \frac{\omega^2 \rho}{\lambda + 2\mu} - k^2 \quad (2.38)$$

$$\beta^2 = -\bar{\beta}^2 = k_T^2 - k^2 = \frac{\omega^2 \rho}{\mu} - k^2. \quad (2.39)$$

As we can see, (2.34) and (2.37) can be rewritten as Bessel differential equations of 0th order while (2.36) and (2.37) correspond to Bessel differential equations of 1st order. In general, the solution to a Bessel differential equation of n th order contains Bessel functions of first and second kind of n th order, however, in order to avoid singularities at $r = 0$, the contributions of Bessel functions of second kind have to be discarded³ which leaves

$$\Phi = A_1 J_0(\alpha r) e^{i(kz + \omega t)} \quad (2.40)$$

$$H_r = A_2 J_1(\beta r) e^{i(kz + \omega t)} \quad (2.41)$$

$$H_\varphi = A_3 J_1(\beta r) e^{i(kz + \omega t)} \quad (2.42)$$

$$H_z = A_4 J_0(\beta r) e^{i(kz + \omega t)} \quad (2.43)$$

as solutions to (2.34)-(2.37). Using (2.8), we find that for the case of axially symmetric waves in a cylindrical geometry the displacement fields are

$$u_r = \partial_r \Phi - \partial_z H_\varphi \quad (2.44)$$

$$u_\varphi = \partial_z H_r - \partial_r H_z \quad (2.45)$$

³or eliminated in a mathematically clean way by choosing appropriate boundary conditions at $r = 0$

$$u_z = \partial_z \Phi + \partial_r H_\varphi + \frac{H_\varphi}{r}. \quad (2.46)$$

As we can see, the displacement vector can be split into two independent components. The first one contains only the displacement in circumferential direction and represents the torsional guided waves (T -modes). The second one contains displacement fields in r - and z -direction and represents the axially symmetric longitudinal waves (L -modes) which correspond to the plane strain assumption we used in the derivation of Lamb-modes. For modes of higher order in circumferential direction, longitudinal and torsional movement would no longer be decoupled. The resulting modes are usually referred to as flexural modes (F -modes). Since the adaptation of the multimodal method will be restricted to L -modes, only (2.40) and (2.42) have to be taken into consideration from this point onward. If we set $A_1 = A$ and $A_3 = B$, the relevant elements of the displacement vector \vec{u} and stress tensor $\boldsymbol{\sigma}$ are

$$u_r = -(\alpha A J_1(\alpha r) + ik B J_1(\beta r)) e^{i(kz + \omega t)} \quad (2.47)$$

$$u_z = (ik A J_0(\alpha r) + \beta B J_0(\beta r)) e^{i(kz + \omega t)} \quad (2.48)$$

$$\sigma_{rr} = \mu \left(A \left[(k^2 - \beta^2) J_0(\alpha r) + \frac{2\alpha}{r} J_1(\alpha r) \right] - 2ik B \left[\beta J_0(\beta r) - \frac{1}{r} J_1(\beta r) \right] \right) e^{i(kz + \omega t)} \quad (2.49)$$

$$\sigma_{rz} = \mu (-2ik\alpha A J_1(\alpha r) + (k^2 - \beta^2) B J_1(\beta r)) e^{i(kz + \omega t)} \quad (2.50)$$

$$\sigma_{zz} = \mu (-(k^2 - 2\alpha^2 + \beta^2) A J_0(\alpha r) + 2ik\beta B J_0(\beta r)) e^{i(kz + \omega t)} \quad (2.51)$$

$$\sigma_{\varphi\varphi} = \mu \left(A \left[(k^2 + 2\alpha^2 - \beta^2) J_0(\alpha r) - \frac{2\alpha}{r} J_1(\alpha r) \right] - \frac{2ik}{r} B J_1(\beta r) \right) e^{i(kz + \omega t)}. \quad (2.52)$$

The dispersion relation which determines (2.47)-(2.51) up to a normalization factor is derived from the boundary condition of a traction free lateral surface (i.e. setting (2.49) and (2.50) to zero at the outer radius $r = R$) and reads (compare e.g. [31])

$$(k^2 - \beta^2)^2 J_0(\alpha R) J_1(\beta R) + 4k^2 \alpha \beta J_1(\alpha R) J_0(\beta R) - \frac{2\alpha}{R} (k^2 + \beta^2) J_1(\alpha R) J_1(\beta R) = 0. \quad (2.53)$$

2.1.3 Displacement and stress in hollow cylinders

A detailed mathematical derivation of guided waves in thick walled hollow cylinders has been covered e.g. in [32, 33, 36]. As in the previous section we will restrict the discussion to the solutions of the wave equation that are relevant for this thesis (i.e. displacement and stress fields of L -modes).

The expressions for $\boldsymbol{\sigma}$ and $\boldsymbol{\epsilon}$ given in (2.32) and (2.33) remain valid for hollow cylinders as do the radial equations for the Helmholtz potentials (2.34)-(2.37) if we assume axial symmetry and free propagation in time and in z -direction. Furthermore, the Helmholtz decomposition (2.8) still leads to (2.44)-(2.46) meaning that the decoupling of axially

symmetric solutions into L - and T -modes is still in effect⁴. Since the scope of this work is restricted to L -modes, only (2.34) and (2.36) have to be evaluated which yields

$$\Phi = (AJ_0(\alpha r) + CY_0(\alpha r)) e^{i(kz+\omega t)} \quad (2.54)$$

and

$$H_\varphi = (BJ_1(\beta r) + DY_1(\beta r)) e^{i(kz+\omega t)} \quad (2.55)$$

with J_n and Y_n being Bessel functions of first and second kind. This leads to the displacement fields

$$u_r = -(\alpha(AJ_1(\alpha r) + CY_1(\alpha r)) + ik(BJ_1(\beta r) + DY_1(\beta r))) e^{i(kz+\omega t)} \quad (2.56)$$

$$u_z = (ik(AJ_0(\alpha r) + CY_0(\alpha r)) + \beta(BJ_0(\beta r) + DY_0(\beta r))) e^{i(kz+\omega t)} \quad (2.57)$$

and subsequently to the stress components

$$\begin{aligned} \sigma_{rr} = \mu \left[(k^2 - \beta^2)(AJ_0(\alpha r) + CY_0(\alpha r)) + \frac{2\alpha}{r}(AJ_1(\alpha r) + CY_1(\alpha r)) \right. \\ \left. - 2ik\beta(BJ_0(\beta r) + DY_0(\beta r)) + \frac{2ik}{r}(BJ_1(\beta r) + DY_1(\beta r)) \right] e^{i(kz+\omega t)} \end{aligned} \quad (2.58)$$

$$\sigma_{rz} = \mu \left[-2ik\alpha(AJ_1(\alpha r) + CY_1(\alpha r)) + (k^2 - \beta^2)(BJ_1(\beta r) + DY_1(\beta r)) \right] e^{i(kz+\omega t)} \quad (2.59)$$

$$\sigma_{zz} = \mu \left[-(k^2 - 2\alpha^2 + \beta^2)(AJ_0(\alpha r) + CY_0(\alpha r)) + 2ik\beta(BJ_0(\beta r) + DY_0(\beta r)) \right] e^{i(kz+\omega t)} \quad (2.60)$$

$$\begin{aligned} \sigma_{\varphi\varphi} = \mu \left[(k^2 + 2\alpha^2 - \beta^2)(AJ_0(\alpha r) + CY_0(\alpha r)) - \frac{2\alpha}{r}(AJ_1(\alpha r) + CY_1(\alpha r)) \right. \\ \left. - \frac{2ik}{r}(BJ_1(\beta r) + DY_1(\beta r)) \right] e^{i(kz+\omega t)} \end{aligned} \quad (2.61)$$

In order to determine the expressions (2.56)-(2.60) up to a normalization factor, we use the boundary condition of traction free surfaces (i.e. equating (2.58) and (2.59) to zero at the inner and outer radius $r = R_I$ and $r = R_O$). The dispersion relation follows from

$$\det \begin{pmatrix} D_{11} & D_{12} & D_{13} & D_{14} \\ D_{21} & D_{22} & D_{23} & D_{24} \\ D_{31} & D_{32} & D_{33} & D_{34} \\ D_{41} & D_{42} & D_{43} & D_{44} \end{pmatrix} = 0 \quad (2.62)$$

⁴Which is not surprising given that a cylindrical rod can be viewed as the special case of a hollow cylinder with inner radius $R_I = 0$.

where the matrix elements are

$$D_{11} = (k^2 - \beta^2)J_0(\alpha R_O) + \frac{2\alpha}{R_O}J_1(\alpha R_O) \quad (2.63)$$

$$D_{12} = -2ik \left(\beta J_0(\beta R_O) - \frac{J_1(\beta R_O)}{R_O} \right) \quad (2.64)$$

$$D_{13} = (k^2 - \beta^2)Y_0(\alpha R_O) + \frac{2\alpha}{R_O}Y_1(\alpha R_O) \quad (2.65)$$

$$D_{14} = -2ik \left(\beta Y_0(\beta R_O) - \frac{Y_1(\beta R_O)}{R_O} \right) \quad (2.66)$$

$$D_{21} = (k^2 - \beta^2)J_0(\alpha R_I) + \frac{2\alpha}{R_I}J_1(\alpha R_I) \quad (2.67)$$

$$D_{22} = -2ik \left(\beta J_0(\beta R_I) - \frac{J_1(\beta R_I)}{R_I} \right) \quad (2.68)$$

$$D_{23} = (k^2 - \beta^2)Y_0(\alpha R_I) + \frac{2\alpha}{R_I}Y_1(\alpha R_I) \quad (2.69)$$

$$D_{24} = -2ik \left(\beta Y_0(\beta R_I) - \frac{Y_1(\beta R_I)}{R_I} \right) \quad (2.70)$$

$$D_{31} = -2ik\alpha J_0(\alpha R_O) \quad (2.71)$$

$$D_{32} = (k^2 - \beta^2)J_1(\beta R_O) \quad (2.72)$$

$$D_{33} = -2ik\alpha Y_0(\alpha R_O) \quad (2.73)$$

$$D_{34} = (k^2 - \beta^2)Y_1(\beta R_O) \quad (2.74)$$

$$D_{41} = -2ik\alpha J_0(\alpha R_I) \quad (2.75)$$

$$D_{42} = (k^2 - \beta^2)J_1(\beta R_I) \quad (2.76)$$

$$D_{43} = -2ik\alpha Y_0(\alpha R_I) \quad (2.77)$$

$$D_{44} = (k^2 - \beta^2)Y_1(\beta R_I) \quad (2.78)$$

A closed expression of this dispersion relation would be long and complicated, however, since such an expression can be useful for an efficient implementation⁵, it will be provided in Appendix A.

2.2 The effect of a varying cross-section

Since the dispersive behaviour of guided waves depends on the frequency as well as the thickness of the waveguide, changes of the cross-section will result in corresponding changes of wave numbers for excited modes and might lead to changes in the number of

⁵Calculating the determinant of a matrix that depends on a vector of different frequencies in MATLAB requires to switch through the individual frequencies in a for-loop which is expensive in terms of computation time. While using the pre-implemented det-function is more efficient for single frequencies, a vectorized implementation of a closed expression for the dispersion relation is superior if a large number of different frequencies has to be considered.

potentially propagating wave modes. At a point where the cross-section of the waveguide changes, mode coupling will occur that allows energy transfer between different guided wave modes thus resulting in possible attenuation of individual propagating modes as well as the appearance of modes within the mode spectrum that had not been excited initially [11]. In addition there will be coupling effects between forward and backward propagating versions of guided wave modes which results in some of the incident energy being reflected [11, 12]. If for a particular cross-section the combination of frequency and thickness coincides with a cut-off in the dispersion curves (i.e. a point at which the wave number of a mode switches from complex to real values), an incident wave that loses its ability to propagate behind that cross-section (due to the fact that it would become evanescent) will be subject to total reflection. A mathematical description of this phenomena can be found in [12] while [39] confirms this behaviour in experimental results for the case of a plate with linearly varying thickness. The results presented in [39] also show that at cut-offs where the wave numbers of two different modes coincide (referred to as irregular cut-offs in [12]), strong mode conversion might occur as well.

2.3 Concept of the multimodal method

In order to solve the problem of waveguides with varying cross-section, modal methods have already been suggested several decades ago (see e.g. [40] or [41]). A detailed theoretical description of a modal decomposition approach and its application to several aeroacoustic problems have been provided during the 90s by Pagneux et al. in [42] and [43]. An extended and modified version of this method was adapted to the description of Lamb-waves in plates with varying thickness in 2006 as multimodal method [17]. While there is no pressing need to repeat a detailed derivation of the entire method here, a descriptive outline of the general idea will be provided.

The basic concept behind the multimodal method is illustrated in Figure 2.2 on the example of a plate where thickness increases in a single step.

We assume that only the first antisymmetric mode is propagating before the step. Behind the step we can expect most of the energy to keep propagating within the initial mode albeit with a different frequency. However, due to the asymmetric nature of the change in thickness, some energy might be coupled into the first symmetric mode. In addition, the number of modes that can propagate might increase so that higher order modes may be excited as well. To avoid discontinuities within the displacement field at the position of the step, local contributions of evanescent (i.e. non-propagating) modes have to be taken into account⁶. If we extend the situation illustrated in Figure 2.2 to a plate with continuously varying thickness, it is straightforward to conclude that the mode spectrum also has to change continuously in terms of which modes are excited as well as regarding their respective relative weight within the spectrum.

⁶The relevance of evanescent modes in mode expansions for contributions to the near field was also noted in the investigation of wave transfer through cylindrical bars of constant thickness in [44].

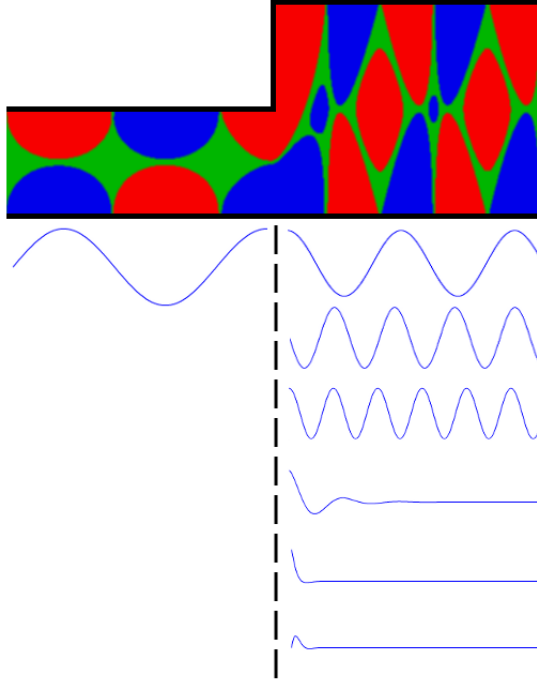


Figure 2.2: Multimodal approach at a transition between different cross-sections.

In a nutshell, the idea of the multimodal approach as described in [17] is to express the local displacement field within the waveguide in a basis of guided wave modes of the corresponding waveguide with constant thickness at any given point along the direction of wave propagation. While similar mode expansions have been successfully applied in the investigation of wave propagation through waveguides of constant cross-section (e.g. [44, 45]), the application to waveguides with varying cross-section is more complicated due to the fact that options for mode coupling and reflection have to be included into the model. With the continuous variation of cross-section being translated into a continuous variation of the coefficients describing relative weights within the expansion into the modal basis, the numerical effort of calculating the displacement field along the waveguide is now reduced to solving the differential equations which govern the evolution of these coefficients in wave propagation direction. A more detailed mathematical description of this method will be provided on the example of plates with varying thickness in Chapter 3.

2.4 Determination of complex wave numbers

As mentioned before, contributions of evanescent waves have to be considered in the multimodal approach in order to obtain accurate results. This means that at a given frequency real and complex wave numbers will have to be extracted from the dispersion

relations (2.25), (2.31), (2.53) and (2.62). The following three paragraphs contain a brief overview and discussion of various existing methods for the computation of wave numbers which can be found in similar form in [46].

Calculations of dispersion curves by use of root finding algorithms have been carried out e.g. by Zemanek for cylindrical rods [31] and by Gazis for hollow cylinders [34]. The approach of using a root finding algorithm on a closed analytical expression of the dispersion relation is still in use today, for example in the commercially available software Disperse [47] or the free MATLAB script PCDisp [48], both of which use the global matrix method as described e.g. in [49] to extend their applicability to layered structures. However, this method can be very expensive in terms of computation time, especially for the calculation of complex wave numbers.

Over the last two decades prior to this thesis, several numerical methods for the calculation of wave numbers have been suggested as alternatives to a direct root search. The older ones of these methods are based on the finite element method (FEM) (see e.g. [50]) and rely on discretizing only a representative part of the waveguide [51, 52]. A more advanced approach is the so called semi-analytical finite element method (SAFE) which is based on the idea of discretizing the cross-section with finite elements while describing the solution in the direction of wave propagation analytically. This method has been implemented for various problems e.g. the investigation of wave propagation in rods and rails [53], pre-stressed pipes [54], damped cylinders [55], damped waveguides of arbitrary cross-section [56] or leaky waves in embedded waveguides of arbitrary cross-section [57]. The scaled boundary finite element method (SBFEM) shows some similarities with the SAFE approach in the case of three dimensional waveguides with arbitrary cross-section but utilizes different solution procedures in order to enhance efficiency. In contrast to FEM and SAFE, the SBFEM makes use of higher order spectral elements to discretize the cross-section [58] and yields a significant advantage in terms of computational efficiency for plate structures [59] and axisymmetric waveguides [60, 61]. Other methods that have been suggested for the calculation of wave numbers in a plate at a given frequency but, to the best of the author's knowledge, haven't seen wide use in applications so far include a spectral decomposition into a basis of orthogonal functions that transforms the wave equations for components of the displacement vector into a regular eigenvalue problem [62], a spectral method that represents differential operators in the equation of motion by Chebyshev differentiation matrices to transform the equations of motion into a generalized eigenvalue problem [63] or a finite product approximation [64].

This work adopts the spectral decomposition method that has been suggested in [62] for numerical calculations of dispersion curves of symmetric and antisymmetric Lamb-modes in isotropic homogeneous plates. The general idea of this method is to express the components of the displacement vector \vec{u} in an orthogonal basis formed by eigenfunctions of the Laplace operator on the waveguide's cross-section. If the equations of motion for the different displacement components are projected onto that basis, the problem of finding the wave numbers of guided wave modes (i.e. the roots of the dispersion relation) at a

given frequency can be transformed into an eigenvalue problem that can be solved efficiently. Although the spectral decomposition method is less accurate and more limited in its applicability than advanced semi-analytical approaches like SAFE or SBFEM, it can be used to obtain complex dispersion curves relatively fast and is easy to implement. Furthermore, the fact that wave numbers are calculated and sorted at a single given frequency eliminates the necessity to start at a sufficiently low frequency and use mode tracking while advancing to the frequency range of interest. In contrast to a direct root search there is no risk of missing a mode and no errors can occur at frequencies where the wave numbers of two different modes are very similar. For these features, the spectral decomposition method was considered to be an attractive alternative to established methods for the problems that had to be covered in this thesis.

The method has been successfully extended to the use on L -modes in isotropic homogeneous cylindrical rods and hollow cylinders in a previous publication [46]. While the most important steps of these adaptations will be repeated in Chapter 4, this section will cover the basic procedure illustrated on the example of plates (compare to [62] for a more detailed description).

Starting point for the spectral decomposition method is the wave equation for the displacement vector \vec{u} as given in (2.7). Under the assumption of plane strain and free propagation in x -direction (2.7) leads to

$$(k^2 - k_L^2)u_x - ik\frac{\gamma - 1}{\gamma}\partial_y u_y - \frac{\partial_y^2 u_x}{\gamma} = 0 \quad (2.79)$$

and

$$(k^2 - k_T^2)u_y - ik(\gamma - 1)\partial_y u_x - \gamma\partial_y u_y = 0 \quad (2.80)$$

as equations of motion for the displacement fields in x - and y -direction where k_L and k_T are the longitudinal and transversal wave number respectively and $\gamma = (\lambda + 2\mu)/\mu$ is a function of the Lamé constants. The boundary conditions of traction free surfaces at $y = h/2 = \bar{h}$ and $y = -h/2 = -\bar{h}$ take the form

$$\partial_y u_x(\pm\bar{h}) = -ik u_y(\pm\bar{h}) \quad (2.81)$$

and

$$\partial_y u_y(\pm\bar{h}) = -ik\frac{\gamma - 2}{\gamma}u_x(\pm\bar{h}). \quad (2.82)$$

Solving the Helmholtz equation on the cross-section (i.e. in y -direction) under boundary conditions that force symmetric or antisymmetric solutions yields two different sets of functions both of which form a complete orthogonal basis to describe even or odd functions respectively. The normalized functions are

$$\psi_1 = \sqrt{\frac{1}{h}} \cos(\phi_n y) \text{ and } \psi_{n>1} = \sqrt{\frac{2}{h}} \cos(\phi_n y) \quad (2.83)$$

$$\chi_n = \sqrt{\frac{2}{\bar{h}}} \sin(\theta_n y) \quad (2.84)$$

with $\phi_n = (n-1)\pi/\bar{h}$ and $\theta_n = (n-1/2)\pi/\bar{h}$. The normalization was chosen to fulfill $\langle \psi_n | \psi_m \rangle = \delta_{nm}$ and $\langle \chi_n | \chi_m \rangle = \delta_{nm}$ where the scalar product, presented in bra-ket notation, is defined as $\langle f(y) | g(y) \rangle = \int_0^{\bar{h}} f(y)g(y)dy$ and δ_{nm} denotes Kronecker's delta. Since A - and S -modes are independent solutions of the wave equation for a plate under plane strain approximation, they have to be treated as two distinct cases for the spectral decomposition.

2.4.1 Spectral decomposition for symmetric Lamb-waves

After reviewing (2.19) and (2.20), the displacement fields for S -modes are expressed in the bases (2.83) and (2.84) as

$$u_x = \sum_n V_n^S \psi_n(y) \quad (2.85)$$

and

$$u_y = \sum_n U_n^S \chi_n(y). \quad (2.86)$$

Now we project (2.79) onto ψ_n and (2.80) onto χ_n . If the boundary conditions expressed in (2.81) and (2.82) are taken into account, these projections yield the system of equations

$$k^2 \vec{V}^S + k \mathbf{A}^S \vec{U}^S + \mathbf{B}^S \vec{V}^S = 0 \quad (2.87)$$

and

$$k^2 \vec{U}^S + k \mathbf{C}^S \vec{V}^S + \mathbf{D}^S \vec{U}^S = 0 \quad (2.88)$$

where \vec{V}^S and \vec{U}^S are the vectors of coefficients in the expansion (2.85) and (2.86) respectively and \mathbf{A}^S , \mathbf{B}^S , \mathbf{C}^S and \mathbf{D}^S are matrices which can be expressed by

$$A_{nm}^S = \frac{2i(-1)^{n+m}}{\gamma \bar{h}} \left(\frac{\phi_n^2 + (\gamma-2)\theta_m^2}{\theta_m^2 - \phi_n^2} \right) \quad (2.89)$$

$$B_{nm}^S = \left(\frac{\phi_n^2}{\gamma} - k_L^2 \right) \delta_{nm} \quad (2.90)$$

$$C_{nm}^S = -\gamma A_{mn}^S \quad (2.91)$$

$$D_{nm}^S = (\gamma \theta_n^2 - k_T^2) \delta_{nm}. \quad (2.92)$$

2.4.2 Spectral decomposition for antisymmetric Lamb-waves

For A -modes, the displacement fields u_x and u_y are expressed as

$$u_x = \sum_n V_n^A \chi_n(y) \quad (2.93)$$

and

$$u_y = \sum_n U_n^A \psi_n(y) \quad (2.94)$$

and we project (2.79) onto χ_n and (2.80) onto ψ_n . Once more we obtain systems of equations for the coefficients U_n^A and V_n^A which read

$$k^2 \vec{V}^A + k \mathbf{A}^A \vec{U}^A + \mathbf{B}^A \vec{V}^A = 0 \quad (2.95)$$

and

$$k^2 \vec{U}^A + k \mathbf{C}^A \vec{V}^A + \mathbf{D}^A \vec{U}^A = 0. \quad (2.96)$$

The matrices \mathbf{A}^A , \mathbf{B}^A , \mathbf{C}^A and \mathbf{D}^A can be expressed by

$$A_{nm}^A = \frac{2i(-1)^{n+m}}{\gamma \bar{h}} \left(\frac{(\gamma - 2)\phi_m^2 + \theta_n^2}{\phi_m^2 - \theta_n^2} \right) \quad (2.97)$$

$$B_{nm}^A = \left(\frac{\theta_n^2}{\gamma} - k_L^2 \right) \delta_{nm} \quad (2.98)$$

$$C_{nm}^A = -\gamma A_{mn}^A \quad (2.99)$$

$$D_{nm}^A = (\gamma \phi_n^2 - k_T^2) \delta_{nm}. \quad (2.100)$$

2.4.3 Computing the dispersion curves

If we omit the superscripts that distinguish between A - and S -modes, the systems of equations for the coefficients of the spectral decomposition are

$$k^2 \vec{V} + k \mathbf{A} \vec{U} + \mathbf{B} \vec{V} = 0 \quad (2.101)$$

and

$$k^2 \vec{U} + k \mathbf{C} \vec{V} + \mathbf{D} \vec{U} = 0. \quad (2.102)$$

If (2.101) is rearranged to isolate \vec{V} and subsequently inserted into (2.102), we obtain

$$K^2 \mathcal{X} + K(\mathbf{B} - \mathbf{A}\mathbf{C} + \mathbf{C}^{-1}\mathbf{D}\mathbf{C})\mathcal{X} + \mathbf{B}\mathbf{C}^{-1}\mathbf{D}\mathbf{C}\mathcal{X} = 0 \quad (2.103)$$

with $K = k^2$ and $\mathcal{X} = \mathbf{C}^{-1}\vec{U}\mathbf{C}$. If we define

$$K \mathcal{X} = \mathcal{Y} \quad (2.104)$$

we can rewrite (2.103) into an expression that is linear in K

$$K \mathcal{Y} + \mathbf{O} \mathcal{Y} + \mathbf{P} \mathcal{X} = 0 \quad (2.105)$$

with $\mathbf{O} = \mathbf{B} - \mathbf{AC} + \mathbf{C}^{-1}\mathbf{DC}$ and $\mathbf{P} = \mathbf{BC}^{-1}\mathbf{DC}$. Finally we combine (2.104) and (2.105) into

$$\begin{pmatrix} 0 & \mathbb{1} \\ -\mathbf{P} & -\mathbf{O} \end{pmatrix} \begin{pmatrix} \vec{\mathcal{X}} \\ \vec{\mathcal{Y}} \end{pmatrix} = K \begin{pmatrix} \vec{\mathcal{X}} \\ \vec{\mathcal{Y}} \end{pmatrix}. \quad (2.106)$$

The real and complex wave numbers at a given frequency can now be calculated by taking the square roots of the eigenvalues of the $2N \times 2N$ matrix given in (2.106). Real positive square roots and complex square roots with positive imaginary part are the ones that carry physical meaning. Wave numbers of A - and S -modes are calculated separately and can directly be assigned to their corresponding modes if real results are sorted in descending order and placed before complex results ordered by ascending absolute value with positive real parts placed before negative real parts in case of identical absolute values. If the spectral decomposition is truncated after N elements, we obtain $2N$ eigenvalues. While Pagneux and Maurel stated that “...the k spectrum found with the spectral method coincides with the exact one (k^e) for the N or so first values...” [62], the results observed in the course of this work suggest the use of the first $N - 1$ eigenvalues (see [46]). Repeating the calculation of wave numbers for a sufficiently large number of different frequencies will map out the complex dispersion curves which are shown in Figure 2.3.

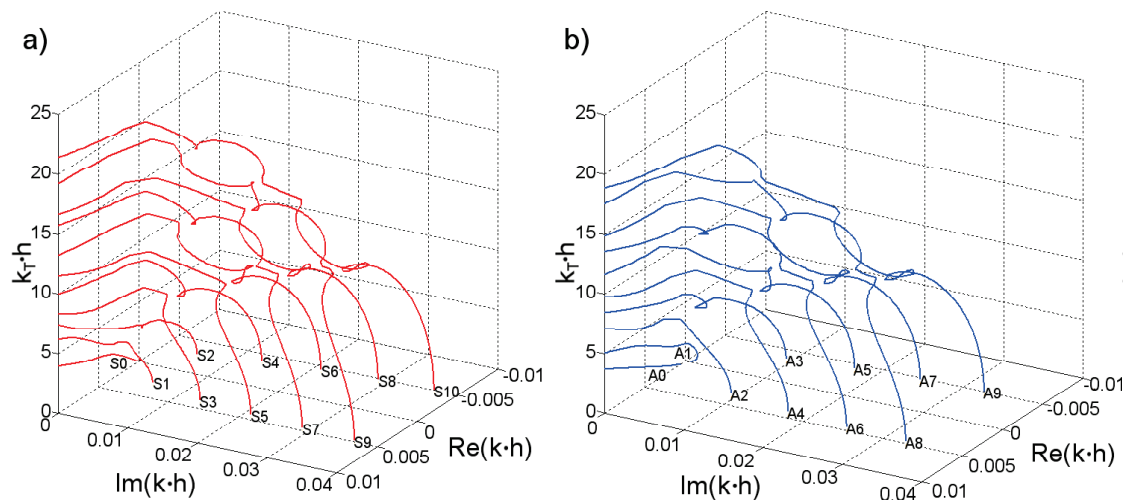


Figure 2.3: Complex dispersion curves of a) symmetric and b) antisymmetric Lamb-modes in an isotropic homogeneous plate.

In Figure 2.4, only the real wave numbers are plotted over the frequency thickness product fh for an isotropic homogeneous plate.

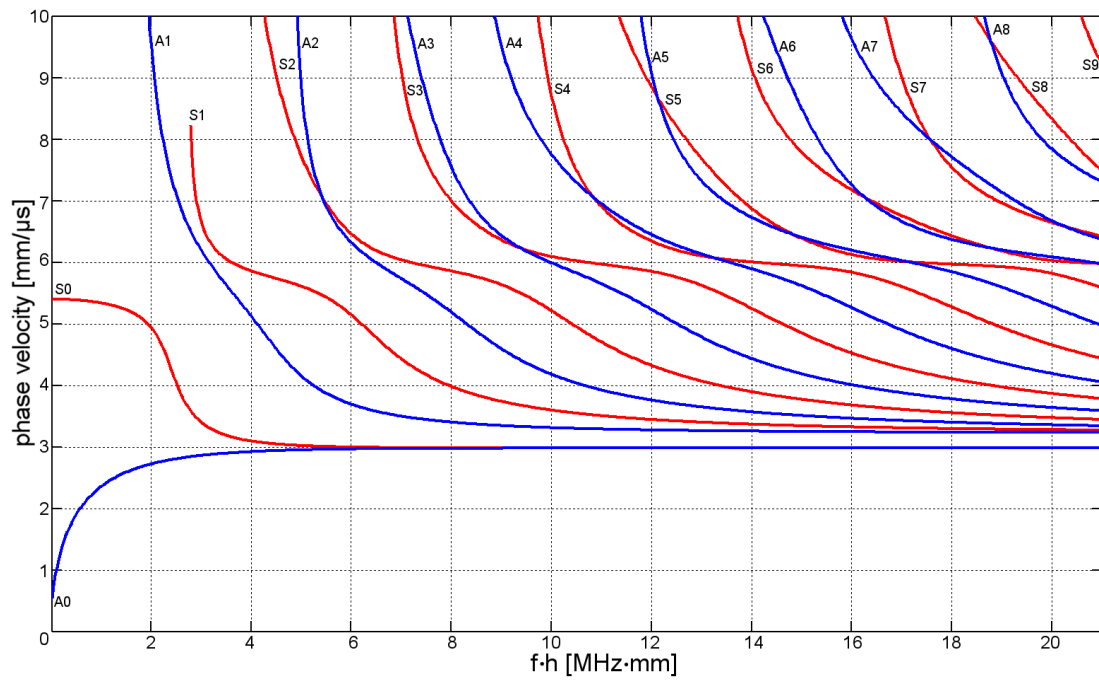


Figure 2.4: Real dispersion curves of symmetric and antisymmetric Lamb-modes in an isotropic homogeneous plate as plot of phase velocities over frequency thickness product.

Chapter 3

Implementation for plates

3.1 Plates with symmetrically and asymmetrically varying thickness

In this section we will largely follow the description of the multimodal method as given in [17] for Lamb-waves in plates with symmetrically varying thickness while making the necessary generalizations to cover plates with asymmetrically varying thickness as well. While not strictly required for the subsequent adaptation to cylindrical geometries, this extension to plates with asymmetrically varying thickness provides valuable insight into the handling of different families of guided wave modes. The starting point for the multimodal method is the general equation of motion for linear elastodynamics in frequency domain written in the form

$$-\rho\omega^2\vec{u} = \text{div}(\boldsymbol{\sigma}). \quad (3.1)$$

For Cartesian coordinates the divergence of the stress tensor $\boldsymbol{\sigma}$ takes the form

$$\text{div}(\boldsymbol{\sigma}) = \begin{pmatrix} \partial_x\sigma_{xx} + \partial_y\sigma_{xy} + \partial_z\sigma_{xz} \\ \partial_x\sigma_{xy} + \partial_y\sigma_{yy} + \partial_z\sigma_{yz} \\ \partial_x\sigma_{xz} + \partial_y\sigma_{yz} + \partial_z\sigma_{zz} \end{pmatrix}. \quad (3.2)$$

Under plane strain approximation, (3.1) is reduced to a two dimensional problem. Using (2.1), (2.2) and (2.6), the remaining components of the stress tensor are expressed in terms of the relevant displacement fields u_x and u_y and the Lamé constants by

$$\sigma_{xx} = \lambda\partial_y u_y + (\lambda + 2\mu)\partial_x u_x \quad (3.3)$$

$$\sigma_{xy} = \mu(\partial_y u_x + \partial_x u_y) \quad (3.4)$$

$$\sigma_{yy} = (\lambda + 2\mu)\partial_y u_y + \lambda\partial_x u_x \quad (3.5)$$

which can be rewritten as

$$\partial_x u_x = \frac{f_1}{\lambda} - f_1\partial_y u_y, \quad (3.6)$$

$$\partial_x u_y = \frac{1}{\mu} \sigma_{xy} - \partial_y u_x \quad (3.7)$$

and

$$\sigma_{yy} = f_1 \sigma_{xx} + f_2 \partial_y u_y \quad (3.8)$$

with $f_1 = \lambda/(\lambda + 2\mu)$ and $f_2 = 4\mu(\lambda + \mu)/(\lambda + 2\mu)$. Furthermore, (3.1) and (3.2) lead to

$$\partial_x \sigma_{xx} = -\rho\omega^2 u_x - \partial_y \sigma_{xy} \quad (3.9)$$

and

$$\partial_x \sigma_{xy} = -\rho\omega^2 u_y - f_1 \partial \sigma_{xx} - f_2 \partial_y^2 u_y. \quad (3.10)$$

Since σ_{yy} can be expressed in terms of σ_{xx} and u_y , only four independent stress and displacement fields remain. In accordance with [17] and [65] these stress and displacement fields are expressed in a 4-dimensional vector which can be split into the two 2-dimensional vectors $\vec{X} = (u_x, \sigma_{xy})^T$ and $\vec{Y} = (-\sigma_{xx}, u_y)^T$. Now (3.6),(3.7),(3.9) and (3.10) can be written in the form of a vector equation

$$\partial_x \begin{pmatrix} \vec{X} \\ \vec{Y} \end{pmatrix} = \begin{pmatrix} 0 & \mathbf{F} \\ \mathbf{G} & 0 \end{pmatrix} \begin{pmatrix} \vec{X} \\ \vec{Y} \end{pmatrix} \quad (3.11)$$

where the matrix operators \mathbf{F} and \mathbf{G} are given as

$$\mathbf{F} = \begin{pmatrix} -\frac{f_1}{\lambda} & -f_1 \partial_y \\ f_1 \partial_y & -\rho\omega^2 - f_2 \partial_y^2 \end{pmatrix} \quad (3.12)$$

and

$$\mathbf{G} = \begin{pmatrix} \rho\omega^2 & \partial_y \\ -\partial_y & \frac{1}{\mu} \end{pmatrix}. \quad (3.13)$$

The eigenvectors of the eigenvalue problem corresponding to (3.11)

$$ik_n \begin{pmatrix} \vec{X}_n \\ \vec{Y}_n \end{pmatrix} = \begin{pmatrix} 0 & \mathbf{F} \\ \mathbf{G} & 0 \end{pmatrix} \begin{pmatrix} \vec{X}_n \\ \vec{Y}_n \end{pmatrix} \quad (3.14)$$

represent Lamb-modes as described in Chapter 2 with k_n being the wave numbers corresponding to the A - or S -mode of order n . However, compared to (2.19)-(2.22) and (2.26)-(2.29), the expressions given for stress and displacement fields of symmetric and antisymmetric Lamb-modes given in [17] slightly differ in the distribution of factors $\bar{\alpha}$ and $\bar{\beta}$. While no explanation for this deviation is provided in [17] itself, the reason is that working with the description of Lamb-modes that follows directly from the calculations done in [30] would give rise to artifacts whenever $\bar{\alpha}$ or $\bar{\beta}$ approaches zero. To avoid this, the Helmholtz potentials Φ and H_z (compare (2.14) and (2.15)) are renormalized in a way to ensure that they do not vanish for $\bar{\alpha} = 0$ or $\bar{\beta} = 0$ which leads to

$$\Phi = A \cosh(\bar{\alpha}y) e^{ikx} \quad (3.15)$$

and

$$H_z = B \frac{\sinh(\bar{\beta}y)}{\bar{\beta}} e^{ikx} \quad (3.16)$$

for symmetric Lamb-modes and to

$$\Phi = A \frac{\sinh(\bar{\alpha}y)}{\bar{\alpha}} e^{ikx} \quad (3.17)$$

and

$$H_z = B \cosh(\bar{\beta}y) e^{ikx} \quad (3.18)$$

for antisymmetric Lamb-modes. The time dependence $e^{i\omega t}$ has been omitted and will be neglected for the remainder of this section.

In Chapter 2 the plate surfaces were set at $y = h/2$ and $y = -h/2$. If the thickness of the plate varies in x -direction (i.e. direction of wave propagation), the upper and lower surface have to be described as functions $h_U(x)$ and $h_L(x)$. If $h_U(x) \neq -h_L(x)$ a local shift in y -direction has to be applied in order to preserve symmetric and antisymmetric properties in the description of Lamb-waves. The shift is given as $y \rightarrow (y - \tilde{h})$ with $\tilde{h} = (h_U + h_L)/2$ which translates the upper and lower bonds of y into $h_U \rightarrow \bar{h}$ and $h_L \rightarrow -\bar{h}$ with $\bar{h} = (h_U - h_L)/2$.

The eigenvectors from (3.14) form a basis in which the local stress and displacement fields within the plate can be expressed with \vec{X}_n and \vec{Y}_m fulfilling the biorthogonality relation [17]

$$\langle \vec{X}_n | \vec{Y}_m \rangle = \mathcal{I}_n \delta_{nm} \quad (3.19)$$

where the scalar product corresponds to an integration in y -direction from h_L to h_U ¹ and $\mathcal{I}_n(x)$ is a function that will later be used in the normalization of the coupling matrices. In the final step the normalization has to be chosen to fully determine the basis $(\vec{X}_n, \vec{Y}_n)^T$. Pagneux and Maurel suggested to construct the normalization in a way that neither \vec{X}_n nor \vec{Y}_n vanishes for $k_n = 0$ (i.e. that \vec{X}_n and \vec{Y}_n remain a valid orthogonal basis if $k_n = 0$) [17]. As a result a renormalization factor $Z_{c,n}$ is introduced which corresponds to the diagonal elements of the characteristic impedance matrix \mathbf{Z}_c [17]. The eigenvalue problem (3.14) is modified to

$$ik_n \begin{pmatrix} \vec{X}_n \\ Z_{c,n} \vec{Y}_n \end{pmatrix} = \begin{pmatrix} 0 & \mathbf{F} \\ \mathbf{G} & 0 \end{pmatrix} \begin{pmatrix} \vec{X}_n \\ Z_{c,n} \vec{Y}_n \end{pmatrix}. \quad (3.20)$$

The Lamb-mode eigenvectors take the form

$$\vec{X}_n = (k_n^2 + \bar{\beta}_n^2) ik_n Z_{c,n} \begin{pmatrix} \cosh(\bar{\alpha}_n(y - \tilde{h})) \\ 2\bar{\alpha}_n \mu \sinh(\bar{\alpha}_n(y - \tilde{h})) \end{pmatrix} + \begin{pmatrix} \cosh(\bar{\beta}_n(y - \tilde{h})) \\ (k_n^2 + \bar{\beta}_n^2) \frac{\mu}{\bar{\beta}_n} \sinh(\bar{\beta}_n(y - \tilde{h})) \end{pmatrix} \quad (3.21)$$

¹similar to the description provided in Chapter 2

$$\vec{Y}_n = (k_n^2 + \bar{\beta}_n^2) \begin{pmatrix} (k_n^2 + 2\bar{\alpha}_n^2 - \bar{\beta}_n^2)\mu \cosh(\bar{\alpha}_n(y - \tilde{h})) \\ \bar{\alpha}_n \sinh(\bar{\alpha}_n(y - \tilde{h})) \end{pmatrix} - \frac{ik_n}{Z_{c,n}} \begin{pmatrix} 2\mu \cosh(\bar{\beta}_n(y - \tilde{h})) \\ \frac{1}{\bar{\beta}_n} \sinh(\bar{\beta}_n(y - \tilde{h})) \end{pmatrix} \quad (3.22)$$

with

$$Z_{c,n} = \frac{i \sinh(\bar{\beta}_n \bar{h})}{2k_n \bar{\alpha}_n \bar{\beta}_n \sinh(\bar{\alpha}_n \bar{h})} = \frac{2ik_n \cosh(\bar{\beta}_n \bar{h})}{(k_n^2 + \bar{\beta}_n^2)^2 \cosh(\bar{\alpha}_n \bar{h})} \quad (3.23)$$

for S -modes and

$$\vec{X}_n = (k_n^2 + \bar{\beta}_n^2) ik_n Z_{c,n} \begin{pmatrix} \frac{1}{\bar{\alpha}_n} \sinh(\bar{\alpha}_n(y - \tilde{h})) \\ 2\mu \cosh(\bar{\alpha}_n(y - \tilde{h})) \end{pmatrix} + \begin{pmatrix} \bar{\beta}_n \sinh(\bar{\beta}_n(y - \tilde{h})) \\ (k_n^2 + \bar{\beta}_n^2)\mu \cosh(\bar{\beta}_n(y - \tilde{h})) \end{pmatrix} \quad (3.24)$$

$$\vec{Y}_n = (k_n^2 + \bar{\beta}_n^2) \begin{pmatrix} (k_n^2 + 2\bar{\alpha}_n^2 - \bar{\beta}_n^2) \frac{\mu}{\bar{\alpha}_n} \sinh(\bar{\alpha}_n(y - \tilde{h})) \\ \cosh(\bar{\alpha}_n(y - \tilde{h})) \end{pmatrix} - \frac{ik_n}{Z_{c,n}} \begin{pmatrix} 2\mu \bar{\beta}_n \sinh(\bar{\beta}_n(y - \tilde{h})) \\ \cosh(\bar{\beta}_n(y - \tilde{h})) \end{pmatrix} \quad (3.25)$$

with

$$Z_{c,n} = \frac{i \cosh(\bar{\beta}_n \bar{h})}{2k_n \cosh(\bar{\alpha}_n \bar{h})} = \frac{2ik_n \bar{\alpha}_n \bar{\beta}_n \sinh(\bar{\beta}_n \bar{h})}{(k_n^2 + \bar{\beta}_n^2)^2 \sinh(\bar{\alpha}_n \bar{h})} \quad (3.26)$$

for A -modes. The expansion of general stress and displacement fields in Lamb-modes is

$$\vec{X} = \sum_{n \in \mathbb{N}} a_n(x) \vec{X}_n \quad (3.27)$$

$$\vec{Y} = \sum_{n \in \mathbb{N}} b_n(x) \vec{Y}_n \quad (3.28)$$

with

$$a_n = c_n^+ + c_n^- \quad (3.29)$$

and

$$b_n = Z_{c,n} (c_n^+ - c_n^-) \quad (3.30)$$

incorporating the coefficients c_n^+ for waves propagating in positive direction and c_n^- for waves propagating in negative direction. These modal coefficients can be expressed as vectors $\vec{a}(x)$ and $\vec{b}(x)$.

In order to derive the differential equations that describe the evolution of \vec{a} and \vec{b} in x -direction, the system (3.11) is projected onto the bases \vec{X}_n and $Z_{c,n} \vec{Y}_n$ by

$$\langle \partial_x \vec{X} \mid Z_{c,n} \vec{Y}_n \rangle = \langle \mathbf{F} \vec{Y} \mid Z_{c,n} \vec{Y}_n \rangle \quad (3.31)$$

and

$$\langle \partial_x \vec{Y} \mid \vec{X}_n \rangle = \langle \mathbf{G} \vec{X} \mid \vec{X}_n \rangle \quad (3.32)$$

which leads to a system of coupled differential equations (see [17] for details)

$$\partial_x \vec{a} = \mathbf{N}_1 \vec{a} + \mathbf{N}_2 \vec{b} \quad (3.33)$$

$$\partial_x \vec{b} = \mathbf{N}_3 \vec{a} + \mathbf{N}_4 \vec{b}. \quad (3.34)$$

The matrices \mathbf{N}_1 , \mathbf{N}_2 , \mathbf{N}_3 and \mathbf{N}_4 are given by

$$N_{1,nm} = -\frac{1}{\mathcal{I}_n} \left\langle \partial_x \vec{X}_m \middle| \vec{Y}_n \right\rangle \quad (3.35)$$

$$N_{2,nm} = \frac{ik_n}{Z_{c,n}} \delta_{nm} \quad (3.36)$$

$$N_{3,nm} = ik_n Z_{c,n} \delta_{nm} \quad (3.37)$$

$$N_{4,nm} = \frac{1}{\mathcal{I}_n} \left\{ -\left\langle \partial_x \vec{Y}_m \middle| \vec{X}_n \right\rangle + (\partial_x h_U) \sigma_{xx,m}(\bar{h}) u_{x,n}(\bar{h}) - (\partial_x h_L) \sigma_{xx,m}(-\bar{h}) u_{x,n}(-\bar{h}) \right\} \quad (3.38)$$

where \mathbf{N}_2 and \mathbf{N}_3 describe propagation while the coupling of modes is governed by \mathbf{N}_1 and \mathbf{N}_4 .

The expressions given in (3.36) and (3.37) can be implemented right away. Finding closed analytical expressions for (3.35) and (3.38) by directly evaluating the scalar products is possible but very time consuming and cumbersome. A faster alternative is to evaluate (3.35) and (3.38) by using the properties of the operators \mathbf{F} and \mathbf{G} . This has been done in [17] for plates with symmetrically varying thickness where only coupling of S -modes to S -modes and A -modes to A -modes had to be considered. If N coefficients for symmetric and N coefficients for antisymmetric Lamb-modes are combined into $2N$ -dimensional vectors \vec{a} and \vec{b} for the mode expansion, the matrices \mathbf{N}_1 and \mathbf{N}_4 can be arranged in $N \times N$ blocks

$$\mathbf{N}_{1,4} = \begin{pmatrix} \mathbf{N}_{1,4}^{SS} & \mathbf{N}_{1,4}^{SA} \\ \mathbf{N}_{1,4}^{AS} & \mathbf{N}_{1,4}^{AA} \end{pmatrix}. \quad (3.39)$$

Considering the symmetric properties of the stress and displacement fields given in (3.21) and (3.22) or (3.24) and (3.25) and using the notations $u_{x,n}(\bar{h}) = \mathcal{U}_n$, $u_{y,n}(\bar{h}) = \mathcal{V}_n$, $\sigma_{xx,n}(\bar{h}) = \mathcal{S}_n$ and $\partial_x f = f'$, the elements in the diagonal blocks are

$$N_{1,nn}^{SS,AA} = \frac{-1}{2\mathcal{I}_n} \left\{ \mathcal{I}'_n + \mathcal{I}_n \frac{Z'_{c,n}}{Z_{c,n}} + \bar{h}' \left[\mathcal{U}_n \mathcal{S}_n + i\rho\omega^2 \left(\frac{\mathcal{U}_n^2}{k_n Z_{c,n}} + \frac{Z_{c,n} \mathcal{V}_n^2}{k_n} \right) \right] \right\} \quad (3.40)$$

$$N_{4,nn}^{SS,AA} = \frac{1}{2\mathcal{I}_n} \left\{ -\mathcal{I}'_n + \mathcal{I}_n \frac{Z'_{c,n}}{Z_{c,n}} + \bar{h}' \left[\mathcal{U}_n \mathcal{S}_n + i\rho\omega^2 \left(\frac{\mathcal{U}_n^2}{k_n Z_{c,n}} + \frac{Z_{c,n} \mathcal{V}_n^2}{k_n} \right) \right] \right\} \quad (3.41)$$

for $n = m$ and

$$N_{1,nm}^{SS,AA} = \frac{2\bar{h}'}{(k_m^2 - k_n^2) \mathcal{I}_n} \left\{ -k_m^2 \mathcal{U}_m \mathcal{S}_n + i\rho\omega^2 \left(\frac{k_n \mathcal{U}_m \mathcal{U}_n}{Z_{c,n}} - k_m Z_{c,m} \mathcal{V}_m \mathcal{V}_n \right) \right\} \quad (3.42)$$

$$N_{4,nm}^{SS,AA} = \frac{2\bar{h}'}{(k_m^2 - k_n^2) \mathcal{I}_n} \left\{ -k_n^2 \mathcal{U}_n \mathcal{S}_m + i\rho\omega^2 \left(\frac{k_m \mathcal{U}_m \mathcal{U}_n}{Z_{c,m}} - k_n Z_{c,n} \mathcal{V}_m \mathcal{V}_n \right) \right\} \quad (3.43)$$

for $n \neq m$. In (3.40)-(3.43) both indices n and m refer either to S -modes for the diagonal blocks \mathbf{N}_1^{SS} and \mathbf{N}_4^{SS} or to A -modes for the diagonal blocks \mathbf{N}_1^{AA} and \mathbf{N}_4^{AA} . Using the same notation, the elements of the off-diagonal blocks are

$$N_{1,nm}^{AS,SA} = \frac{2\tilde{h}'}{(k_m^2 - k_n^2)\mathcal{J}_n} \left\{ -k_m^2 \mathcal{U}_m \mathcal{S}_n + i\rho\omega^2 \left(\frac{k_n \mathcal{U}_m \mathcal{U}_n}{Z_{c,n}} - k_m Z_{c,m} \mathcal{V}_m \mathcal{V}_n \right) \right\} \quad (3.44)$$

$$N_{4,nm}^{AS,SA} = \frac{2\tilde{h}'}{(k_m^2 - k_n^2)\mathcal{J}_n} \left\{ -k_n^2 \mathcal{U}_n \mathcal{S}_m + i\rho\omega^2 \left(\frac{k_m \mathcal{U}_m \mathcal{U}_n}{Z_{c,m}} - k_n Z_{c,n} \mathcal{V}_m \mathcal{V}_n \right) \right\} \quad (3.45)$$

where index n refers to S - and m to A -modes for the off-diagonal blocks \mathbf{N}_1^{AS} and \mathbf{N}_4^{AS} and vice versa for the off-diagonal blocks \mathbf{N}_1^{SA} and \mathbf{N}_4^{SA} . The function \mathcal{J}_n which follows from the biorthogonality relation (3.19) is

$$\mathcal{J}_n = \mu \frac{ik_n}{Z_{c,n}} \left\{ \sinh(2\bar{\beta}_n \bar{h}) P(k_n) + (k_n^2 - \bar{\beta}_n^2) \bar{h} \left(1 - \frac{\bar{\beta}_n \sinh(2\bar{\beta}_n \bar{h})}{\bar{\alpha}_n \sinh(2\bar{\alpha}_n \bar{h})} \right) \right\} \frac{1}{\bar{\beta}_n^2} \quad (3.46)$$

for S -modes and

$$\mathcal{J}_n = \mu \frac{ik_n}{Z_{c,n}} \left\{ \sinh(2\bar{\beta}_n \bar{h}) P(k_n) - (k_n^2 - \bar{\beta}_n^2) \bar{h} \left(1 - \frac{\bar{\beta}_n \sinh(2\bar{\beta}_n \bar{h})}{\bar{\alpha}_n \sinh(2\bar{\alpha}_n \bar{h})} \right) \right\} \quad (3.47)$$

for A -modes² with

$$P(k_n) = -\frac{\bar{\beta}_n(k_n^2 - \bar{\beta}_n^2)}{2\bar{\alpha}_n^2} + \frac{\bar{\beta}_n^3}{k_n^2} - \frac{k_n^2}{2\bar{\beta}_n} + \frac{7\bar{\beta}_n}{2} - \frac{8\bar{\beta}_n^3}{k_n^2 + \bar{\beta}_n^2} \quad (3.48)$$

for both S - and A -modes³.

It is easy to see that for plates with symmetrically varying thickness, $\tilde{h} = 0$ and thus (3.44) and (3.45) vanish as expected. The expressions (3.40)-(3.43) have been stated by Pagneux and Maurel in [17] without providing a detailed derivation. Since this step is important for the adaptation to other types of waveguides, the derivation of expressions for the elements of \mathbf{N}_1 and \mathbf{N}_4 by using the properties of the operators \mathbf{F} and \mathbf{G} can be found in Appendix B.

3.2 Solving the differential equations

3.2.1 Transforming the coupled differential equations

In [17], Pagneux and Maurel state that solving the coupled differential equations for \vec{a} and \vec{b} (3.33) and (3.34) directly would be numerically unstable due to the presence

²The factor \bar{h} is missing in the expression for \mathcal{J}_n that was provided in [17] which is likely an error in typesetting. Furthermore, there is no additional factor $1/\bar{\beta}_n^2$ in [17] for symmetric Lamb-modes which is correct if the stress and displacement fields that are derived from the Helmholtz potentials given in (2.14) and (2.15) are used in the calculation. Using the renormalized Helmholtz potentials (3.15)-(3.18) leads to the expressions given in this thesis.

³In [17] the 4th term in (3.48) is given as $7/(2\bar{\beta}_n)$ rather than $(7\bar{\beta}_n)/2$ as obtained from calculations performed in the course of this work. Since the latter version ensures that all terms in (3.48) are of the same unit (1/m) this deviation is most likely caused by a typesetting error in [17]

of evanescent modes and refer to [42] for a more detailed discussion of the inherent problems involved in their numerical treatment. A useful approach to avoid this problem is to introduce an impedance matrix \mathbf{Z} as a linear operator to link the vectors \vec{a} and \vec{b} [17, 42]

$$\vec{b}(x) = \mathbf{Z}(x)\vec{a}(x). \quad (3.49)$$

If (3.49) is inserted into (3.33) and (3.34) this leads to a linear differential equation for \vec{a}

$$\partial_x \vec{a} = (\mathbf{N}_1 + \mathbf{N}_2 \mathbf{Z}) \vec{a} \quad (3.50)$$

and a Riccati matrix differential equation for \mathbf{Z}

$$\partial_x \mathbf{Z} = \mathbf{N}_3 + \mathbf{N}_4 \mathbf{Z} - \mathbf{Z} \mathbf{N}_1 - \mathbf{Z} \mathbf{N}_2 \mathbf{Z}. \quad (3.51)$$

Equation (3.51) has to be solved first with a condition imposed on the end of the waveguide. A simple condition is $\mathbf{Z}(x_{\text{end}}) = \pm \mathbf{Z}_c$ with \mathbf{Z}_c being the characteristic impedance matrix which diagonal elements are defined by (3.23) for S -modes and by (3.26) for A -modes. Using $+\mathbf{Z}_c$ allows only the existence of right going modes at the end of the waveguide which corresponds to a continued waveguide while $-\mathbf{Z}_c$ allows only the existence of left going modes and corresponds to a perfectly reflecting wall at the end of the waveguide. Once $\mathbf{Z}(x)$ has been calculated by solving (3.51), (3.50) can be solved with a starting value that is determined by the desired excitation at the beginning of the waveguide. If solutions for $\mathbf{Z}(x)$ and $\vec{a}(x)$ are known, $\vec{b}(x)$ can be obtained from (3.49).

3.2.2 Solving the Riccati matrix differential equation

Computational methods to solve a Riccati matrix differential equation have been around for some time e.g. the one proposed by Razzaghi [66], however, in this case the elements of matrices \mathbf{N}_1 - \mathbf{N}_4 are not constant in case of a waveguide with varying thickness. Furthermore, comparing (3.40) and (3.41) shows that $\mathbf{N}_1 \neq \mathbf{N}_4^T$ which means that (3.51) is a non-symmetric Riccati matrix differential equation. A survey of properties and conditions on the solvability of symmetric and non-symmetric Riccati matrix differential equations can be found in [67] while [68] lists several methods for the integration of Riccati matrix differential equations with non-constant matrices and investigates their stability in the presence of singularities within the solution. The discussion provided in [68] confirms that the utilization of a Möbius scheme as proposed by Schiff and Shnider [69] is applicable to the problem of solving (3.51). A detailed description of the Möbius method, including an application to several test cases, can be found in [69]. The essential steps in constructing the solver used in this work will be repeated here.

First the problem is discretized in x -direction by $x_{j+1} = x_j + \Delta x$. The Möbius method utilizes the link between a Riccati matrix differential equation and a system of coupled differential equations that has been illustrated in the previous subsection. The system (3.33) and (3.34) can be written as

$$\partial_x \begin{pmatrix} \vec{a}(x) \\ \vec{b}(x) \end{pmatrix} = \begin{pmatrix} \mathbf{N}_1 & \mathbf{N}_2 \\ \mathbf{N}_3 & \mathbf{N}_4 \end{pmatrix} \begin{pmatrix} \vec{a}(x) \\ \vec{b}(x) \end{pmatrix}. \quad (3.52)$$

An implicit or explicit numerical integration method can then be written in the form

$$\begin{pmatrix} \vec{a}_{j+1} \\ \vec{b}_{j+1} \end{pmatrix} = \begin{pmatrix} \tilde{\mathbf{N}}_1 & \tilde{\mathbf{N}}_2 \\ \tilde{\mathbf{N}}_3 & \tilde{\mathbf{N}}_4 \end{pmatrix}_j \begin{pmatrix} \vec{a}_j \\ \vec{b}_j \end{pmatrix} \quad (3.53)$$

where $\tilde{\mathbf{N}}_1$ - $\tilde{\mathbf{N}}_4$ will be constructed in a later step. A scheme for the numerical integration of \mathbf{Z} can be constructed from (3.53)

$$\begin{aligned} \mathbf{Z}_{j+1} &= \vec{b}_{j+1} \vec{a}_{j+1}^{-1} \\ &= \left(\tilde{\mathbf{N}}_{3,j} \vec{a}_j + \tilde{\mathbf{N}}_{4,j} \vec{b}_j \right) \left(\tilde{\mathbf{N}}_{1,j} \vec{a}_j + \tilde{\mathbf{N}}_{2,j} \vec{b}_j \right)^{-1} \\ &= \left(\tilde{\mathbf{N}}_{3,j} \vec{a}_j + \tilde{\mathbf{N}}_{4,j} \vec{b}_j \right) \vec{a}_j^{-1} \left(\tilde{\mathbf{N}}_{1,j} + \tilde{\mathbf{N}}_{2,j} \mathbf{Z}_j \right)^{-1} \\ &= \left(\tilde{\mathbf{N}}_{3,j} + \tilde{\mathbf{N}}_{4,j} \mathbf{Z}_j \right) \left(\tilde{\mathbf{N}}_{1,j} + \tilde{\mathbf{N}}_{2,j} \mathbf{Z}_j \right)^{-1}. \end{aligned} \quad (3.54)$$

Since the integration of \mathbf{Z} has to be performed from back to front, (3.54) has to be inverted to

$$\mathbf{Z}_j = \left(\tilde{\mathbf{N}}_{4,j} - \mathbf{Z}_{j+1} \tilde{\mathbf{N}}_{2,j} \right)^{-1} \left(\mathbf{Z}_{j+1} \tilde{\mathbf{N}}_{1,j} - \tilde{\mathbf{N}}_{3,j} \right). \quad (3.55)$$

In order to implement a solver for the Riccati matrix differential equation based on (3.55), $\tilde{\mathbf{N}}_{1,j}$ - $\tilde{\mathbf{N}}_{4,j}$ have to be constructed. In this work a second order method was used with

$$\tilde{\mathbf{N}}_{1,j} = \mathbb{1} + \frac{\Delta x}{2} (\mathbf{N}_{1,j} + \mathbf{N}_{1,j+1}) + \frac{\Delta x^2}{2} (\mathbf{N}_{1,j}^2 + \mathbf{N}_{2,j} \mathbf{N}_{3,j}) \quad (3.56)$$

$$\tilde{\mathbf{N}}_{2,j} = \frac{\Delta x}{2} (\mathbf{N}_{2,j} + \mathbf{N}_{2,j+1}) + \frac{\Delta x^2}{2} (\mathbf{N}_{1,j} \mathbf{N}_{2,j} + \mathbf{N}_{2,j} \mathbf{N}_{4,j}) \quad (3.57)$$

$$\tilde{\mathbf{N}}_{3,j} = \frac{\Delta x}{2} (\mathbf{N}_{3,j} + \mathbf{N}_{3,j+1}) + \frac{\Delta x^2}{2} (\mathbf{N}_{3,j} \mathbf{N}_{1,j} + \mathbf{N}_{4,j} \mathbf{N}_{3,j}) \quad (3.58)$$

$$\tilde{\mathbf{N}}_{4,j} = \mathbb{1} + \frac{\Delta x}{2} (\mathbf{N}_{4,j} + \mathbf{N}_{4,j+1}) + \frac{\Delta x^2}{2} (\mathbf{N}_{3,j} \mathbf{N}_{2,j} + \mathbf{N}_{4,j}^2). \quad (3.59)$$

where $\mathbb{1}$ denotes the identity matrix. Another possible construction of $\tilde{\mathbf{N}}_{1,j}$ - $\tilde{\mathbf{N}}_{4,j}$ was suggested in [17] by combining the Möbius scheme with a Magnus method as described e.g. in [70]. In this Magnus-Möbius method $\tilde{\mathbf{N}}_1$ - $\tilde{\mathbf{N}}_4$ would be determined by

$$\begin{pmatrix} \tilde{\mathbf{N}}_1 & \tilde{\mathbf{N}}_2 \\ \tilde{\mathbf{N}}_3 & \tilde{\mathbf{N}}_4 \end{pmatrix} = \exp \left(\begin{pmatrix} \mathbf{N}_1 & \mathbf{N}_2 \\ \mathbf{N}_3 & \mathbf{N}_4 \end{pmatrix} \Delta x \right). \quad (3.60)$$

While (3.60) can be expected to be more accurate, the necessity to compute a matrix exponential introduces an additional possible source of numerical errors. A good overview on different methods to compute the matrix exponential and their respective properties is provided in [71]. While in the course of this work some test simulations have been carried out with the 2nd order Möbius as well as the Magnus-Möbius method using the pre-implemented MATLAB function to calculate matrix exponentials, no notable difference

could be observed in the results. For sufficiently complicated problems the use of the Magnus-Möbius method might in fact be necessary and in this case further investigations should be conducted in order to determine the most suited method to calculate a matrix exponential for use in the solver for Riccati matrix differential equations.

3.2.3 Solving the linear differential equation

In an early stage of this work, a solver for the linear differential equation was constructed by discretizing (3.50) into

$$\frac{\vec{a}_{j+1} - \vec{a}_j}{\Delta x} = \mathbf{M}_{j+\frac{1}{2}} \vec{a}_{j+\frac{1}{2}} \quad (3.61)$$

with $\mathbf{M} = \mathbf{N}_1 + \mathbf{N}_2 \mathbf{Z}$. Using the interpolations

$$\mathbf{M}_{j+\frac{1}{2}} = \frac{\mathbf{M}_j + \mathbf{M}_{j+1}}{2} \quad (3.62)$$

and

$$\vec{a}_{j+\frac{1}{2}} = \frac{\vec{a}_j + \vec{a}_{j+1}}{2} \quad (3.63)$$

we find

$$\vec{a}_{j+1} = (4\mathbb{1} - \Delta x(\mathbf{M}_{j+1} + \mathbf{M}_j))^{-1} (4\mathbb{1} + \Delta x(\mathbf{M}_{j+1} + \mathbf{M}_j)) \vec{a}_j \quad (3.64)$$

as a simple solver that can be implemented right away⁴. In cases where higher accuracy is required a suitable alternative is

$$\vec{a}_{j+1} = \left(\tilde{\mathbf{N}}_{1,j+\frac{1}{2}} + \tilde{\mathbf{N}}_{2,j+\frac{1}{2}} \mathbf{Z}_j \right) \vec{a}_j \quad (3.65)$$

with $\tilde{\mathbf{N}}_1$ and $\tilde{\mathbf{N}}_2$ being constructed in accordance with the Magnus-Möbius method (3.60) [17]. While both solvers (3.64) and (3.65) produced satisfactory results for simple test cases, (3.65) was used in the final implementation for simulations with more than one propagating mode.

3.3 On the accuracy of wave numbers

3.3.1 Estimate of relative error

Since the spectral decomposition method is based on a series expansion of the displacement fields in eigenfunctions of the Laplace operator, its accuracy will depend on the number of elements N after which this expansion is truncated⁵. By comparing the relative

⁴This construction bears some similarities to the Crank-Nicolson method. However, even though the solver described by (3.64) was successfully applied for a good part of this work, it is important to note that a proper application of the Crank-Nicolson scheme would yield $(\vec{a}_{j+1} - \vec{a}_j)/\Delta x = (\mathbf{M}_{j+1}\vec{a}_{j+1} + \mathbf{M}_j\vec{a}_j)/2$ and lead to $\vec{a}_{j+1} = (2\mathbb{1} - \Delta x\mathbf{M}_{j+1})^{-1}(2\mathbb{1} + \Delta x\mathbf{M}_j)\vec{a}_j$ which might provide more accurate results than (3.64). This discrepancy went unnoticed until after (3.64) was replaced by (3.65) in the implementation used for the simulations documented in this thesis.

⁵Which also determines the dimension of the eigenvalue problem and thus the number of modes that can be calculated.

errors in symmetric Lamb-modes for a range up to $N = 100$ it was shown by Pagneux and Maurel that the spectral decomposition method converges in fact with $1/N$ [62]. In [46] the relative errors have been investigated over a range of frequencies for different values of N which lead to

$$\left| \frac{\Delta k}{k} \right| = \frac{1}{5N} \left(\frac{f}{2} + 1 \right) \quad (3.66)$$

as an estimate for the relative error. While (3.66) confirms the $1/N$ dependence, it also shows that the relative error will increase for large frequencies f .

3.3.2 Anomaly in the modes of lowest order

When the wave numbers are calculated as described in Chapter 2, some care has to be taken with the S_0 and A_0 mode of a plate as well as with the $L(0,0)$ and $L(0,1)$ mode of a cylindrical rod or hollow cylinder. While these modes are supposed to approach the phase velocity of a Rayleigh wave for high frequencies, calculations using the spectral decomposition method will provide a local minimum at the Rayleigh wave velocity in the dispersions curves of these modes before they asymptotically approach the phase velocity of transverse waves. This anomaly was discussed in [46] and can be dealt with in two ways. The first way is to increase the number of modes N that are calculated and thus the overall accuracy of the spectral decomposition method. This will in fact cause the calculated dispersion curves to stay close to the correct results over an extended range of frequency and to raise up more slowly to the wrong asymptotic value if the frequency is increased too far. The second method to mitigate the effect of that anomaly can be applied if the dispersion curves are to be calculated over a range of frequencies starting with a sufficiently low one⁶. The procedure requires to switch to the phase velocity frequency space and ensure that the phase velocity of the S_0 mode (or the $L(0,1)$ mode) is monotonically decreasing with increasing frequency and that the phase velocity of the A_0 mode (or $L(0,0)$ mode) is smaller than that of the corrected S_0 mode (or $L(0,1)$ mode) before switching back to the wave number frequency space.

3.3.3 Achieving the required accuracy

The validity of some expressions that have been derived in the multimodal method (e.g. for the off-diagonal elements of \mathbf{N}_1 and \mathbf{N}_4) depends on the identities (3.23) and (3.26). As can be seen, these identities correspond to the dispersion relations for S - and A -modes (2.25) and (2.31) which means they hold true for wave numbers k_n that are roots of those dispersion relations. As a consequence, the entire numerical evaluation of the multimodal method will break down if the value of the dispersion relation is not sufficiently close to zero for a given wave number k_n which is supposed to be on the dispersion curve of a Lamb-mode. In other words, if the numerical determination of wave numbers is done with insufficient accuracy, the application of the multimodal method as a whole will fail.

⁶Meaning a frequency at which the calculated dispersion curve for the modes in question is still close to the correct result.

If the frequency is increased, an increasing number of roots of the dispersion relation is closely packed near the wave number of shear waves k_T (see Figure 2.4 for an illustration). Furthermore, the dispersion relation becomes increasingly steep between two neighbouring roots. This means that, especially for Lamb-modes of lower order, at high frequencies even a small numerical deviation from the actual root might result in a rather large value of the dispersion relation. Beyond a critical frequency, even calculations up to the machine epsilon will not be sufficient anymore which puts a hard limit on the applicability of the multimodal method as far as the range of frequencies is concerned. It has already been mentioned in Chapter 2 that the numerical computation of wave numbers based on the spectral decomposition method is not overly impressive in terms of accuracy. As can be seen from (3.66) the accuracy can be improved by increasing the number of calculated modes N , however, a more expedient approach is to follow the suggestion given in [62] to treat the spectral decomposition method as a provider of relatively accurate initial guess values.

The approach to improve calculated wave numbers to the required accuracy is twofold. First a minimum initial accuracy is imposed by ensuring that even if only a small number of modes have to be evaluated, the calculation is done with at least $N = 20$. Secondly the values obtained with the spectral decomposition method are used as a starting point for iterative root finding procedures such as a bracketing method for real wave numbers and the method of steepest descent⁷ for complex wave numbers. Since the required accuracy depends on frequency as well as the order of the evaluated mode, no fixed threshold for the accuracy is set in the implementation used in this work. Instead at each iterative step, the dispersion relation is tested with the current k_n . If the value of the dispersion relation drops below 10^{-5} , the iteration is stopped. If the iterative procedure runs into a dead end without achieving the required accuracy, a warning is issued together with the last value of the dispersion relation.

While these iterative procedures, which have to be performed for every point of the dispersion curve of every individual mode, do partially negate the spectral decomposition method's main advantage of short computation times, it is still more efficient and reliable than a blind root search would be⁸.

3.4 Concerning Cutoffs

Cutoffs are points in the dispersion curves at which a wave mode switches its behaviour from evanescent to propagating or vice versa (i.e. the wave number k_n is real before or after the cutoff). Two cases of Cutoffs can be distinguished. The first case are Cutoffs at which a single mode switches its behaviour at $k_n = 0$. These Cutoffs will be

⁷The method of steepest descent is used to find local minima in the absolute values of the dispersion relation which can be treated as 2-dimensional function if complex wave numbers are considered. In each iteration a search for the minimum in direction of the negative local gradient at the starting point is performed. This minimum is then used as starting point for the next iterative step.

⁸For reasons that have been mentioned in Chapter 2

referred to as regular Cutoffs in accordance with [12]. The second case are Cutoffs at which two neighbouring modes coincide at a non-zero wave number k_n while turning into propagating modes. These cases will be called irregular Cutoffs in accordance with [12]. Both cases are illustrated in Figure 3.1⁹.

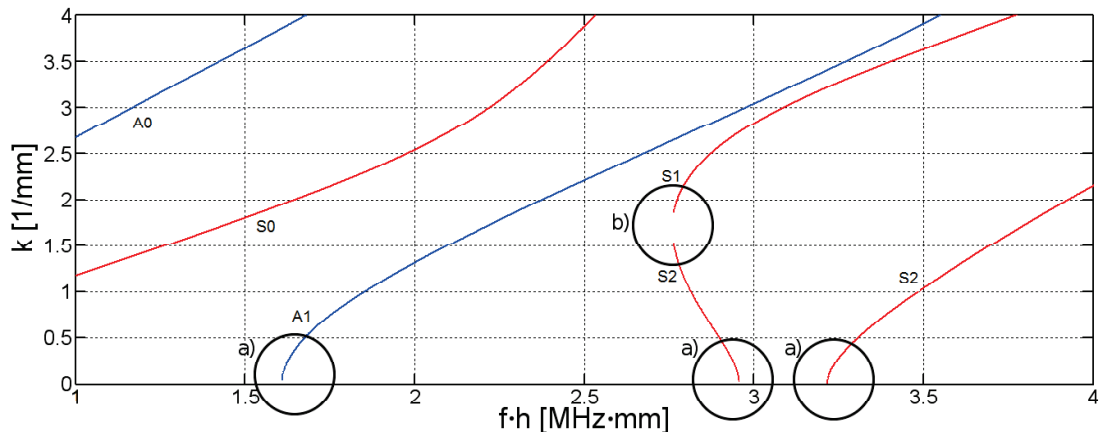


Figure 3.1: Section of the real parts of dispersion curves in a plate with a) regular and b) irregular Cutoffs.

The wave number k_n of a guided wave mode depends on the waveguide's thickness at any given frequency, if this thickness is a function of x then so is k_n . If (3.40)-(3.45) are implemented, a numerical differentiation of k_n in x -direction has to be performed which was done using finite differences of higher order¹⁰ in this work. While $k_n(x)$ will be continuous when crossing a Cutoff cross-section, it will usually not be differentiable at the Cutoff itself. Therefore, some care has to be taken in order to avoid numerical artifacts at Cutoffs. As a first step, Cutoffs have to be detected within the numerically determined $k_n(x)$ which is done by searching for positions at which the imaginary part vanishes. The function $k_n(x)$ is then split at these points in order to ensure that numerical differentiation is only applied piecewise on continuous, differentiable segments.

3.4.1 Regular Cutoffs

Although the renormalization of Lamb-modes that has been suggested in [17] prevents numerical instabilities at regular Cutoffs, the solver that is used on the differential equations might still produce inaccurate results near a Cutoff cross-section which result in discontinuities (i.e. a slight jump in modal coefficients $\mathbf{Z}(x)$). Since the positions of Cutoff cross-sections had to be identified in the numerical differentiation of $k_n(x)$, this

⁹The gap between the S_1 - and S_2 -mode at the irregular Cutoff marked as b) arises from the resolution of different frequencies and would become smaller for a finer frequency step size Δf .

¹⁰Usually a central difference of 6th order is applied at the inner points of $k_n(x)$ while 6th order backward difference and forward difference are used at beginning and end respectively.

problem can easily be solved by using a Taylor or Padé approximation to extrapolate over regular Cutoffs instead of integrating over these critical points via solver.

3.4.2 Irregular Cutoffs

At an irregular Cutoff, two different guided wave modes coincide. The close proximity of two neighbouring modes near an irregular Cutoff can lead to problems in the iterative improvement of wave number accuracy. In order to prevent the iterative procedure from converging towards the wrong root of the dispersion relation, some care has to be taken in choosing the interval on which the iterative root search is performed. A useful property of the spectral decomposition method is the observation that with increasing N , wave numbers in monotonically increasing branches of dispersion curves converge from below while wave numbers on monotonically decreasing branches of dispersion curves converge from above. In this work, satisfactory results have been obtained by running the iterative improvement from high to low frequencies and at each frequency (except the highest one) using the aforementioned property of the spectral decomposition method as well as the results of the iterative improvement at the previous frequency to select proper boundaries for the root search.

A more significant problem is that at irregular Cutoffs the guided wave modes of the corresponding waveguide with constant thickness do not form a complete orthogonal basis anymore which means that the multimodal method will break down at these points. Since the solver that is used on the differential equations runs into a singularity at irregular Cutoffs¹¹, a simple extrapolation over these points, as used for regular Cutoffs, will not be sufficient. While there are several possible approaches to address it, the treatment of irregular Cutoffs in the multimodal method remains somewhat an open problem and will be discussed in more detail in Chapter 6.

3.5 Pulse Propagation

The multimodal method as described so far would calculate the steady state displacement fields. Since the goal of this work is to establish a tool for the simulation of pulse propagation through a waveguide with varying thickness, some modifications have to be applied. First the previously omitted time-dependence has to be reintroduced by adding an oscillating term $e^{i\omega t}$ to the stationary solution for the displacement fields. This corresponds to a continuous wave solution which would result from an excitation with a single frequency. A pulse propagation can now be simulated by simply overlapping a sufficient number of continuous wave solutions. The general scheme of that procedure is illustrated in Figure 3.2.

¹¹A solver using the Möbius method as described in (3.54) is in principle capable to integrate over singularities in the solution [69], however, the breakdown of the orthogonal basis causes singularities within the matrices \mathbf{N}_1 - \mathbf{N}_4 as well so that no meaningful results can be obtained close to an irregular Cutoff.

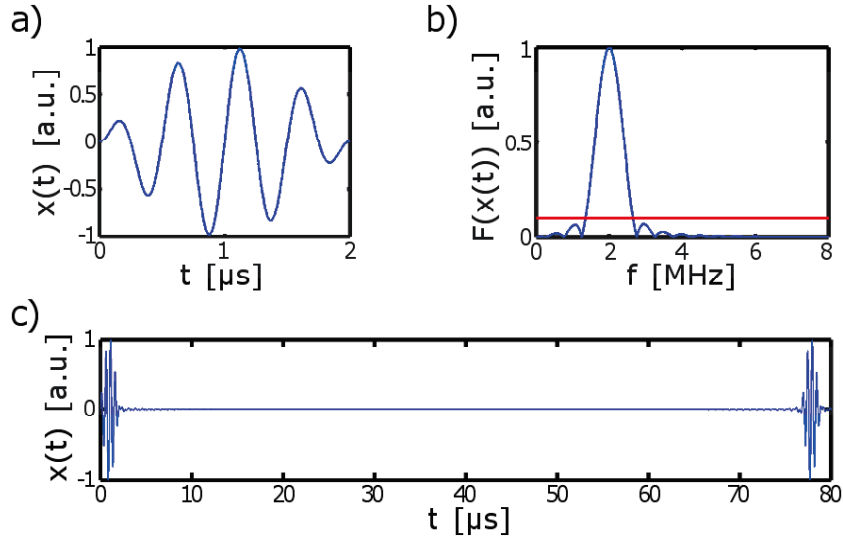


Figure 3.2: Implementation of pulse propagation including a) modelling of an excitation pulse, b) reducing the spectrum to a finite number of frequencies and c) reconstructing the pulse excitation as superposition of continuous wave solutions.

After the desired excitation pulse has been modelled (e.g. a sine burst pulse as shown in Figure 3.2 a)), a Fast Fourier Transform (FFT) is applied to transform it to the frequency domain. The spectrum is then reduced to a finite number of frequencies by discarding all contributions below 10% of the center frequency as illustrated in Figure 3.2 b). In a last step continuous wave solutions are calculated for the remaining frequencies and overlapped according to their relative weights within the frequency spectrum. The modelled excitation pulse is reconstructed where the continuous wave solutions overlap constructively and dispersive behaviour of the wave package is automatically modelled in accordance with the calculated dispersion curves. Since overlapping a finite number of periodic functions will always result in another periodic function, the reconstructed excitation is in fact a pulse series rather than a single pulse (see Figure 3.2 c)). Therefore some care has to be taken in adjusting the resolution and threshold in the reduced spectrum to ensure that at any given time only one pulse is propagating within the modelled geometry of the waveguide.

3.6 Reproduction of previously published results

In order to verify that the multimodal method was correctly implemented for plates, some of the results published by Pagneux and Maurel in [17] for displacement fields in plates with symmetrically varying thickness have been reproduced. The material properties used in this simulation were defined by the density $\rho = 1 \text{ mg/mm}^3$, the phase velocity for longitudinal waves $c_L = 2/\pi\sqrt{2(1-\nu)/(1-2\nu)} \text{ mm}/\mu\text{s}$, the phase velocity for shear waves $c_T = 2/\pi \text{ mm}/\mu\text{s}$ and the Poisson ratio $\nu = 0.31$. The geometry of the waveguide

is defined by

$$h_U(x) = -h_L(x) = h_0 + (h_1 - h_0)e^{-\frac{x^2}{L^2}} \quad (3.67)$$

with $h_0 = 0.7$ mm, $h_1 = 1.5$ mm and $L = 1.5$ mm. Only contributions of antisymmetric Lamb-modes have been taken into account and only the A_0 -mode is excited at the front face of the waveguide but a total of eleven modes is used in the subsequent calculations.

Figure 3.3 shows the displacement field in x -direction for the excitation frequency $\omega = 0.5$ MHz. The A_0 is the only propagating mode in this test case which corresponds to the one documented in [17]: Figure 4a.

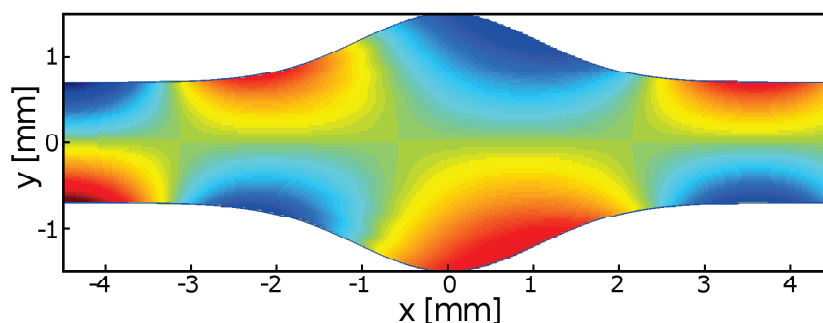


Figure 3.3: Displacement field in x -direction for $\omega = 0.5$ MHz with red for positive and blue for negative displacement.

The displacement field in x -direction for the excitation frequency $\omega = 1.37$ MHz is plotted in Figure 3.4. In this case, the A_0 -mode is propagating throughout the entire waveguide while the A_1 -mode hits two Cutoff cross-sections within the waveguide which are located symmetrically around $x = 0$ thus becoming what Pagneux and Maurel referred to as a trapped mode [17]. This test case corresponds to the one shown in [17]: Figure 4b.

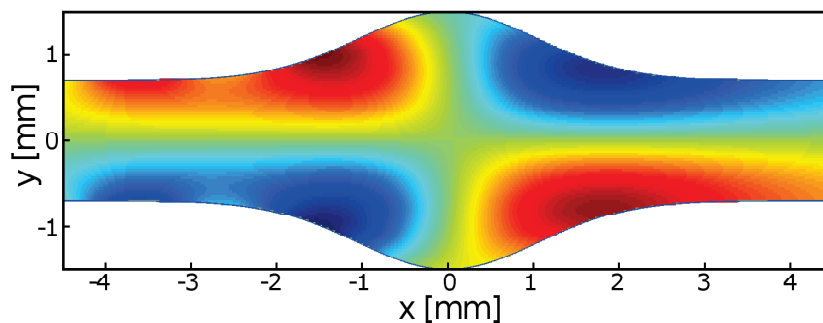


Figure 3.4: Displacement field in x -direction for $\omega = 1.37$ MHz with red for positive and blue for negative displacement.

For the third test case, the displacement field in x -direction was simulated for the excita-

tion frequency $\omega = 1.5$ MHz. The results are shown in Figure 3.5. The A_0 - and A_1 -mode are both propagating modes throughout the entire waveguide with no other mode hitting a Cutoff. Although only the A_0 -mode is excited initially, the A_0 and A_1 are coupled throughout the waveguide due to its continuously varying thickness and therefore both contribute to the displacement field. This corresponds to [17]: Figure 4c.

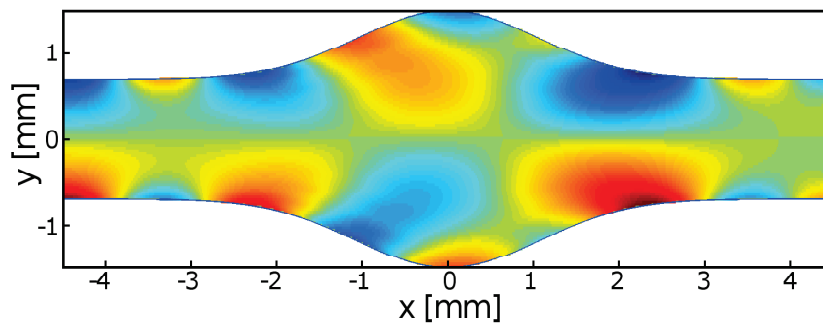


Figure 3.5: Displacement field in x -direction for $\omega = 1.5$ MHz with red for positive and blue for negative displacement.

In general the results obtained in this work for the test cases documented in Figures 3.3-3.5 are in good agreement with the results published in [17]: Figure 4a-4c. Thus it can be concluded that the implementation of the multimodal method used in this work is equivalent to the one used by Pagneux and Maurel for the case of plates with symmetrically varying thickness. Further validation, especially for waveguides other than plates with symmetrically varying thickness, will be provided in Chapter 5.

Chapter 4

Adaptation to cylindrical structures

4.1 Dispersion relations of axially symmetric guided waves

The adaptation of the spectral decomposition method to the calculation of complex dispersion curves has been covered in detail in [46], however, since the calculation of wave numbers is vital to the application of the multimodal approach, the most important points will be repeated in this section. Since the scope of this work is limited to axially symmetric longitudinal modes (L -modes), only two displacement fields (u_r and u_z) have to be considered. The general outline of the spectral decomposition method is the same as described in Chapter 2. In cylindrical coordinates and under the assumption of free propagation in z -direction the wave equation for the displacement vector \vec{u} (2.7) leads to

$$(k^2 - k_T^2)u_r - ik(\gamma - 1)\partial_r u_z - \gamma\partial_r\left(\frac{1}{r}\partial_r(ru_r)\right) = 0 \quad (4.1)$$

and

$$(k^2 - k_L^2)u_z - ik\frac{\gamma - 1}{\gamma r}\partial_r(ru_r) - \frac{1}{\gamma r}\partial_r(r\partial_r u_z) = 0 \quad (4.2)$$

where k_L and k_T are the longitudinal and transversal wave number respectively and γ is a function of the Lamé constants as defined in Chapter 2. With σ and ϵ taking the form given in (2.32) and (2.33), the identities

$$\partial_r u_r(R) = -\frac{\gamma - 2}{\gamma}\left(ik u_z(R) + \frac{u_r(R)}{R}\right) \quad (4.3)$$

and

$$\partial_r u_z(R) = -ik u_r(R) \quad (4.4)$$

are obtained from the boundary condition of a traction free lateral surface at a given radius $r = R$. The remaining steps to determine the complex wave numbers for cylindrical structures are to find suitable orthogonal bases for the spectral decomposition

$$u_r = \sum_n U_n \chi_n(y) \quad (4.5)$$

$$u_z = \sum_n V_n \psi_n(y) \quad (4.6)$$

for cylindrical rods and hollow cylinders and to project (4.1) and (4.2) onto these bases in order to determine the entries of the matrices **A**, **B**, **C** and **D**.

4.1.1 Cylindrical rods

As in Chapter 2 the orthogonal bases are obtained as eigenfunctions of the Laplace operator on the cross-section which essentially means solving the Helmholtz equation

$$\frac{1}{r} \partial_r (r \partial_r \psi_n) = -\phi_n^2 \psi_n \quad (4.7)$$

which can be written as the Bessel differential equation and yields the general solution

$$\psi_n = A J_0(\phi_n r) + B Y_0(\phi_n r) \quad (4.8)$$

where A and B have to be determined by boundary conditions at $r = 0$ and the outer radius of the cylindrical rod $r = R$. To avoid singularities at the central axis of the rod, the boundary condition at $r = 0$ has to be fixed as

$$\partial_r \psi_n(0) = 0. \quad (4.9)$$

Applying a von Neumann like boundary condition

$$\partial_r \psi_n(R) = 0 \quad (4.10)$$

at the outer radius $r = R$ leads to a set of normalized orthogonal functions of the form

$$\psi_n = \frac{J_0(\phi_n r)}{\sqrt{\pi R} J_0(\phi_n R)} \quad (4.11)$$

where the eigenvalues ϕ_n are roots of $J_1(\phi_n R)$. Since these functions are eigenfunctions of a classical Sturm-Liouville problem, they form a complete basis (see e.g. [72]). Using a Dirichlet like boundary condition

$$\psi_n(R) = 0 \quad (4.12)$$

leads to a different set of eigenvalues which are determined as roots of $J_0(\theta_n R)$ but otherwise to a basis similar to (4.11). However, it is possible to find a second set of orthogonal functions belonging to these eigenvalues which reads

$$\chi_n = \frac{J_1(\theta_n r)}{\sqrt{\pi R} J_1(\theta_n R)} \quad (4.13)$$

and satisfies the boundary conditions

$$\chi_n(0) = 0 \quad (4.14)$$

at $r = 0$ and

$$\left(\frac{1}{r}\partial_r(r\chi_n)\right)(R) = 0 \quad (4.15)$$

at $r = R$ thereby still meeting the requirements of a Sturm-Liouville problem and thus providing the second basis needed to apply the spectral decomposition method to cylindrical rods. Projecting (4.2) onto ψ_n and (4.1) onto χ_n yields the following expressions for the entries of the matrices **A**, **B**, **C** and **D**

$$A_{nm} = \frac{2i}{\gamma R} \left(\frac{\phi_n^2 + (\gamma - 2)\theta_m^2}{\phi_n^2 - \theta_m^2} \right) \quad (4.16)$$

$$B_{nm} = \left(\frac{\phi_n^2}{\gamma} - k_L^2 \right) \delta_{nm} \quad (4.17)$$

$$C_{nm} = -\gamma A_{mn} \quad (4.18)$$

$$D_{nm} = (\gamma\theta_n^2 - k_T^2) \delta_{nm} - \frac{4}{R^2}. \quad (4.19)$$

4.1.2 Hollow cylinders

The Helmholtz equation (4.7) and its general solution (4.8) remain valid for hollow cylinders, however, the boundary conditions which are used to determine the coefficients in (4.8) have to be adjusted. For $R_O = R_I + d$ and $R_I \rightarrow \infty$ the L -modes of a hollow cylinder will become identical to the guided wave modes of a plate under plane strain approximation¹ with R_O and R_I taking the role of upper and lower plate surface respectively. On the other hand a cylindrical rod can be seen as a special case of a hollow cylinder with $R_I = 0$. If a plate under plane strain assumption and a cylindrical rod are viewed as the extremal cases, the description of the hollow cylinder must reflect the transition between these two structures. On the plate, von Neumann boundary conditions are applied on upper and lower surface for the first basis and Dirichlet boundary conditions for the second basis. For cylindrical rods, a von Neumann boundary condition was used at $r = R$ for the first and a Dirichlet boundary condition for the second basis while the boundary condition at $r = 0$ had to be fixed as a von Neumann type boundary condition. As a consequence the first basis for the spectral decomposition of a hollow cylinder can be obtained by simply using von Neumann type boundary conditions at $r = R_I$ and $r = R_O$. The resulting normalized orthogonal basis is given by

$$\psi_1 = \frac{1}{\sqrt{\pi}} \frac{1}{\sqrt{R_O^2 - R_I^2}} \quad (4.20)$$

and

$$\psi_{n>1} = \frac{\sqrt{\pi}}{2} \phi_n \frac{Y_1(\phi_n R_I) Y_1(\phi_n R_O)}{\sqrt{Y_1^2(\phi_n R_I) - Y_1^2(\phi_n R_O)}} \left(J_0(\phi_n r) - \frac{J_1(\phi_n R_I)}{Y_1(\phi_n R_I) Y_0(\phi_n r)} \right). \quad (4.21)$$

¹It can be shown that in the formulation of the spectral decomposition method, the expressions for L -modes in a hollow cylinder will indeed decouple into A - and S -modes of a plate [46].

For $n > 1$ the eigenvalues ϕ_n are obtained by evaluating

$$J_1(\phi_n R_O)Y_1(\phi_n R_I) - J_1(\phi_n R_I)Y_1(\phi_n R_O) = 0 \quad (4.22)$$

while the first eigenvalue is $\phi_1 = 0$ (see also [46]).

If Dirichlet type boundary conditions are applied for ψ_n on both the inner and the outer lateral surface, we find an implied second basis χ_n which fulfills the boundary conditions

$$\left(\frac{1}{r}\partial_r(r\chi_n)\right)(R_{I,O}) = 0. \quad (4.23)$$

By comparing (4.23) to (4.14) and (4.15), we find that the boundary condition at the inner radius $r = R_I$ has to contain a transition between a Dirichlet and a von Neumann like boundary condition. A general formulation for a mixed boundary condition that is still in accordance with a Sturm-Liouville problem is [72]

$$\sqrt{1 - S_\vartheta^2}\chi_n(R_I) + S_\vartheta R_I \partial_r \chi_n(R_I) = 0 \quad (4.24)$$

where S_ϑ denotes the sine of the mixing angle ϑ . In order to transform (4.24) into the appropriate boundary conditions for plates and cylindrical rods, $S_\vartheta = 0$ for $R_I = 0$ and $S_\vartheta = 1/\sqrt{2}$ for $R_I \rightarrow \infty$ have to be fulfilled. The results of investigations conducted over the course of this work suggest that

$$S_\vartheta = \frac{1}{\sqrt{2}} \left(1 - \frac{R_O - R_I}{R_O + R_I}\right) \quad (4.25)$$

is a reasonably good choice to model the desired transition with sufficient accuracy [46]. The set of orthogonal functions that form the second basis is

$$\chi_n = \frac{\sqrt{\pi}}{2} \theta_n \frac{Y_0(\theta_n R_O)}{\sqrt{T_n(R_O, R_I)}} \left(\Gamma_n J_1(\theta_n r) - \tilde{\Gamma}_n Y_1(\theta_n r)\right) \quad (4.26)$$

with

$$\Gamma_n = S_\vartheta \theta_n R_I Y_0(\theta_n R_I) - \left(\sqrt{1 - S_\vartheta^2} - S_\vartheta\right) Y_1(\theta_n R_I) \quad (4.27)$$

$$\tilde{\Gamma}_n = S_\vartheta \theta_n R_I J_0(\theta_n R_I) - \left(\sqrt{1 - S_\vartheta^2} - S_\vartheta\right) J_1(\theta_n R_I) \quad (4.28)$$

and

$$\begin{aligned} T_n(R_O, R_I) = & S_\vartheta^2 \theta_n^2 R_I^2 (Y_0^2(\theta_n R_I) - Y_0^2(\theta_n R_O)) \\ & - 2S_\vartheta \left(\sqrt{1 - S_\vartheta^2} - S_\vartheta\right) (\theta_n R_I Y_0(\theta_n R_I) Y_1(\theta_n R_I) - Y_0^2(\theta_n R_O)) \\ & + \left(\sqrt{1 - S_\vartheta^2} - S_\vartheta\right)^2 (Y_1^2(\theta_n R_I) - Y_0^2(\theta_n R_O)). \end{aligned} \quad (4.29)$$

The eigenvalues θ_n are determined by

$$\begin{aligned} & \left(\sqrt{1 - S_\vartheta^2} - S_\vartheta \right) (J_0(\theta_n R_O) Y_1(\theta_n R_I) - J_1(\theta_n R_I) Y_0(\theta_n R_O)) \\ & - S_\vartheta \theta_n R_I (J_0(\theta_n R_O) Y_0(\theta_n R_I) - J_0(\theta_n R_I) Y_0(\theta_n R_O)) = 0. \end{aligned} \quad (4.30)$$

The following expressions for the entries of the matrices **A**, **B**, **C** and **D** are obtained by projecting (4.2) onto ψ_n and (4.1) onto χ_n

$$A_{1m} = \frac{2i}{\gamma} \frac{\Gamma_m - S_\vartheta \theta_m R_I Y_0(\theta_m R_O)}{\sqrt{T_m(R_O, R_I)} (R_O^2 - R_I^2)} (2 - \gamma) \quad (4.31)$$

$$A_{nm} = \frac{Y_1(\phi_n R_I) \Gamma_m - S_\vartheta \theta_m R_O Y_1(\phi_n R_O) Y_0(\theta_m R_O)}{\sqrt{T_m(R_O, R, I)} (Y_1^2(\phi_n R_I) - Y_1^2(\phi_n R_O))} \frac{2i}{\gamma R_O} \left(\frac{\phi_n^2 + (\gamma - 2)\theta_m^2}{\theta_m^2 - \phi_n^2} \right) \quad (4.32)$$

$$B_{nm} = \left(\frac{\phi_n^2}{\gamma} - k_L^2 \right) \delta_{nm} \quad (4.33)$$

$$C_{nm} = -\gamma A_{mn} \quad (4.34)$$

$$\begin{aligned} D_{nm} = & (\gamma \theta_m^2 - k_T^2) \delta_{nm} - \frac{4}{R_O^2} \frac{\Gamma_m \Gamma_n}{\sqrt{T_m(R_O, R_I) T_n(R_O, R_I)}} \\ & - 2S_\vartheta \theta_m \theta_n \frac{Y_0(\theta_m R_O) Y_0(\theta_n R_O)}{\sqrt{T_m(R_O, R_I) T_n(R_O, R_I)}} \left(\gamma \sqrt{1 - S_\vartheta^2} - (\gamma + 2) S_\vartheta \right). \end{aligned} \quad (4.35)$$

4.2 Multimodal method

The general outline for the multimodal method remains the same as described in [17] for plates. The matrix operators have to be adapted to cylindrical coordinates and the basis used in the modal expansion has to be chosen to fit cylindrical rods or hollow cylinders respectively. The starting point of the multimodal method is still the general equation of motion as described in (3.1). For cylindrical coordinates the divergence of the stress tensor $\boldsymbol{\sigma}$ takes the form

$$\operatorname{div}(\boldsymbol{\sigma}) = \begin{pmatrix} \frac{1}{r} \partial_r (r \sigma_{rr}) + \frac{1}{r} (\partial_\varphi \sigma_{r\varphi} - \sigma_{\varphi\varphi}) + \partial_z \sigma_{rz} \\ \frac{1}{r} \partial_r (r \sigma_{r\varphi}) + \frac{1}{r} (\partial_\varphi \sigma_{\varphi\varphi} + \sigma_{r\varphi}) + \partial_z \sigma_{\varphi z} \\ \frac{1}{r} \partial_r (r \sigma_{rz}) + \frac{1}{r} \partial_\varphi \sigma_{\varphi z} + \partial_z \sigma_{zz} \end{pmatrix}. \quad (4.36)$$

Using (2.1), (2.2) and the strain tensor as given in (2.33), the components of the stress tensor can be expressed in terms of displacement fields and Lamé constants. For axially symmetric longitudinal waves (L -modes) this yields

$$\sigma_{rr} = (\lambda + 2\mu) \partial_r u_r + \lambda \left(\frac{u_r}{r} + \partial_z u_z \right) \quad (4.37)$$

$$\sigma_{\varphi\varphi} = (\lambda + 2\mu) \frac{u_r}{r} + \lambda (\partial_r u_r + \partial_z u_z) \quad (4.38)$$

$$\sigma_{zz} = (\lambda + 2\mu)\partial_z u_z + \lambda \left(\frac{u_r}{r} + \partial_r u_r \right) \quad (4.39)$$

$$\sigma_{rz} = \mu(\partial_z u_r + \partial_r u_z) \quad (4.40)$$

and

$$\sigma_{r\varphi} = \sigma_{\varphi z} = 0. \quad (4.41)$$

As we can see, the only relevant displacement fields for our problem are u_r and u_z . From (4.37)-(4.40) as well as (3.1) and (4.36), the expressions

$$\sigma_{rr} = f_1 \sigma_{zz} + f_2 \left(\frac{1}{r} \partial_r (r u_r) \right) - 2\mu \frac{u_r}{r} \quad (4.42)$$

$$\sigma_{\varphi\varphi} = f_1 \sigma_{zz} + f_2 \left(\frac{1}{r} \partial_r (r u_r) \right) - 2\mu \partial_r u_r \quad (4.43)$$

$$\partial_z u_r = -\partial_r u_z + \frac{1}{\mu} \sigma_{rz} \quad (4.44)$$

$$\partial_z u_z = -f_1 \frac{1}{r} \partial_r (r u_r) + \frac{f_1}{\lambda} \sigma_{zz} \quad (4.45)$$

$$\partial_z \sigma_{rz} = -\rho\omega^2 u_r - f_2 \partial_r \left(\frac{1}{r} \partial_r (r u_r) \right) - f_1 \partial_r \sigma_{zz} \quad (4.46)$$

and

$$\partial_z \sigma_{zz} = -\rho\omega^2 u_z - \frac{1}{r} \partial_r (r \sigma_{rz}) \quad (4.47)$$

are obtained with $f_1 = \lambda/(\lambda+2\mu)$ and $f_2 = 4\mu(\lambda+\mu)/(\lambda+2\mu)$ as in the implementation for plates that was described in Chapter 3. If we define $\vec{X} = (u_z, \sigma_{rz})^T$ and $\vec{Y} = (-\sigma_{zz}, u_r)^T$, (4.44)-(4.47) can be written as

$$\partial_z \begin{pmatrix} \vec{X} \\ \vec{Y} \end{pmatrix} = \begin{pmatrix} 0 & \mathbf{F} \\ \mathbf{G} & 0 \end{pmatrix} \begin{pmatrix} \vec{X} \\ \vec{Y} \end{pmatrix} \quad (4.48)$$

where the matrix operators \mathbf{F} and \mathbf{G} take the form

$$\mathbf{F} = \begin{pmatrix} -\frac{f_1}{\lambda} & -f_1 \frac{1}{r} \partial_r (r \cdot) \\ f_1 \partial_r & -\rho\omega^2 - f_2 \partial_r \left(\frac{1}{r} \partial_r (r \cdot) \right) \end{pmatrix} \quad (4.49)$$

$$\mathbf{G} = \begin{pmatrix} \rho\omega^2 & \frac{1}{r} \partial_r (r \cdot) \\ -\partial_r & \frac{1}{\mu} \end{pmatrix}. \quad (4.50)$$

The vector equation (4.48) and the expressions (4.49) and (4.50) hold true for cylindrical geometries in general. The eigenvalue problem corresponding to (4.48) takes the same form as in (3.14).

For the remaining steps in the adaptation of the multimodal method to axially symmetric longitudinal modes in cylindrical waveguides, it is necessary to view cylindrical rods and hollow cylinders as two distinct cases.

4.2.1 Cylindrical rods

The geometry of a cylindrical rod with varying thickness is illustrated in Figure 4.1. The central axis is marked by a dash-dotted line with z denoting the direction of wave propagation.

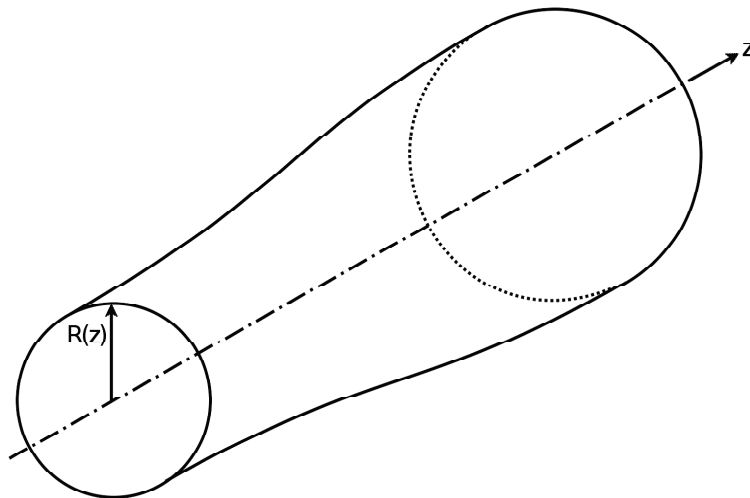


Figure 4.1: Cylindrical rod with varying thickness.

The guided wave modes of cylindrical rods with constant thickness that have been described in Chapter 2 are used as basis for the modal expansion in cylindrical rods with varying thickness. Similar to the case of plates with varying thickness as described in Chapter 3, the actual basis functions have to be derived from modified versions of the Helmholtz potentials given in (2.40)-(2.43) which do not vanish at $\beta = 0$. The relevant Helmholtz potentials are

$$\Phi = AJ_0(\alpha r)e^{ikz} \quad (4.51)$$

and

$$H_\varphi = B \frac{J_1(\beta r)}{\beta} e^{ikz}. \quad (4.52)$$

Once again the time dependence $e^{i\omega t}$ has been omitted.

For cylindrical rods the eigenvectors \vec{X}_n and \vec{Y}_n still fulfill a biorthogonality relation of the form given in (3.19), where the scalar product now corresponds to an integration $\int_0^{2\pi} \int_0^R r dr d\varphi$, and have to be normalized in a way to ensure that they remain a valid orthogonal basis for $k_n = 0$. As in Chapter 3, the diagonal entries $Z_{c,n}$ of the characteristic impedance matrix \mathbf{Z}_c are introduced as renormalization factors and the eigenvalue problem (3.14) is modified into (3.20).

The eigenvectors \vec{X}_n and \vec{Y}_n which form the orthogonal basis for axially symmetric lon-

itudinal guided waves in cylindrical rods take the form

$$\vec{X}_n = (k_n^2 - \beta_n^2) Z_{c,n} i k_n \begin{pmatrix} J_0(\alpha_n r) \\ -2\mu \alpha_n J_1(\alpha_n r) \end{pmatrix} + \begin{pmatrix} J_0(\beta_n r) \\ (k_n^2 - \beta_n^2) \frac{\mu}{\beta_n} J_1(\beta_n r) \end{pmatrix} \quad (4.53)$$

$$\vec{Y}_n = (k_n^2 - \beta_n^2) \begin{pmatrix} \mu(k_n^2 - 2\alpha_n^2 + \beta_n^2) J_0(\alpha_n r) \\ -\alpha_n J_1(\alpha_n r) \end{pmatrix} - \frac{i k_n}{Z_{c,n}} \begin{pmatrix} 2\mu J_0(\beta_n r) \\ \frac{1}{\beta_n} J_1(\beta_n r) \end{pmatrix} \quad (4.54)$$

with

$$Z_{c,n} = \frac{J_1(\beta_n R)}{2i k_n \alpha_n \beta_n J_1(\alpha_n R)} = \frac{2i k_n (\beta_n R J_0(\beta_n R) - J_1(\beta_n R))}{(k_n^2 - \beta_n^2)^2 \beta_n R J_0(\alpha_n R) + 2\alpha_n \beta_n (k_n^2 - \beta_n^2) J_1(\alpha_n R)} \quad (4.55)$$

where R denotes the outer radius of the cylindrical rod.

The modal expansion is done in accordance with (3.27) and (3.28). In order to derive the differential equations that describe the evolution of \vec{a} and \vec{b} in z -direction, the system (4.48) is projected onto the bases \vec{X}_n and $Z_{c,n} \vec{Y}_n$ by

$$\langle \partial_z \vec{X} \mid Z_{c,n} \vec{Y}_n \rangle = \langle \mathbf{F} \vec{Y} \mid Z_{c,n} \vec{Y}_n \rangle \quad (4.56)$$

and

$$\langle \partial_z \vec{Y} \mid \vec{X}_n \rangle = \langle \mathbf{G} \vec{X} \mid \vec{X}_n \rangle \quad (4.57)$$

which leads to the coupled differential equations

$$\partial_z \vec{a} = \mathbf{N}_1 \vec{a} + \mathbf{N}_2 \vec{b} \quad (4.58)$$

and

$$\partial_z \vec{b} = \mathbf{N}_3 \vec{a} + \mathbf{N}_4 \vec{b} \quad (4.59)$$

where the matrices \mathbf{N}_1 , \mathbf{N}_2 , \mathbf{N}_3 and \mathbf{N}_4 are given by

$$N_{1,nm} = -\frac{1}{\mathcal{J}_n} \langle \partial_z \vec{X}_m \mid \vec{Y}_n \rangle \quad (4.60)$$

$$N_{2,nm} = \frac{i k_n}{Z_{c,n}} \delta_{nm} \quad (4.61)$$

$$N_{3,nm} = i k_n Z_{c,n} \delta_{nm} \quad (4.62)$$

$$N_{4,nm} = \frac{1}{\mathcal{J}_n} \left\{ -\langle \partial_z \vec{Y}_m \mid \vec{X}_n \rangle + (\partial_z R) R \sigma_{zz,m}(R) u_{z,n}(R) \right\}. \quad (4.63)$$

The expressions (4.60) and (4.63) are evaluated by using the properties of the operators \mathbf{F} and \mathbf{G} . The procedure is similar to the one used to derive the corresponding expressions for plates and can be found in some detail in Appendix B. Using the notations $u_{z,n}(R) =$

\mathcal{U}_n , $u_{r,n}(R) = \mathcal{V}_n$, $\sigma_{zz,n}(R) = \mathcal{S}_n$ and $\partial_z f = f'$, the resulting expressions for elements of \mathbf{N}_1 and \mathbf{N}_4 are

$$N_{1,nn} = \frac{-1}{2\mathcal{I}_n} \left\{ \mathcal{I}'_n + \mathcal{I}_n \frac{Z'_{c,n}}{Z_{c,n}} + \pi RR' \left[\mathcal{U}_n \mathcal{S}_n + i\rho\omega^2 \left(\frac{\mathcal{U}_n^2}{k_n Z_{c,n}} + \frac{Z_{c,n} \mathcal{V}_n^2}{k_n} \right) \right] \right. \\ \left. - \frac{i\pi}{k_n} Z_{c,n} R' \frac{1}{2(\lambda + \mu)} \left(\lambda \mathcal{S}_n \mathcal{V}_n + \frac{2\mu}{R} (3\lambda + 2\mu) \mathcal{V}_n^2 \right) \right\} \quad (4.64)$$

$$N_{4,nn} = \frac{1}{2\mathcal{I}_n} \left\{ -\mathcal{I}'_n + \mathcal{I}_n \frac{Z'_{c,n}}{Z_{c,n}} + \pi RR' \left[\mathcal{U}_n \mathcal{S}_n + i\rho\omega^2 \left(\frac{\mathcal{U}_n^2}{k_n Z_{c,n}} + \frac{Z_{c,n} \mathcal{V}_n^2}{k_n} \right) \right] \right. \\ \left. - \frac{i\pi}{k_n} Z_{c,n} R' \frac{1}{2(\lambda + \mu)} \left(\lambda \mathcal{S}_n \mathcal{V}_n + \frac{2\mu}{R} (3\lambda + 2\mu) \mathcal{V}_n^2 \right) \right\} \quad (4.65)$$

for $n = m$ and

$$N_{1,mm} = \frac{2\pi RR'}{\mathcal{I}_n(k_m^2 - k_n^2)} \left\{ i\rho\omega^2 \left(\frac{k_n \mathcal{U}_n \mathcal{U}_m}{Z_{c,n}} - k_m Z_{c,m} \mathcal{V}_n \mathcal{V}_m \right) \right. \\ \left. - \frac{k_m}{2Z_{c,n}} (k_m \mathcal{U}_m Z_{c,n} \mathcal{S}_n + Z_{c,m} \mathcal{S}_m k_n \mathcal{U}_n) \right. \\ \left. + \frac{ik_m Z_{c,m}}{4R(\lambda + \mu)} \left[\lambda (\mathcal{S}_m \mathcal{V}_n + \mathcal{S}_n \mathcal{V}_m) + \frac{4\mu}{R} (3\lambda + 2\mu) \mathcal{V}_m \mathcal{V}_n \right] \right\} \quad (4.66)$$

$$N_{4,mm} = \frac{2\pi RR'}{\mathcal{I}_n(k_m^2 - k_n^2)} \left\{ i\rho\omega^2 \left(\frac{k_m \mathcal{U}_n \mathcal{U}_m}{Z_{c,m}} - k_n Z_{c,n} \mathcal{V}_n \mathcal{V}_m \right) \right. \\ \left. - \frac{k_n}{2Z_{c,m}} (k_n \mathcal{U}_n Z_{c,m} \mathcal{S}_m + Z_{c,n} \mathcal{S}_n k_m \mathcal{U}_m) \right. \\ \left. + \frac{ik_n Z_{c,n}}{4R(\lambda + \mu)} \left[\lambda (\mathcal{S}_n \mathcal{V}_m + \mathcal{S}_m \mathcal{V}_n) + \frac{4\mu}{R} (3\lambda + 2\mu) \mathcal{V}_m \mathcal{V}_n \right] \right\} \quad (4.67)$$

for $n \neq m$. An expression for \mathcal{I}_n is found by directly evaluating the scalar product in (3.19) using the expressions (4.53) and (4.54) for \vec{X}_n and \vec{Y}_m . All ensuing integrals with Bessel functions have closed analytical solutions [73] and ultimately lead to

$$\mathcal{I}_n = 2\pi\mu \frac{ik_n}{Z_{c,n}\beta_n^2} (k_n^2 + \beta_n^2) \left\{ -\frac{(k_n^2 + \beta_n^2)}{2k_n^2(k_n^2 - \beta_n^2)^2} (5k_n^2 - 3\beta_n^2) J_1^2(\beta_n R) \right. \\ \left. - \frac{R^2}{2} \left[\left(1 + \frac{4k_n^2\beta_n^2}{(k_n^2 - \beta_n^2)^2} \right) J_0^2(\beta_n R) + \left(1 + \frac{(k_n^2 - \beta_n^2)^2}{4k_n^2\alpha_n^2} \right) J_1^2(\beta_n R) \right] \right. \\ \left. + \frac{(k_n^2 + \beta_n^2)}{k_n^2\beta_n^2(k_n^2 - \beta_n^2)^2} \beta_n R [k_n^2(k_n^2 + \beta_n^2) + \beta_n^2(k_n^2 - \beta_n^2)] J_0(\beta_n R) J_1(\beta_n R) \right\}. \quad (4.68)$$

4.2.2 Hollow cylinders

The geometry of a hollow cylinder with varying thickness is illustrated in Figure 4.2. The central axis is marked by a dash-dotted line with z denoting the direction of wave propagation. In accordance with the geometry of a wheelset-axle, the variation in thickness arises from the fact that the outer radius R_O varies in z -direction while the inner radius R_I is constant.

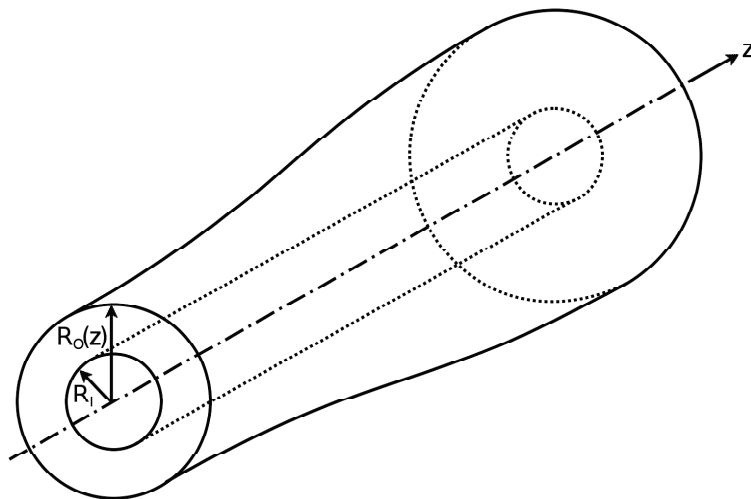


Figure 4.2: Hollow cylinder with varying thickness.

The guided wave modes of hollow cylinders with constant thickness that have been described in Chapter 2 serve as basis for the modal expansion in hollow cylinders with varying thickness. In order to simplify the expressions used throughout further calculations and to keep them more in line with the expressions derived for the case of cylindrical rods, we combine Bessel functions of first and second kind by introducing the functions

$$\hat{H}_0(\alpha r) = J_0(\alpha r) + Q_1 Y_0(\alpha r) \quad (4.69)$$

$$\hat{H}_1(\alpha r) = J_1(\alpha r) + Q_1 Y_1(\alpha r) \quad (4.70)$$

$$\tilde{H}_0(\beta r) = J_0(\beta r) + Q_2 Y_0(\beta r) \quad (4.71)$$

$$\tilde{H}_1(\beta r) = J_1(\beta r) + Q_2 Y_1(\beta r) \quad (4.72)$$

where $Q_1 = C/A$ and $Q_2 = D/B$ are formed from the coefficients used e.g. in (2.54) and (2.55). The analytical expressions for Q_1 and Q_2 have to be derived from the boundary conditions of traction free lateral surfaces at the inner radius $r = R_I$ and the outer radius $r = R_O$. While the detailed calculation will be omitted in this work valid expressions for both terms are provided in Appendix C.

If the same modifications that have been used on (2.40)-(2.43) for the case of cylindrical rods are applied to the Helmholtz potentials given in (2.54) and (2.55) and (4.69)-(4.72)

are used, the modified versions of the relevant Helmholtz potentials for hollow cylinders take the form

$$\Phi = A\hat{H}_0(\alpha r)e^{ikz} \quad (4.73)$$

and

$$H_\varphi = B\frac{\tilde{H}_1(\beta r)}{\beta}e^{ikz} \quad (4.74)$$

with the time dependence $e^{i\omega t}$ being omitted as before.

In case of a hollow cylinder, the biorthogonality relation given in (3.19) remains valid for the eigenvectors \vec{X}_n and \vec{Y}_n . The scalar product now corresponds to an integration $\int_0^{2\pi} \int_{R_I}^{R_O} r dr d\varphi$. Since plates and cylindrical rods can be considered as asymptotic cases of hollow cylinders, the characteristic impedance matrix \mathbf{Z}_c for hollow cylinders is constructed in a similar manner as for those previously described cases. If its diagonal elements $Z_{c,n}$ are used to renormalize the eigenvectors \vec{X}_n and \vec{Y}_n and to modify the eigenvalue problem (3.14) into the form (3.20), the orthogonal basis for axially symmetric longitudinal guided waves in hollow cylinders takes the form

$$\vec{X}_n = (k_n^2 - \beta_n^2)Z_{c,n}ik_n \begin{pmatrix} \hat{H}_0(\alpha_n r) \\ -2\mu\alpha_n\hat{H}_1(\alpha_n r) \end{pmatrix} + \begin{pmatrix} \tilde{H}_0(\beta_n r) \\ (k_n^2 - \beta_n^2)\frac{\mu}{\beta_n}\tilde{H}_1(\beta_n r) \end{pmatrix} \quad (4.75)$$

$$\vec{Y}_n = (k_n^2 - \beta_n^2) \begin{pmatrix} \mu(k_n^2 - 2\alpha_n^2 + \beta_n^2)\hat{H}_0(\alpha_n r) \\ -\alpha_n\hat{H}_1(\alpha_n r) - \frac{ik_n}{Z_{c,n}} \begin{pmatrix} 2\mu\tilde{H}_0(\beta_n r) \\ \frac{1}{\beta_n}\tilde{H}_1(\beta_n r) \end{pmatrix} \end{pmatrix} \quad (4.76)$$

with

$$\begin{aligned} Z_{c,n} &= \frac{\tilde{H}_1(\beta_n R_O)}{2ik_n\alpha_n\beta_n\hat{H}_1(\alpha_n R_O)} = \frac{2ik_n(\beta_n R_O\tilde{H}_0(\beta_n R_O) - \tilde{H}_1(\beta_n R_O))}{(k_n^2 - \beta_n^2)^2\beta_n R_O\hat{H}_0(\alpha_n R_O) + 2\alpha_n\beta_n(k_n^2 - \beta_n^2)\hat{H}_1(\alpha_n R_O)} \\ &= \frac{\tilde{H}_1(\beta_n R_I)}{2ik_n\alpha_n\beta_n\hat{H}_1(\alpha_n R_I)} = \frac{2ik_n(\beta_n R_I\tilde{H}_0(\beta_n R_I) - \tilde{H}_1(\beta_n R_I))}{(k_n^2 - \beta_n^2)^2\beta_n R_I\hat{H}_0(\alpha_n R_I) + 2\alpha_n\beta_n(k_n^2 - \beta_n^2)\hat{H}_1(\alpha_n R_I)}. \end{aligned} \quad (4.77)$$

As before in the adaptation to the case of cylindrical rods, the modal expansion is done in accordance with (3.27) and (3.28) while the system (4.48) is projected onto the bases \vec{X}_n and $Z_{c,n}\vec{Y}_n$ as described by (4.56) and (4.57). The resulting system of coupled differential equations that describe the evolution of \vec{a} and \vec{b} in z -direction then takes the same form as in (4.58) and (4.59) with \mathbf{N}_1 , \mathbf{N}_2 , \mathbf{N}_3 and \mathbf{N}_4 being described by

$$N_{1,nm} = -\frac{1}{\mathcal{J}_n} \left\langle \partial_z \vec{X}_m \middle| \vec{Y}_n \right\rangle \quad (4.78)$$

$$N_{2,nm} = \frac{ik_n}{Z_{c,n}} \delta_{nm} \quad (4.79)$$

$$N_{3,nm} = ik_n Z_{c,n} \delta_{nm} \quad (4.80)$$

$$N_{4,nm} = \frac{1}{\mathcal{I}_n} \left\{ (\partial_z R_O) R_O \sigma_{zz,m}(R_O) u_{z,n}(R_O) - (\partial_z R_I) R_I \sigma_{zz,m}(R_I) u_{z,n}(R_I) - \left\langle \partial_z \vec{Y}_m \middle| \vec{X}_n \right\rangle \right\} \quad (4.81)$$

for the case of hollow cylinders. In order to implement the multimodal method for hollow cylinders, the expressions (4.78) and (4.81) have to be evaluated by using the properties of the operators \mathbf{F} and \mathbf{G} . The procedure closely resembles the one used for cylindrical rods. The most important steps are illustrated in Appendix B.

Given the desired future application on wheelset-axles, we can assume the inner radius R_I to be constant and thus $\partial_z R_I = 0$ which simplifies the expressions for \mathbf{N}_1 and \mathbf{N}_4 to some degree. With the notations $u_{z,n}(R_O) = \mathcal{U}_n$, $u_{r,n}(R_O) = \mathcal{V}_n$, $\sigma_{zz,n}(R_O) = \mathcal{S}_n$ and $\partial_z f = f'$, the elements of \mathbf{N}_1 and \mathbf{N}_4 (for the special case of constant inner radius R_I) can be expressed as

$$N_{1,nn} = \frac{-1}{2\mathcal{I}_n} \left\{ \mathcal{I}'_n + \mathcal{I}_n \frac{Z'_{c,n}}{Z_{c,n}} + \pi R_O R'_O \left[\mathcal{U}_n \mathcal{S}_n + i\rho\omega^2 \left(\frac{\mathcal{U}_n^2}{k_n Z_{c,n}} + \frac{Z_{c,n} \mathcal{V}_n^2}{k_n} \right) \right] - \frac{i\pi}{k_n} Z_{c,n} R'_O \frac{1}{2(\lambda + \mu)} \left(\lambda \mathcal{S}_n \mathcal{V}_n + \frac{2\mu}{R_O} (3\lambda + 2\mu) \mathcal{V}_n^2 \right) \right\} \quad (4.82)$$

$$N_{4,nn} = \frac{1}{2\mathcal{I}_n} \left\{ -\mathcal{I}'_n + \mathcal{I}_n \frac{Z'_{c,n}}{Z_{c,n}} + \pi R_O R'_O \left[\mathcal{U}_n \mathcal{S}_n + i\rho\omega^2 \left(\frac{\mathcal{U}_n^2}{k_n Z_{c,n}} + \frac{Z_{c,n} \mathcal{V}_n^2}{k_n} \right) \right] - \frac{i\pi}{k_n} Z_{c,n} R'_O \frac{1}{2(\lambda + \mu)} \left(\lambda \mathcal{S}_n \mathcal{V}_n + \frac{2\mu}{R_O} (3\lambda + 2\mu) \mathcal{V}_n^2 \right) \right\} \quad (4.83)$$

for $n = m$ and

$$N_{1,nm} = \frac{2\pi R_O R'_O}{\mathcal{I}_n (k_m^2 - k_n^2)} \left\{ i\rho\omega^2 \left(\frac{k_n \mathcal{U}_n \mathcal{U}_m}{Z_{c,n}} - k_m Z_{c,m} \mathcal{V}_n \mathcal{V}_m \right) - \frac{k_m}{2Z_{c,n}} (k_m \mathcal{U}_m Z_{c,n} \mathcal{S}_n + Z_{c,m} \mathcal{S}_m k_n \mathcal{U}_n) + \frac{ik_m Z_{c,m}}{4R_O (\lambda + \mu)} \left[\lambda (\mathcal{S}_m \mathcal{V}_n + \mathcal{S}_n \mathcal{V}_m) + \frac{4\mu}{R_O} (3\lambda + 2\mu) \mathcal{V}_m \mathcal{V}_n \right] \right\} \quad (4.84)$$

$$N_{4,nm} = \frac{2\pi R_O R'_O}{\mathcal{I}_n (k_m^2 - k_n^2)} \left\{ i\rho\omega^2 \left(\frac{k_m \mathcal{U}_n \mathcal{U}_m}{Z_{c,m}} - k_n Z_{c,n} \mathcal{V}_n \mathcal{V}_m \right) - \frac{k_n}{2Z_{c,m}} (k_n \mathcal{U}_n Z_{c,m} \mathcal{S}_m + Z_{c,n} \mathcal{S}_n k_m \mathcal{U}_m) + \frac{ik_n Z_{c,n}}{4R_O (\lambda + \mu)} \left[\lambda (\mathcal{S}_n \mathcal{V}_m + \mathcal{S}_m \mathcal{V}_n) + \frac{4\mu}{R_O} (3\lambda + 2\mu) \mathcal{V}_m \mathcal{V}_n \right] \right\} \quad (4.85)$$

for $n \neq m$. In order to find \mathcal{I}_n , the scalar product in (3.19) has to be directly evaluated for the expressions of \vec{X}_n and \vec{Y}_m that are given in (4.75) and (4.76). Even though we now have to consider Bessel functions of first and second kind, the ensuing integrals still yield closed analytical solutions [73]. Ultimately we find that for hollow cylinders, \mathcal{I}_n takes the form

$$\begin{aligned}
\mathcal{I}_n = & 2\pi\mu \frac{ik_n}{Z_{c,n}\beta_n^2} (k_n^2 + \beta_n^2) \left\{ -\frac{(k_n^2 + \beta_n^2)}{2k_n^2(k_n^2 - \beta_n^2)^2} (5k_n^2 - 3\beta_n^2) \left(\tilde{H}_1^2(\beta_n R_O) - \tilde{H}_1^2(\beta_n R_I) \right) \right. \\
& + \frac{(k_n^2 + \beta_n^2)}{k_n^2\beta_n^2(k_n^2 - \beta_n^2)^2} \beta_n \left[k_n^2(k_n^2 + \beta_n^2) + \beta_n^2(k_n^2 - \beta_n^2) \right] R_O \tilde{H}_0(\beta_n R_O) \tilde{H}_1(\beta_n R_O) \\
& - \frac{(k_n^2 + \beta_n^2)}{k_n^2\beta_n^2(k_n^2 - \beta_n^2)^2} \beta_n \left[k_n^2(k_n^2 + \beta_n^2) + \beta_n^2(k_n^2 - \beta_n^2) \right] R_I \tilde{H}_0(\beta_n R_I) \tilde{H}_1(\beta_n R_I) \\
& - \frac{1}{2} \left(1 + \frac{4k_n^2\beta_n^2}{(k_n^2 - \beta_n^2)^2} \right) \left(R_O^2 \tilde{H}_0^2(\beta_n R_O) - R_I^2 \tilde{H}_0^2(\beta_n R_I) \right) \\
& \left. - \frac{1}{2} \left(1 + \frac{(k_n^2 - \beta_n^2)^2}{4k_n^2\alpha_n^2} \right) \left(R_O^2 \tilde{H}_1^2(\beta_n R_O) - R_I^2 \tilde{H}_1^2(\beta_n R_I) \right) \right\}.
\end{aligned} \tag{4.86}$$

Chapter 5

Simulation results

5.1 Plates

In order to validate the implementation of the multimodal method for plates as described in Chapter 3, a set of test cases for plates with varying thickness has been investigated. For each test case, the displacement field in x -direction was simulated using the multimodal method as well as FEM for comparison. The simulations with the multimodal method have been carried out using MATLAB R2007b (Ver. 7.5.0.342) with the initial excitation limited to the A_0 -mode and $N = 17$ as total number of simulated modes. For the FEM simulations, COMSOL 4.0a (Ver. 4.0.0.982) was used for the first test case of plates with symmetrically varying thickness and the test case of plates with asymmetrically varying thickness and ANSYS 16.0 (Ver. 16.0.0.78) for all remaining test cases. A mode selective excitation in favour of the A_0 -mode was used in all FEM simulations for plates.

The waveguide was modelled as in the test cases used by Pagneux and Maurel, the material parameters given in [17] have been repeated in Chapter 3 and translate into the density $\rho=1 \text{ mg/mm}^3$ and the Lamé constants $\lambda = 2.48/(0.38\pi^2) \text{ GPa}$ and $\mu = 4/\pi^2 \text{ GPa}$ which have been used in the implementation discussed in this thesis.

The smallest wavelengths contributing to the simulations can be expected to be approximately 1 mm. Therefore, the discretization step size in the direction of wave propagation was set to $\Delta x = 0.1 \text{ mm}$ for the multimodal method. In the FEM simulations carried out with COMSOL, a mesh with triangular elements ranging from 0.01 mm to 0.5 mm in size has been used while the simulations carried out in ANSYS used a mesh with rectangular elements at a fixed size of 0.1 mm. The resolution in time dependence of the sound fields in the FEM simulations was set to $\Delta t = 10^{-8} \text{ s}$.

5.1.1 Plates with symmetrically varying thickness

The examples used by Pagneux and Maurel in [17] are chosen as test cases for plates with symmetrically varying thickness. While it has been shown in Chapter 3 that the

implementation of the multimodal method used in this work reproduces the results published in [17], these results have not been validated against a source independent from the multimodal method. The geometry of the plate with symmetrically varying thickness is described as in (3.67) by

$$h_U(x) = h_0 + (h_1 - h_0)e^{-\frac{x^2}{L^2}} \quad (5.1)$$

and

$$h_L(x) = -h_0 - (h_1 - h_0)e^{-\frac{x^2}{L^2}} \quad (5.2)$$

with $h_0 = 0.7$ mm, $h_1 = 1.5$ mm and $L = 1.5$ mm.

Figure 5.2 a) shows the simulation result obtained via multimodal method for the displacement field in x -direction for an excitation of the A_0 -mode at $\omega = 0.5$ MHz ($f \approx 0.08$ MHz) which corresponds to the test case documented in [17]: Figure 4a. For the FEM simulations performed with COMSOL, the geometry of the waveguide was extended to the left and to the right. For the mode selective excitation, a continuous wave excitation has been applied in a way that the wavelength corresponding to the desired guided wave mode at the given frequency was forced onto a limited region of the waveguide's surface. After running the simulation long enough for the front of the resulting guided wave to propagate through the area of interest, an appropriate frame has been chosen for comparison with the results obtained via multimodal method. The result of the FEM simulation is shown in Figure 5.2 b). The corresponding dispersion curves for real valued wave numbers are plotted in Figure 5.1. The results for this first test case in plates with symmetrically varying thickness as shown in Figure 5.2 have already been published and discussed in [74] but are included in this thesis as well to supplement the two more complex examples.

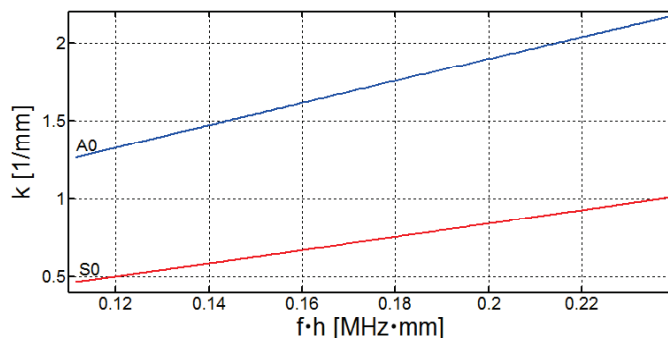


Figure 5.1: Dispersion curves for real valued wave numbers corresponding to a plate with symmetrically varying thickness for an excitation frequency of $\omega = 0.5$ MHz.

Figure 5.1 shows that the A_0 -mode is the only propagating A -mode throughout the entire waveguide in the simulation results shown in Figure 5.2. The largest wave number in Figure 5.1 is $k = 2.167$ 1/mm which corresponds to a minimum wavelength of approximately 2.90 mm.

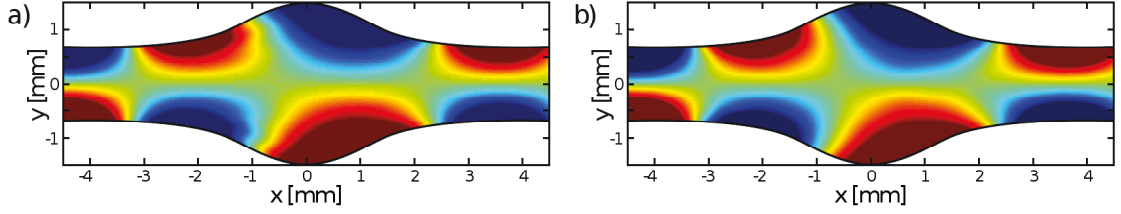


Figure 5.2: Displacement field in x -direction in a plate with symmetrically varying thickness for an excitation frequency of $\omega = 0.5$ MHz simulated with a) multimodal method and b) COMSOL with red for positive and blue for negative displacement.

As we can see, the results for the FEM simulations and the multimodal method are in good agreement, however, on close examination some fine structures can be found in the displacement field shown in Figure 5.2 a) which are in agreement with the plot shown in [17]: Figure 4a but are missing in Figure 5.2 b). While these deviations have been noted in [74], the explanation for their presence can be found in [24] and boils down to a slow convergence with increasing number of evanescent modes. In fact it has been confirmed in the course of this work that these fine structures diminish if simulations are run with a higher total number of simulated modes N .

Figure 5.4 a) shows the simulation result obtained via multimodal method for the displacement field in x -direction for an excitation of the A_0 -mode at $\omega = 1.37$ MHz ($f \approx 0.22$ MHz) which corresponds to the test case documented in [17]: Figure 4b. For comparison, an FEM simulation has been performed with ANSYS in a similar way as described for the previous test case, the result of which is shown in Figure 5.4 b). The dispersion curves for real valued wave numbers are plotted in Figure 5.3.

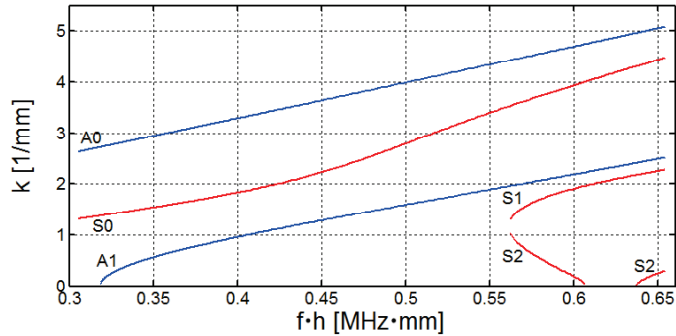


Figure 5.3: Dispersion curves for real valued wave numbers corresponding to a plate with symmetrically varying thickness for an excitation frequency of $\omega = 1.37$ MHz.

As can be seen in Figure 5.3, the displacement field shown in Figure 5.4 is composed of the A_0 -mode which is propagating throughout the entire waveguide and the A_1 -mode which is evanescent at the ends of the waveguide but can propagate near the center. The

largest wave number to be found in Figure 5.3 is $k = 5.085$ 1/mm which corresponds to a minimum wavelength of about 1.24 mm.

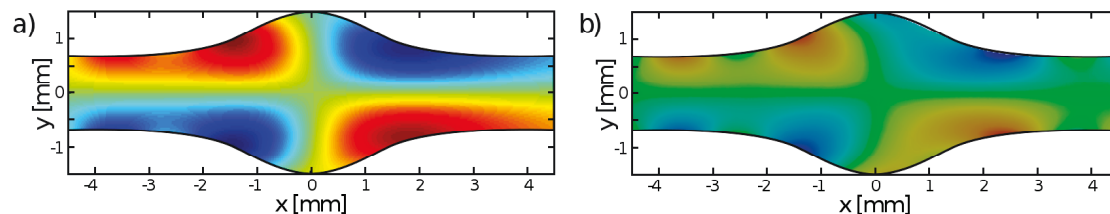


Figure 5.4: Displacement field in x -direction in a plate with symmetrically varying thickness for an excitation frequency of $\omega = 1.37$ MHz simulated with a) multimodal method and b) ANSYS with red for positive and blue for negative displacement.

The resulting trapped mode pattern¹ is clearly visible in the plots obtained with the multimodal method (Figure 5.4 a)) and the FEM simulation (Figure 5.4 b)). Thus the results of both methods can be considered to be in good agreement.

Figure 5.6 a) shows the simulation result obtained via multimodal method for the displacement field in x -direction for an excitation of the A_0 -mode at $\omega = 1.5$ MHz ($f \approx 0.24$ MHz) which corresponds to the test case documented in [17]: Figure 4c. The result of the corresponding FEM simulation, which has been performed with ANSYS for comparison is shown in Figure 5.6 b). The corresponding real valued wave numbers are shown in Figure 5.5.

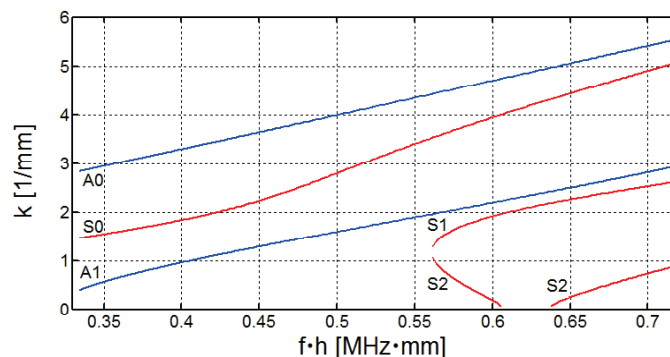


Figure 5.5: Dispersion curves for real valued wave numbers corresponding to a plate with symmetrically varying thickness for an excitation frequency of $\omega = 1.5$ MHz.

In this test case, the A_0 and the A_1 -mode are contributing to the displacement field as illustrated in Figure 5.5 with the largest wave number being $k = 5.528$ 1/mm and thus the minimum wavelength being approximately 1.14 mm.

¹See [17] for a more extensive description.

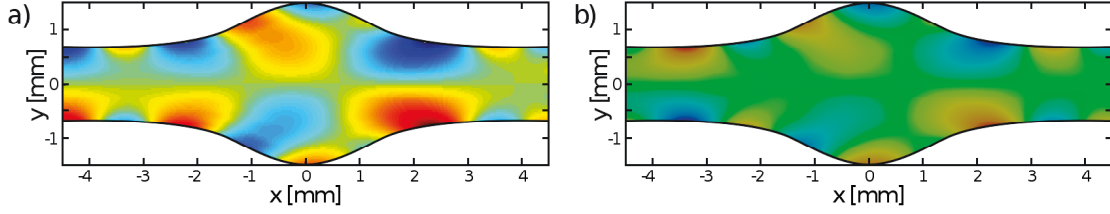


Figure 5.6: Displacement field in x -direction in a plate with symmetrically varying thickness for an excitation frequency of $\omega = 1.5$ MHz simulated with a) multimodal method and b) ANSYS with red for positive and blue for negative displacement.

Both modes are propagating throughout the entire waveguide and are coupled to each other due to the variation of thickness. The patterns of the displacement field in x -direction obtained with the multimodal method (Figure 5.6 a)) and the FEM simulation (Figure 5.6 b)) are very similar. Small deviations might arise from an insufficient number of evanescent modes in the multimodal approach. Another source of error might be the fact that, while in the multimodal method the excitation is truly limited to the A_0 -mode, the mode selective excitation in FEM simulations has to be accomplished by modelling the excitation pattern to match the desired mode and might not yield perfect results. By and large the displacement field obtained with the multimodal method matches the one found by using the commercially available FEM software.

5.1.2 Plates with asymmetrically varying thickness

While the extension of the multimodal method to plates with asymmetrically varying thickness in itself is not essential for the subsequent adaptation to cylindrical geometries, it does provide some insight into the effect of breaches in the waveguide's symmetry and how to handle coupling between different families of modes. Therefore, it seems worthwhile to briefly validate the implementation for such plates as well. For this purpose, the first test case for plates with symmetrically varying thickness has been modified. The geometry of the plate with asymmetrically varying thickness is described by

$$h_U(x) = h_0 + (h_1 - h_0)e^{-\frac{x^2}{L^2}} \quad (5.3)$$

and

$$h_L(x) = -h_0 \quad (5.4)$$

with $h_0 = 0.7$ mm, $h_1 = 1.5$ mm and $L = 1.5$ mm.

The simulation result for the displacement field in x -direction for an excitation of the A_0 -mode at a frequency of $\omega = 0.5$ MHz ($f \approx 0.08$ MHz), obtained with the multimodal method, is plotted in Figure 5.8 a). The FEM simulation used for comparison has been performed in the same manner as described for the first test case in a plate with symmetrically varying thickness by using COMSOL. The result can be found in Figure 5.8 b). The plot of the corresponding real valued wave numbers is presented in Figure

5.7. While the results shown in Figure 5.8 have been previously published in [74], we will discuss them once more in this thesis.

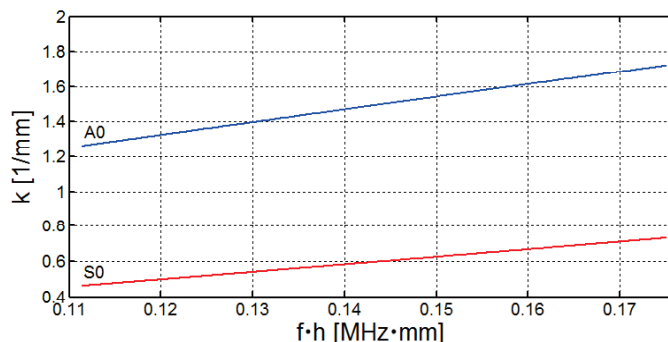


Figure 5.7: Dispersion curves for real valued wave numbers corresponding to a plate with asymmetrically varying thickness for an excitation frequency of $\omega = 0.5$ MHz.

In this test case, both the A_0 and the S_0 -mode are propagating modes throughout the entire waveguide (see Figure 5.7) and even though only the A_0 -mode is excited initially, both modes will be coupled to each other due to the asymmetric properties of the plate. Therefore, the displacement field contains contributions of both the A_0 and the S_0 -mode. The largest wave number in Figure 5.7 is $k = 1.721$ 1/mm which corresponds to a minimum wavelength of about 3.65 mm.

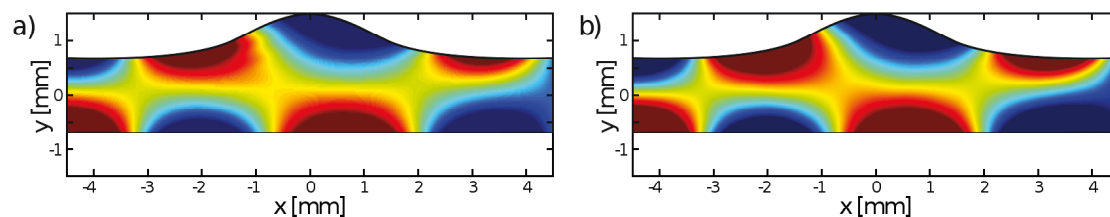


Figure 5.8: Displacement field in x -direction in a plate with asymmetrically varying thickness for an excitation frequency of $\omega = 0.5$ MHz simulated with a) multimodal method and b) COMSOL with red for positive and blue for negative displacement.

As can be seen, the displacement field calculated with the multimodal method (Figure 5.8 a)) is in good agreement with the one obtained from the FEM simulation (Figure 5.8 b)) even though the plot in Figure 5.8 a) shows some fine structures similar to those observed in the first test case for a plate with symmetrically varying thickness which are not reproduced by the FEM simulation.

5.2 Cylindrical rods

To test the adaptation of the multimodal method to cylindrical rods as described in Chapter 4, displacement fields in r -direction have been calculated in a cylindrical rod of

varying thickness for different frequencies using the multimodal method and subsequently compared to the results of corresponding FEM simulations. The simulations with the multimodal method have been carried out using MATLAB R2007b (Ver. 7.5.0.342) with the initial excitation limited to the axisymmetric $L(0,0)$ -mode. Compared to the simulations carried out in plates, the total number of simulated modes was increased to $N = 25$. The FEM simulations were carried out with ANSYS 16.0 (Ver. 16.0.0.78) with a mode selective excitation in favour of the $L(0,0)$ -mode.

The waveguide was modelled in a similar way as for the simulations in plates. The material is still described by the density $\rho = 1 \text{ mg/mm}^3$ and the Lamé constants $\lambda = 2.48/(0.38\pi^2) \text{ GPa}$ and $\mu = 4/\pi^2 \text{ GPa}$ while the geometry is defined by

$$R = R_0 + (R_1 - R_0)e^{-\frac{z^2}{L^2}} \quad (5.5)$$

with $R_0 = 1 \text{ mm}$, $R_1 = 1.5 \text{ mm}$ and $L = 1.5 \text{ mm}$.

With the smallest expected wavelengths contributing to the simulations being expected around 1 mm, the discretization step size in the direction of wave propagation was set to $\Delta z = 0.1 \text{ mm}$ for the multimodal method while the FEM simulations carried out in ANSYS used a mesh with rectangular elements at a fixed size of 0.1 mm. The resolution in time dependence of the sound fields in the FEM simulations was set to $\Delta t = 10^{-8} \text{ s}$.

The displacement field in r -direction for an excitation of the $L(0,0)$ -mode at $\omega = 1.25 \text{ MHz}$ ($f \approx 0.20 \text{ MHz}$) as obtained with the multimodal method is shown in Figure 5.10 a). In a similar procedure as used for the FEM simulations in plates, the rod was extended to the left and to the right in order to apply a mode selective excitation and allow the front of the resulting guided waves to propagate through the region of interest. The result has been plotted in Figure 5.10 b). Figure 5.9 shows the corresponding dispersion curves of real valued wave numbers. The results for this first test case can also be found in [75] but are included in this thesis as part of a more extensive validation of the implementation for cylindrical rods.

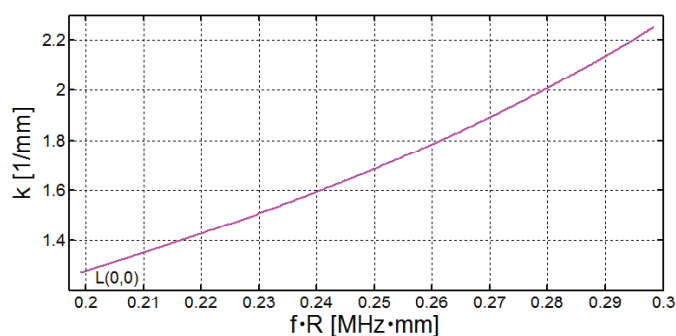


Figure 5.9: Dispersion curves for real valued wave numbers corresponding to a cylindrical rod with varying thickness for an excitation frequency of $\omega = 1.25 \text{ MHz}$.

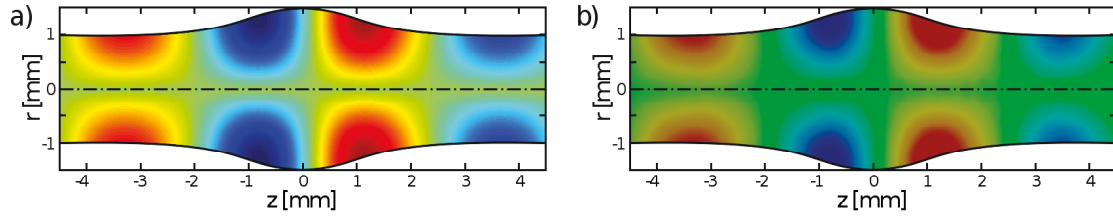


Figure 5.10: Displacement field in r -direction in a cylindrical rod with varying thickness for an excitation frequency of $\omega = 1.25$ MHz simulated with a) multimodal method and b) ANSYS with red for positive and blue for negative displacement.

As can be seen in Figure 5.9, the $L(0,0)$ -mode is the only propagating mode throughout the entire waveguide in simulation results shown in Figure 5.10 with the largest wave number being $k = 2.254$ 1/mm and thus a resulting smallest wavelength of approximately 2.79 mm. The simulation using the multimodal method (Figure 5.10 a)) and the commercially available FEM software ANSYS (Figure 5.10 b)) both lead to identical results for the investigated displacement field.

Figure 5.12 a) shows the simulation result obtained via multimodal method for the displacement field in r -direction for an excitation of the $L(0,0)$ -mode at $\omega = 2.5$ MHz ($f \approx 0.40$ MHz). For comparison, an FEM simulation has been performed with ANSYS in a similar way as described for the previous test case, the result of which is shown in Figure 5.12 b). The corresponding real valued wave numbers have been plotted in Figure 5.11.

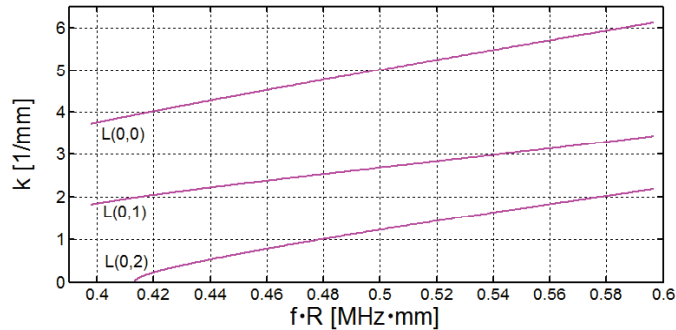


Figure 5.11: Dispersion curves for real valued wave numbers corresponding to a cylindrical rod with varying thickness for an excitation frequency of $\omega = 2.5$ MHz.

As shown in Figure 5.11, $L(0,0)$ and $L(0,1)$ are propagating modes throughout the entire waveguide while $L(0,2)$ switches from an evanescent mode to a propagating mode at a sufficient thickness. The largest wave number to be found in Figure 5.11 is $k = 6.125$ 1/mm which corresponds to a wavelength of about 1.03 mm.

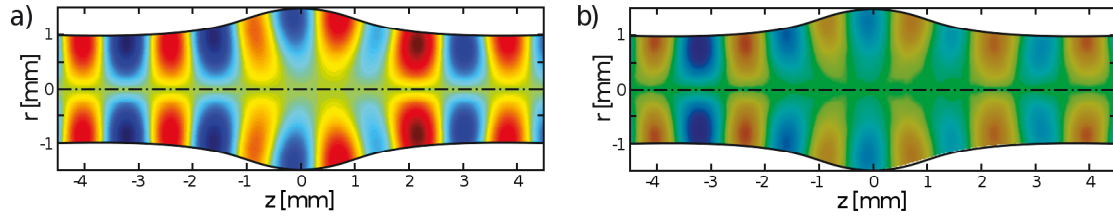


Figure 5.12: Displacement field in r -direction in a cylindrical rod with varying thickness for an excitation frequency of $\omega = 2.5$ MHz simulated with a) multimodal method and b) ANSYS with red for positive and blue for negative displacement.

The results obtained with the multimodal method (Figure 5.12 a)) and through the FEM simulation (Figure 5.12 b)) generally are in good agreement. On close examination there appears to be a slight mismatch regarding the wavelength displayed in the displacement field which becomes most noticeable at the end of the waveguide.

The simulation result for the displacement field in r -direction for an excitation of the $L(0,0)$ -mode at a frequency of $\omega = 2.75$ MHz ($f \approx 0.44$ MHz), obtained with the multimodal method, is plotted in Figure 5.14 a). The FEM simulation used for comparison has been performed using ANSYS. The result can be found in Figure 5.14 b). Figure 5.13 shows the real valued wave numbers corresponding to this test case.

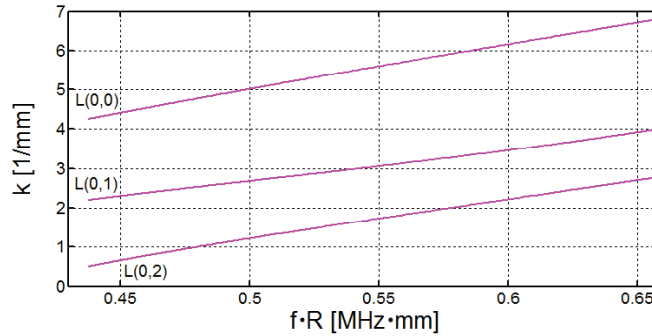


Figure 5.13: Dispersion curves for real valued wave numbers corresponding to a cylindrical rod with varying thickness for an excitation frequency of $\omega = 2.75$ MHz.

The displacement field shown in Figure 5.14 is composed of the axially symmetric modes $L(0,0)$, $L(0,1)$ and $L(0,2)$ which are propagating modes throughout the entire waveguide (see Figure 5.13). The largest wave number in Figure 5.13 is $k = 6.783$ 1/mm which corresponds to a minimum wavelength of approximately 0.93 mm. Even though there are small local deviations, the displacement field calculated with the multimodal method (Figure 5.14 a)) is very similar to the displacement field obtained from the FEM simulation (Figure 5.14 b)). As in the previous test case, there seems to be a slight mismatch between the multimodal and the FEM simulation regarding the predominant wavelength displayed within the displacement field.

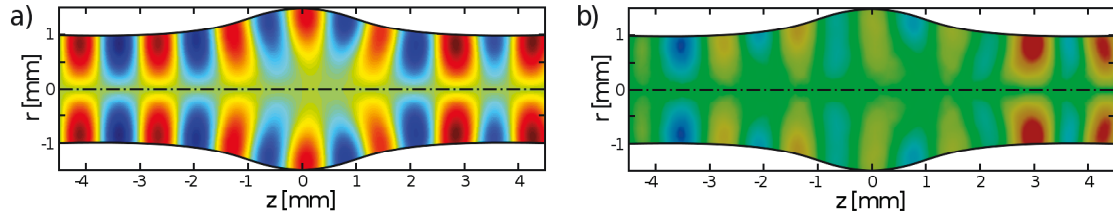


Figure 5.14: Displacement field in r -direction in a cylindrical rod with varying thickness for an excitation frequency of $\omega = 2.75$ MHz simulated with a) multimodal method and b) ANSYS with red for positive and blue for negative displacement.

Figure 5.16 a) shows the simulation result obtained via multimodal method for the displacement field in r -direction for an excitation of the $L(0,0)$ -mode at $\omega = 3.75$ MHz ($f \approx 0.60$ MHz). The result of the corresponding FEM simulation, which has been performed with ANSYS is shown in Figure 5.16 b). The corresponding dispersion curves of the real valued wave numbers are plotted in Figure 5.15.

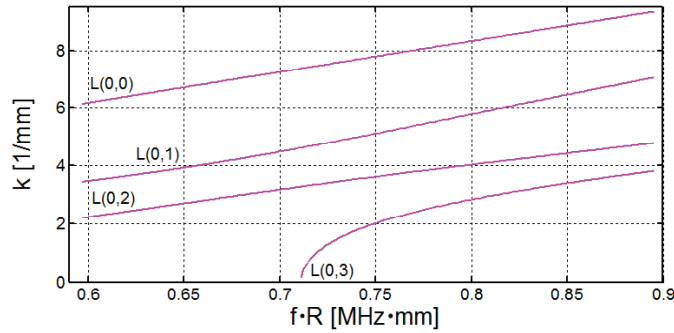


Figure 5.15: Dispersion curves for real valued wave numbers corresponding to a cylindrical rod with varying thickness for an excitation frequency of $\omega = 3.75$ MHz.

As shown in Figure 5.15 the modes $L(0,0)$, $L(0,1)$ and $L(0,2)$ contribute to the displacement field in Figure 5.16 as propagating modes throughout the entire waveguide while the $L(0,3)$ -mode hits two Cutoff cross-sections located around the waveguide's center. The largest wave number in Figure 5.15 is $k = 9.323$ 1/mm, the corresponding wavelength is approximately 0.67 mm. The result obtained by use of the multimodal method (Figure 5.16 a)) contains some artifacts in form of slight discontinuities within the sound field around the center of the waveguide which hints to the fact that the multimodal method as implemented in this work runs into numerical instabilities at these points. Nevertheless, with the exception of those artifacts and other minor local deviations, the displacement field obtained from the multimodal method (Figure 5.16 a)) can be considered to be in good agreement with the result obtained from the FEM simulation (Figure 5.16 b)).

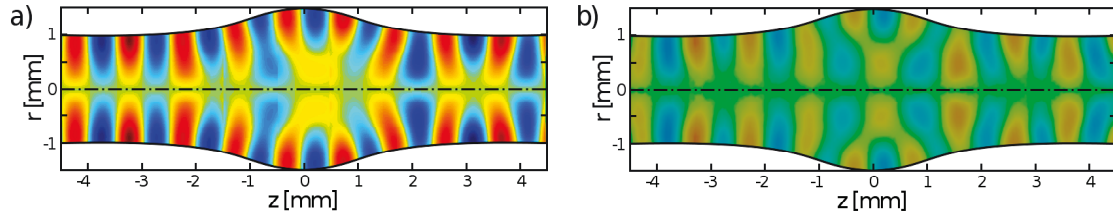


Figure 5.16: Displacement field in r -direction in a cylindrical rod with varying thickness for an excitation frequency of $\omega = 3.75$ MHz simulated with a) multimodal method and b) ANSYS with red for positive and blue for negative displacement.

The artifacts observed in Figure 5.16 a) can be explained by investigating the dispersion curves for the fourth test case chosen to validate the implementation for cylindrical rods. Real and imaginary parts of the wave numbers have been plotted over the product of frequency f and radius R in Figure 5.17 a) and Figure 5.17 b), respectively.

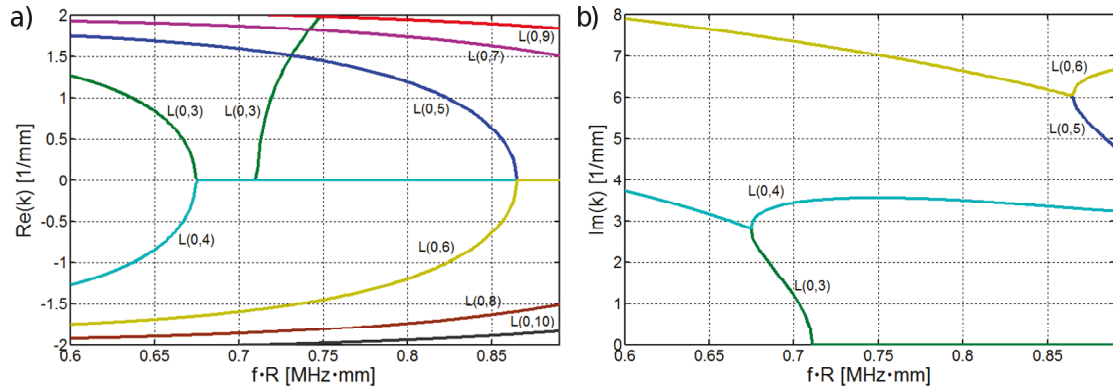


Figure 5.17: Dispersion curves of the cylindrical rod with varying radius for an excitation frequency of $\omega = 3.75$ MHz split into a) real part and b) imaginary part of the wave numbers plotted over frequency-radius product.

As can be seen in Figure 5.17 a), the real parts of the dispersion curves for the $L(0,3)$ and the $L(0,4)$ -mode as well as the ones for the $L(0,5)$ and the $L(0,6)$ -mode show a symmetric behaviour similar to that of an irregular Cutoff as described in Chapter 3 for different values of the fR product while the corresponding imaginary parts show bifurcations at the same points (5.17 b)). It has been pointed out in Chapter 3 that the modal basis loses its orthogonality at such points thus leading to ill conditioned matrices during the process of solving the differential equations. Even though the simulation performed with the multimodal method did not completely break down for the test case investigated in this work, the fact that the wave numbers of two neighbouring modes coincide at these critical points suggests that avoiding instabilities in their presence is not trivial and that a simple extrapolation as used for passing over regular Cutoffs will

not suffice². At an irregular Cutoff, two neighbouring wavemodes coincide at a nonzero real wave number while at the critical points observed in Figure 5.17 two neighbouring wavemodes coincide at a purely imaginary wave number. Given this similarity it can be expected that instabilities at both types of critical points can be avoided by the same methods which will be discussed in Chapter 6.

5.3 Hollow cylinders

In order to test the adaptation of the multimodal method to hollow cylinders as described in Chapter 4, displacement fields in r -direction have been calculated in a hollow cylinder of varying outer radius R_O and constant inner radius R_I for different frequencies. The results obtained by use of the multimodal method have been compared to those of corresponding FEM simulations. The simulations with the multimodal method have been carried out using MATLAB R2007b (Ver. 7.5.0.342) with the initial excitation limited to the axisymmetric $L(0,0)$ -mode. Since the iterative procedure to improve the accuracy of wave numbers showed a tendency to fail to reach the preset threshold more often with increasing order of modes³, the total number of calculated modes has been limited to $N = 17$ as for the simulations in plates. The FEM simulations were carried out with ANSYS 16.0 (Ver. 16.0.0.78) with a mode selective excitation in favour of the $L(0,0)$ -mode.

The hollow cylinder was modelled as a modified version of the previously used cylindrical rod with the material described by the density $\rho = 1 \text{ mg/mm}^3$ and the Lamé constants $\lambda = 2.48/(0.38\pi^2) \text{ GPa}$ and $\mu = 4/\pi^2 \text{ GPa}$ and the geometry defined by

$$R_O = R_1 + (2R_0 - R_1)e^{-\frac{z^2}{L^2}} \quad (5.6)$$

and

$$R_I = 0.5R_0 \quad (5.7)$$

with $R_0 = 1 \text{ mm}$, $R_1 = 1.5 \text{ mm}$ and $L = 1.5 \text{ mm}$.

As in the previous geometries, the smallest wavelengths contributing to the simulations can be expected to be approximately 1 mm. The discretization step size in the direction of wave propagation was set to $\Delta z = 0.1 \text{ mm}$ for the multimodal method. The FEM simulations carried out in ANSYS used a mesh with rectangular elements at a fixed size of 0.1 mm. A resolution of $\Delta t = 10^{-7} \text{ s}$ has been used in time dependence of the sound fields in the FEM simulations.

The displacement fields in r -direction are plotted in Figure 5.19 for an excitation of the

²This simple option has been tested regardless but, as expected, failed to produce satisfactory results.

³The desired threshold was set to 10^{-5} . For a large number of wave numbers the iterative procedure hit an ending condition at a functional value of the dispersion relation between 10^{-3} and 10^{-2} . For few individual wave numbers, the iterative procedure was terminated at a functional value of the dispersion relation of about 10^{-1} .

$L(0,0)$ -mode at $\omega = 0.95$ MHz ($f \approx 0.15$ MHz). The result obtained with the multimodal method is shown in Figure 5.19 a) while the displacement field obtained from FEM simulations carried out with ANSYS is plotted in Figure 5.19 b). The corresponding dispersion curves of the real valued wave numbers have been plotted in Figure 5.18.

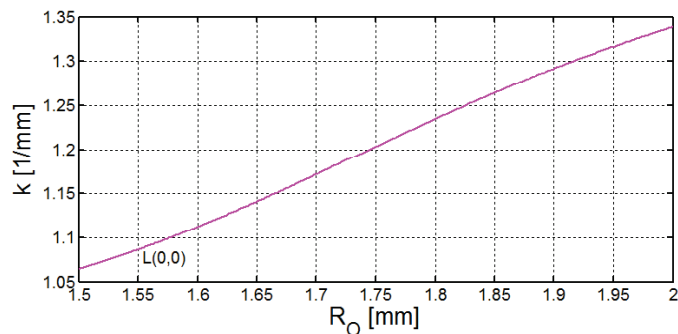


Figure 5.18: Dispersion curves for real valued wave numbers corresponding to a hollow cylinder with varying outer radius for an excitation frequency of $\omega = 0.95$ MHz.

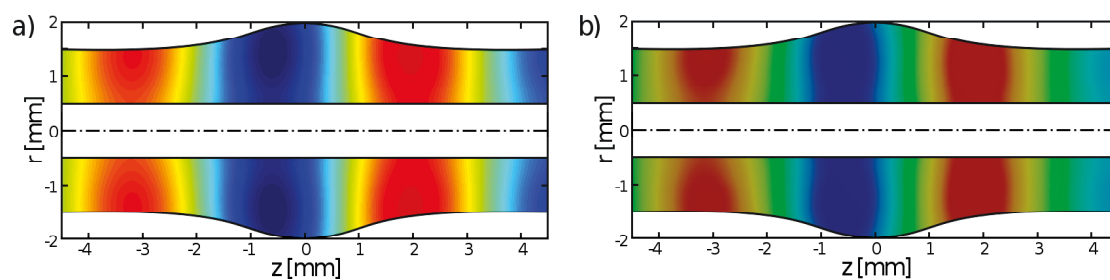


Figure 5.19: Displacement field in r -direction in a hollow cylinder with varying outer radius for an excitation frequency of $\omega = 0.95$ MHz simulated with a) multimodal method and b) ANSYS with red for positive and blue for negative displacement.

As shown in Figure 5.18, the $L(0,0)$ -mode is the only propagating mode throughout the entire waveguide in displacement field shown in Figure 5.19 with a maximum wave number of $k = 1.339$ 1/mm and thus a minimum wavelength of about 4.69 mm. The use of different color scales in both tools notwithstanding, the multimodal method (Figure 5.19 a)) and the FEM simulation (Figure 5.19 b)) yield identical results for the displacement field in r -direction.

Figure 5.21 a) shows the displacement fields in r -direction for an excitation of the $L(0,0)$ -mode at $\omega = 1.55$ MHz ($f \approx 0.25$ MHz). The displacement field obtained from FEM simulations for comparison is plotted in Figure 5.21 b). Figure 5.20 shows the real valued wave numbers corresponding to this test case.

In the case plotted in Figure 5.21 $L(0,0)$ and $L(0,1)$ are propagating modes throughout

the entire waveguide while $L(0, 2)$ switches from an evanescent mode to a propagating mode (see Figure 5.20). The largest wave number in Figure 5.20 is $k = 2.649$ 1/mm which corresponds to a wavelength of approximately 2.37 mm.

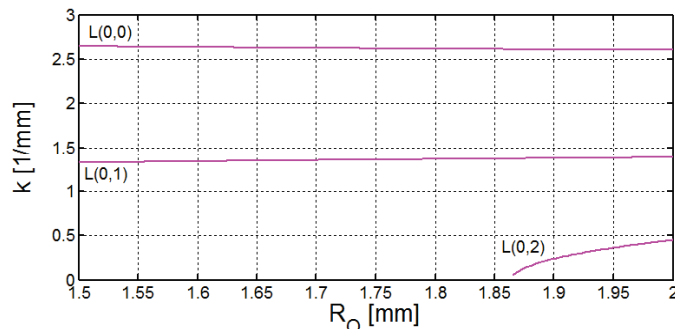


Figure 5.20: Dispersion curves for real valued wave numbers corresponding to a hollow cylinder with varying outer radius for an excitation frequency of $\omega = 1.55$ MHz.

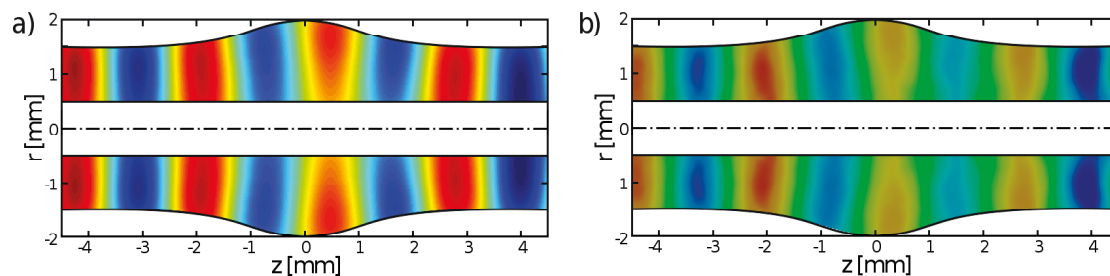


Figure 5.21: Displacement field in r -direction in a hollow cylinder with varying outer radius for an excitation frequency of $\omega = 1.55$ MHz simulated with a) multimodal method and b) ANSYS with red for positive and blue for negative displacement.

The displacement field in r -direction which was calculated using the multimodal method (Figure 5.21 a)) is in good agreement with the corresponding result from the FEM simulation (Figure 5.21 b)).

The simulation result for the displacement field in r -direction for an excitation of the $L(0, 0)$ -mode at a frequency of $\omega = 2.2$ MHz ($f \approx 0.35$ MHz), obtained with the multimodal method, is plotted in Figure 5.23 a). The result of the FEM simulations used for comparison can be found in Figure 5.23 b) while the corresponding dispersion curves of the real valued wave numbers are plotted in Figure 5.22.

As shown in Figure 5.22, the displacement field shown in Figure 5.23 is composed of the axially symmetric modes $L(0, 0)$, $L(0, 1)$ and $L(0, 2)$ which are propagating modes throughout the entire waveguide. The largest wave number to be found in Figure 5.22 is $k = 3.837$ 1/mm with a corresponding wavelength of about 1.64 mm. Even though

some local minor deviations can be found, the multimodal method (Figure 5.23 a)) and the FEM simulation (Figure 5.23 b)) yield the same result for the displacement field in r -direction.

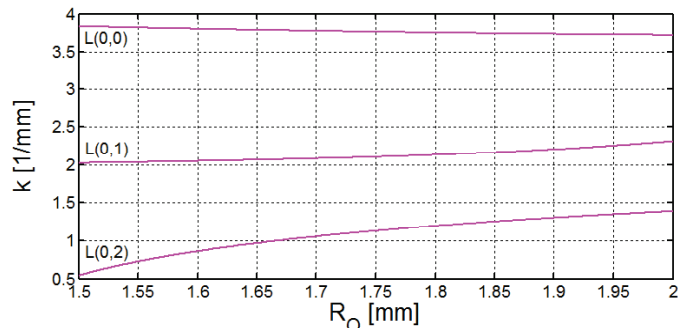


Figure 5.22: Dispersion curves for real valued wave numbers corresponding to a hollow cylinder with varying outer radius for an excitation frequency of $\omega = 2.2$ MHz.

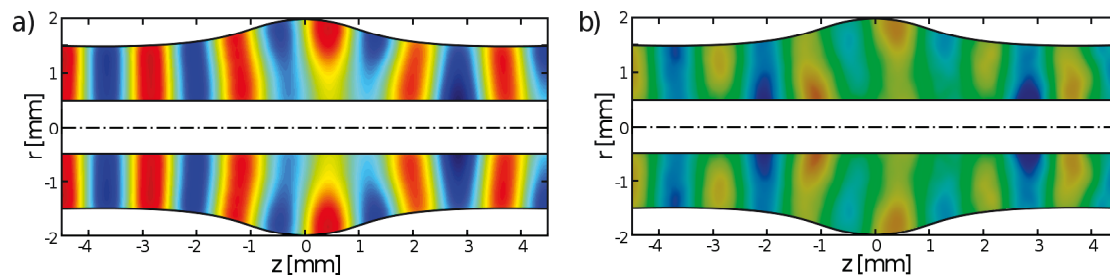


Figure 5.23: Displacement field in r -direction in a hollow cylinder with varying outer radius for an excitation frequency of $\omega = 2.2$ MHz simulated with a) multimodal method and b) ANSYS with red for positive and blue for negative displacement.

5.4 Efficiency compared to FEM

In order to evaluate its potential advantages, computation times for simulations using the multimodal method were compared with those needed for FEM-simulation for the simple test case of a $2 \mu\text{s}$ sinusburst excitation pulse with a center frequency of 2 MHz propagating through waveguides with constant thickness. The waveguides were plates and cylindrical rods made of isotropic steel defined by the density $\rho = 7.866 \text{ mg/mm}^3$ and the Lamé constants $\lambda = 112.4 \text{ GPa}$ and $\mu = 81.4 \text{ GPa}$. To document the influence of different geometric parameters in FEM as well as multimodal method, two different values for the waveguide's thickness (1 mm and 3 mm) have been combined with two different values for the waveguide's length (150 mm and 300 mm). The parameters for the simulations were set up to ensure a short computation time without sacrificing a significant amount of accuracy.

5.4.1 Simulations in plates

The Simulations for pulse propagation through plates were performed on a server dedicated to numerical simulations which was equipped with two Intel(R) Xeon(R) CPU X5650 @2.67 GHz processors (12 cores in total) and 94.6 GB RAM. Simulations using the multimodal approach have been carried out in MATLAB R2012a (Ver. 7.14.0.739). The smallest wavelength to be expected for the S_0 -mode is approximately 1.15 mm. In the multimodal method, the discretization in x -direction was set to a step size of 0.1 mm. The FEM based simulations have been done in COMSOL 4.0a (Ver. 4.0.0.982) with the mesh size ranging from a minimum of 0.01 mm to a maximum of 0.5 mm using triangular elements. The resulting average element size was about 0.25 mm for $d = 1$ mm and approximately 0.30 mm for $d = 3$ mm. The simulations in plates run from $t = 0$ to $t = 53 \mu\text{s}$, using time steps of $0.1 \mu\text{s}$ and mode selective excitation of the S_0 -mode has been applied. These simulations have been discussed in more detail in [74], the obtained results for the computation times are repeated in Table 5.1.

Table 5.1: Computation times for the simulation of S_0 pulse propagation through plates.

	$d = 1$ mm $L = 150$ mm	$d = 1$ mm $L = 300$ mm	$d = 3$ mm $L = 150$ mm	$d = 3$ mm $L = 300$ mm
Multimodal method	35 s	63 s	36 s	62 s
COMSOL	314 s	560 s	628 s	1073 s

As can be seen, computation times increase approximately linearly with the plate length in both simulation methods. An increase in plate thickness has basically no effect on the computation time needed with the multimodal method while the calculation time needed with COMSOL increased significantly. Given that the multimodal method reduces the numerical effort to the direction of wave propagation, i.e. along the length of the plate, this observation was to be expected. The notable point in Table 5.1 is that even for the smallest plate geometry the computation time needed with the multimodal method differs from those needed with FEM approximately by a factor of nine. For larger waveguides the difference is even more pronounced and in the examples documented in Table 5.1 goes up to a factor of approximately 17. While in general computation times heavily depend on the specific problem and neither the multimodal nor the FEM simulations have been fully optimized, the choices of sampling rate in time dependence and mesh size or discretization step size compared to frequency and wavelength as used here can be considered representative for practical applications. Thus the obtained results confirm that, compared to FEM, the use of the multimodal method could potentially shorten the computation times needed for numerical simulations of wave propagation through a waveguide by about one order of magnitude.

5.4.2 Simulations in cylindrical rods

The simulations for pulse propagation through cylindrical rods were performed on a desktop PC equipped with an Intel(R) Core(TM) i7 CPU 860 @2.80 GHz processor (4 cores) and 8 GB RAM. Similar to the plate geometry, the smallest wavelength to be expected for the $L(0,0)$ -mode is approximately 1.15 mm. Simulations using the multimodal method have been carried out in MATLAB R2007b (Ver. 7.5.0.342) with the step size for the discretization in z -direction set to 0.1 mm. The FEM simulations have been carried out using ANSYS 16.0 (Ver. 16.0.0.78). The mesh was fixed to an element size of 0.1 mm using rectangular elements. In order to reduce the computation times in ANSYS, the axisymmetric problems have been approximated by 2D-calculations. The simulations in cylindrical rods run from $t = 0$ to $t = 55 \mu\text{s}$, using time steps of $0.1 \mu\text{s}$ with mode selective excitation applied in favour of the $L(0,0)$ -mode. While a more detailed discussion of these simulations can be found in [75], the obtained computation times are given in Table 5.2.

Table 5.2: Computation times for the simulation of $L(0,0)$ pulse propagation through cylindrical rods.

	$R = 0.5 \text{ mm}$ $L = 150 \text{ mm}$	$R = 0.5 \text{ mm}$ $L = 300 \text{ mm}$	$R = 1.5 \text{ mm}$ $L = 150 \text{ mm}$	$R = 1.5 \text{ mm}$ $L = 300 \text{ mm}$
Multimodal method	46 s	83 s	55 s	100 s
ANSYS	382 s	899 s	1317 s	2686 s

Similar to the simulations in plates, computation times increase more or less linearly with the rod length in both simulation methods. The computation time needed with ANSYS increased significantly with larger radius R while the influence on computation times of the multimodal approach were much less pronounced. The reason why in contrast to the implementation for plates an increase in thickness leads to an increase in computation time for the multimodal method is that calling a Bessel function in MATLAB is more time consuming than calling a sine or cosine function. If the radius R is increased while the discretization in r -direction is kept fixed, Bessel functions have to be evaluated more often.

For the smallest geometry, the multimodal approach is still about 8 times faster than FEM while for the largest waveguide, this difference increases up to a factor of about 27. These results were obtained using a 2D axisymmetric approximation in ANSYS. If modes of higher order in circumferential direction were to be taken into account a full 3D FEM simulation would be required which would significantly increase the computation time of the FEM simulations. However, at the same time a larger number of different families of modes would have to be included in the multimodal method in order to model a non-axisymmetric excitation with sufficient accuracy which makes predictions about the difference in computation times between FEM and multimodal method for a full 3D

case, without testing an actual implementation, somewhat unreliable.

Chapter 6

Conclusions and future work

6.1 Evaluation of the multimodal approach

The use of the multimodal method in applications for the simulation of guided waves in elastic waveguides has been investigated. The implementation of the multimodal approach as suggested by Pagneux and Maurel [17] for plates with symmetrically varying thickness was successfully reproduced and slightly modified to account for plates with asymmetrically varying thickness as well. Furthermore, the multimodal approach has been extended to cylindrical geometries and validated for axially symmetric guided wave modes in cylindrical rods and hollow cylinders. While there remain some open problems that limit the use of the multimodal method for practical applications, the results obtained in the investigated test cases are promising. By using the case of a pulse propagation through a waveguide with constant thickness, it could be confirmed that the multimodal method yields the potential to be at least one order of magnitude faster than simulations with commercially available software based on the Finite Element Method and becomes increasingly advantageous for thick walled waveguides.

It has been shown in Chapter 5, that the multimodal method provides displacement fields very similar to those obtained from simulations with commercially available FEM based software for different types of waveguides with varying thickness. Even though the results of multimodal method and the Finite Element Method generally were in good agreement, small deviations can arise for a variety of reasons. First and foremost it is important to note that the multimodal method using physical guided wave modes of corresponding waveguides with constant thickness as basis will converge somewhat slowly towards the physical displacement field of the waveguide with varying thickness [24]. If an insufficient number of evanescent modes is used in addition to the propagating wave modes, non-physical fine structures may arise in the displacement field obtained from the multimodal method. In the two test cases for cylindrical rods displayed in Figure 5.12 and Figure 5.14, some slight deviations between in the periodicity of the displacement fields obtained by use of the multimodal method and those extracted from FEM simulations have been observed. When using ANSYS, time dependant simulations can lead

to erroneous results in terms of wavelengths if the set value for time steps is too large. However, this problem has been observed in FEM simulations that were carried out with ANSYS at an early stage of this work and some care has been taken to avoid it in the test cases documented in this thesis¹. Another possible explanation is a slight difference in the relative weights of the modes contributing to the displacement field. In the multimodal method, starting values are set for the coefficient vector \vec{a} and the impedance matrix \mathbf{Z} while in FEM simulations a time dependant displacement is set on defined parts of the waveguide's surface as excitation. Even if the excitation is set to favour the lowest order guided wave mode, the fact that it is applied to a limited area will effectively lead to a range of excited wave numbers which might result into some energy being transferred into higher order propagating modes which in turn will lead to slightly different compositions of the displacement fields in FEM simulations and the multimodal method if these initial small contributions of higher order modes are neglected in the latter. In general, it could be observed that differences between results obtained via multimodal methods and those obtained from FEM simulations are larger if more propagating modes are involved. While the aforementioned imperfections in the mode selective excitation in FEM simulations offers an explanation for this, another contributing factor might be that the total number of calculated modes N was fixed for all test cases in one type of waveguide which might lead to a decrease in accuracy as less additional evanescent modes are considered for a higher number of propagating modes.

As discussed in Chapter 3, a key requirement for a successful application of the multimodal method is a sufficient accuracy of the wave numbers involved. More precisely, the functional value of the dispersion relation has to be close to zero for the wave numbers used in the multimodal method. As pointed out in Chapter 3, the tolerable deviation of wave numbers from actual zeros of the dispersion relation decreases with increasing frequency. Since the achievable accuracy of wave numbers is limited by the machine epsilon, this implies the existance of a critical frequency for any given waveguide above which the multimodal method will start to fail. In this work, no fixed accuracy was imposed on the calculated wave numbers. Instead an iterative procedure has been used to gradually improve the wave number's accuracy until the functional value of the dispersion relation drops below a preset threshold. Practical experience with this method have shown that the iterative procedure can run into a state which requires to terminate it before reaching the desired threshold. This has been observed for guided wave modes of high order which suggests that there is also a limit on the total number of calculated modes N . While the specific maximum value of N will depend on the type of waveguide as well as other parameters, it can be stated that this issue is more prominent for hollow cylinders where the density of dispersion curves is higher than for cylindrical rods or plates where the equivalent of L -modes splits into two separate families namely A - and S -modes. In addition, the iterative procedure can become expensive in terms of computation time if

¹In fact the time steps of 10^{-8} to 10^{-7} s that have been chosen in the simulations documented in Chapter 5 provide sampling rates for the resolution of time dependence that are significantly higher than the frequencies involved in the simulations which should reliably eliminate this particular source of errors.

a large number of complex wave numbers have to be processed for different values for thickness or frequency. For some of the test cases documented in Chapter 5, the time needed for the iterative improvement of wave numbers made up about 90 percent of the total computation time thus potentially negating the advantage of the multimodal method over FEM. If a large number of simulations has to be conducted in the same waveguide, this can be compensated by computing the wave numbers for a sufficiently large range of frequencies and storing them in a look up table for later use thereby reducing the computationally expensive iterative improvement of wave numbers to a one time effort.

One interesting feature of the multimodal method is that information about individual contributions of single guided wave modes are easily accessible. As shown in (3.27) and (3.28), entries in the coefficient vectors \vec{a} and \vec{b} correspond to individual modes of a waveguide with constant thickness. Using (3.29) and (3.30), the coefficients c_n^- and c_n^+ for left going and right going n -th guided wave mode can be extracted from a_n and b_n which provides detailed information about reflection and energy transfer for every individual mode. As has been pointed out by Pagneux and Maurel in [17], the results obtained via multimodal method can also be used to calculate local reflection and transmission coefficients at any point along the waveguide.

6.2 Possible application in structural health monitoring and non-destructive testing of wheelset-axles

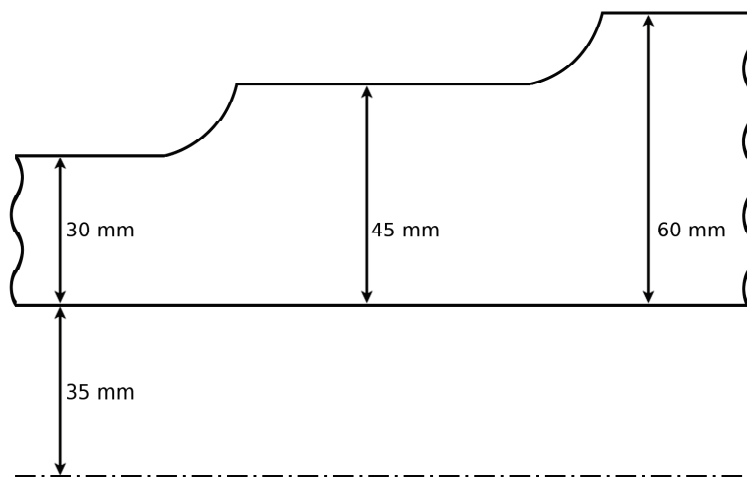


Figure 6.1: Inner radius and various values for the thickness of wheelset-axles.

After evaluating the extension of the multimodal method to cylindrical rods and hollow cylinders in general, the specific application on wheelset-axles will be discussed in this

section. The transition between different outer radii including realistic measures for the inner radius and different values of the thickness in a wheelset-axle is illustrated in Figure 6.1 with the position of the central axis marked by a dash-dotted line.

Given the limitations in the applicability of the multimodal method in terms of frequency f and maximum number of calculated modes N which have been pointed out in the previous section and considering the geometric parameters and frequencies used in the test cases in Chapter 5, a reliable application of the multimodal method in wheelset-axles can be expected for frequencies up to $f \approx 100$ kHz.

For a practical application on real waveguides, a couple of points will have to be addressed. In the simulations documented in Chapter 5, some care has been taken to avoid the presence of irregular Cutoffs within the waveguide and thus corresponding numerical instabilities in the multimodal method. In a realistic scenario, the geometry of the waveguide is determined and the choice of frequencies limited by the available transducers. Therefore, an effective treatment of irregular Cutoffs and equivalent points of instability (e.g. a coincidence of neighbouring modes at a nonzero imaginary value) has to be implemented in order to ensure a more general applicability. Another potential issue is the variation of thickness itself. As can be seen in Figure 6.1, the function that describes the change of the outer radius R_O along the direction of wave propagation in a realistic wheelset-axle contains some points where it is not differentiable. These points will cause artifacts in the numerical differentiation if left unchecked. In Chapter 3, a similar problem has been addressed with respect to Cutoffs as non-differentiable points in complex dispersion curves. The suggested solutions for wave numbers was to identify critical points in $k_n(z)^2$ and split the function at these points in order to perform a piecewise numerical differentiation. For applications on wheelset-axles, a similar procedure would have to be applied on $R_O(z)$. Finally, the calculated sound fields inside the waveguide might deviate from the actual sound field if the initial excitation of modes is modelled incorrectly, especially if a large number of modes can potentially propagate. This problem could be avoided by either projecting the given excitation onto the modal basis in order to determine the initial weights or by modelling the response to a given excitation with a different method (e.g. FEM or SBFEM) and to extract information about the relative weight of excited guided wave modes from the results before continuing to simulate the signal propagation through the waveguide via multimodal method.

With the state of the adaptation to cylindrical waveguides documented in this thesis, the multimodal method could be used in a limited manner for the structural health monitoring of wheelset-axles. If an axially symmetric excitation is applied, the wave propagation through a waveguide without any breeches of axial symmetry can be simulated. If significant deviations between a measured signal and the simulated signal are observed, they will arise from deviations of the real wave guide from perfect axial symmetry (e.g. cracks). This would allow to detect the presence of flaws but not their classification. In order to classify flaws in a testing scenario, a large number of simulations would have

²or $k_n(x)$ in case of plates

to be carried out to determine the influence of different positions and sizes of flaws on an ultrasound pulse propagating through the axle. In particular this would require an extension to guided wave modes of higher circumferential order to simulate the coupling into non-axially symmetric wave modes and thus estimate which contributions of such modes to a measured signal have to be expected for different flaws.

6.3 Outlook

For future works, a couple of goals should be addressed. Some of the most important key points in the further development of a tool for simulations of guided wave propagation in wheelset-axles based on the multimodal method will be discussed in this section to conclude this thesis.

As pointed out before, covering more than just axially symmetric L -modes in simulations would be desirable for a variety of reasons. In the current implementation, this would require an extension of the multimodal method itself and an extension of the calculation of wave numbers via spectral decomposition method. Judging by the experiences made in the extension of the multimodal method to plates with asymmetrically varying thickness, the matrix equations used in the multimodal method would have to be reorganized in a block-representation with off-diagonal blocks describing coupling between different families of modes. While this was restricted to A - and S -modes in plates, cylindrical waveguides may contain an infinite number of different families of F -modes (i.e. modes of higher circumferential order). As a result, non-axially symmetric contributions would have to be approximated by truncating the calculated F -modes (described by $F(m, n)$) not only at a maximum radial order $n = N$ but also at a maximum circumferential order $m = M$. Further investigations would be required in order to identify possible convergence issues arising from this truncation.

For further development towards an unrestricted practical applicability of the multimodal method, a stable treatment of irregular Cutoffs and their counterparts on the imaginary axis is imperative. Pagneux et al. initially suggested the use of solvers for differential equations using an adaptive step size to pass over points of instability [17] and in fact it might be worth testing different implementations of such solvers to determine which offers the best performance for the particular problem. However, in later works (e.g. [24] and [25]) they apparently opted to use a non-physical orthogonal basis instead of physical modes of corresponding waveguides with constant thickness in a so called improved multimodal method. This does offer the advantage that physical Cutoffs will no longer be associated with instabilities in the multimodal method, however, the functions used in the new basis could contain other (non-physical) Cutoffs that are associated with similar problems. If the basis functions do not resemble physical guided wave modes, it is not as straightforward to see which steps have to be taken in order to ensure that an overlap of these functions converges towards a physical solution for the given waveguide. Given that the published applications of the improved multimodal method seem to be limited to

aeroacoustic applications, some additional work might be required to adapt the method to elastic waveguides. Another minor disadvantage of using a non-physical basis is that information about the behaviour of specific guided wave modes can not be accessed directly anymore. In order to achieve reliable stability of the multimodal method, the best approach might be to transform equations between two different orthogonal bases as needed to avoid points of instability entirely.

Another interesting point mentioned in the description of the improved multimodal method [24] with respect to aeroacoustic applications, is the introduction of a boundary mode which is constructed specifically to account for the physical boundary conditions of a waveguide with varying cross-section. This would allow to greatly reduce the total number of calculated modes N and thus the computational effort since, according to [24], considering all propagating modes, one evanescent mode and the boundary mode would be sufficient. For future work, it could be worthwhile to investigate how a boundary mode would have to be constructed for an elastic waveguide in order to increase the efficiency of the implementation.

Since the iterative improvement of the accuracy of wave numbers is the most time consuming step in the current implementation, it is the most promising area for investigating options to further reduce the computation time. Possible approaches to accomplish this goal could include either the optimization of the currently implemented method or an evaluation of possible alternatives like calculations of wave numbers based on SBFEM³.

³see e.g. [58–61]

Appendix A

Dispersion relation of hollow cylinders

The dispersion relation of a hollow cylinder can be written in the form

$$\frac{1}{R_O R_I} \left(\tilde{D}_1 + \tilde{D}_2 + \tilde{D}_3 + \tilde{D}_4 + \tilde{D}_5 + \tilde{D}_6 \right) = 0 \quad (\text{A.1})$$

with

$$\begin{aligned} \tilde{D}_1 = & (k^2 - \beta^2)^2 [J_1(\beta R_O)Y_1(\beta R_I) - J_1(\beta R_I)Y_1(\beta R_O)] \\ & \cdot [((k^2 - \beta^2)R_O Y_0(\alpha R_O) + 2\alpha Y_1(\alpha R_O)) ((k^2 - \beta^2)R_I J_0(\alpha R_I) + 2\alpha J_1(\alpha R_I)) \\ & - ((k^2 - \beta^2)R_I Y_0(\alpha R_I) + 2\alpha Y_1(\alpha R_I)) ((k^2 - \beta^2)R_O J_0(\alpha R_O) + 2\alpha J_1(\alpha R_O))] \end{aligned} \quad (\text{A.2})$$

$$\begin{aligned} \tilde{D}_2 = & 4k^2(k^2 - \beta^2)\alpha [Y_1(\alpha R_O)Y_1(\beta R_I) - Y_1(\alpha R_I)Y_1(\beta R_O)] \\ & \cdot [(\beta R_O J_0(\beta R_O) - J_1(\beta R_O)) ((k^2 - \beta^2)R_I J_0(\alpha R_I) + 2\alpha J_1(\alpha R_I)) \\ & - (\beta R_I J_0(\beta R_I) - J_1(\beta R_I)) ((k^2 - \beta^2)R_O J_0(\alpha R_O) + 2\alpha J_1(\alpha R_O))] \end{aligned} \quad (\text{A.3})$$

$$\begin{aligned} \tilde{D}_3 = & 4k^2(k^2 - \beta^2)\alpha [J_1(\beta R_O)Y_1(\alpha R_I) - J_1(\beta R_I)Y_1(\alpha R_O)] \\ & \cdot [(\beta R_O Y_0(\beta R_O) - Y_1(\beta R_O)) ((k^2 - \beta^2)R_I J_0(\alpha R_I) + 2\alpha J_1(\alpha R_I)) \\ & - (\beta R_I Y_0(\beta R_I) - Y_1(\beta R_I)) ((k^2 - \beta^2)R_O J_0(\alpha R_O) + 2\alpha J_1(\alpha R_O))] \end{aligned} \quad (\text{A.4})$$

$$\begin{aligned} \tilde{D}_4 = & 4k^2(k^2 - \beta^2)\alpha [J_1(\alpha R_O)Y_1(\beta R_I) - J_1(\alpha R_I)Y_1(\beta R_O)] \\ & \cdot [((k^2 - \beta^2)R_O Y_0(\alpha R_O) + 2\alpha Y_1(\alpha R_O)) (\beta R_I J_0(\beta R_I) - J_1(\beta R_I)) \\ & - ((k^2 - \beta^2)R_I Y_0(\alpha R_I) + 2\alpha Y_1(\alpha R_I)) (\beta R_O J_0(\beta R_O) - J_1(\beta R_O))] \end{aligned} \quad (\text{A.5})$$

$$\begin{aligned} \tilde{D}_5 = & 4k^2(k^2 - \beta^2)\alpha [J_1(\alpha R_O)J_1(\beta R_I) - J_1(\alpha R_I)J_1(\beta R_O)] \\ & \cdot [(\beta R_O Y_0(\beta R_O) - Y_1(\beta R_O)) ((k^2 - \beta^2)R_I Y_0(\alpha R_I) + 2\alpha Y_1(\alpha R_I)) \\ & - (\beta R_I Y_0(\beta R_I) - Y_1(\beta R_I)) ((k^2 - \beta^2)R_O Y_0(\alpha R_O) + 2\alpha Y_1(\alpha R_O))] \end{aligned} \quad (\text{A.6})$$

$$\begin{aligned}
\tilde{D}_6 = & 16k^4\alpha^2 [J_1(\alpha R_O)Y_1(\alpha R_I) - J_1(\alpha R_I)Y_1(\alpha R_O)] \\
& \cdot [(\beta R_O Y_0(\beta R_O) - Y_1(\beta R_O))(\beta R_I J_0(\beta R_I) - J_1(\beta R_I)) \\
& - (\beta R_I Y_0(\beta R_I) - Y_1(\beta R_I))(\beta R_O J_0(\beta R_O) - J_1(\beta R_O))].
\end{aligned} \tag{A.7}$$

The factor $1/(R_O R_I)$ could be omitted in (A.1), however, doing so would affect the results of an iterative procedure to shift an approximate value of a wave number k towards a dispersion curve until the absolute value of (A.1) sinks below a preset threshold as applied in this work.

Appendix B

Derivation of matrix elements in \mathbf{N}_1 and \mathbf{N}_4

B.1 Plates

The entries of matrix \mathbf{N}_1 and matrix \mathbf{N}_4 are given by (3.35) and (3.38) respectively. In order to find a closed analytical expression for these entries, the scalar products $\langle \partial_x \vec{X}_m | \vec{Y}_n \rangle$ and $\langle \partial_x \vec{Y}_m | \vec{X}_n \rangle$ have to be evaluated.

The limits of the integration in y -direction that has to be performed to calculate the scalar products are the upper and lower plate surface h_U and h_L . For a plate with varying thickness h_U and h_L are functions of x which means that integration in y - and differentiation in x -direction are no longer commutative. If the x dependent shift in y -direction is applied as in Chapter 3 to account for asymmetrically varying thickness, the commutator between the differential and integral operator is

$$\left[\partial_x f(x, y - \tilde{h}), \int_{h_L}^{h_U} f(x, y - \tilde{h}) dy \right] = (\partial_x h_U) f(x, \bar{h}) - (\partial_x h_L) f(x, -\bar{h}). \quad (\text{B.1})$$

Using this commutator it is easy to show that the biorthogonality relation (3.19) leads to

$$(\partial_x \mathcal{J}_n) \delta_{nm} = \langle \partial_x \vec{X}_n | \vec{Y}_m \rangle + \langle \vec{X}_n | \partial_x \vec{Y}_m \rangle + (\partial_x h_U) \vec{X}_n(\bar{h}) \vec{Y}_m(\bar{h}) - (\partial_x h_L) \vec{X}_n(-\bar{h}) \vec{Y}_m(-\bar{h}). \quad (\text{B.2})$$

The last term in (B.2) can be simplified by taking into account that $\sigma_{xy,n}(\pm\bar{h}) = 0$ for Lamb-modes under the boundary condition of traction free surfaces. The expression

(3.35) for N_1 can now be rewritten as

$$\begin{aligned}
-\mathcal{J}_n N_{1,nm} &= \langle \partial_x \vec{X}_m | \vec{Y}_n \rangle \\
&= \frac{1}{2} \left(\langle \partial_x \vec{X}_m | \vec{Y}_n \rangle + \langle \partial_x \vec{X}_m | \vec{Y}_n \rangle \right) \\
&= \frac{1}{2} \left(\langle \partial_x \vec{X}_m | \vec{Y}_n \rangle - \langle \vec{X}_m | \partial_x \vec{Y}_n \rangle + \partial_x \mathcal{J}_n \right) \\
&\quad + \frac{1}{2} \left((\partial_x h_U) u_{x,m}(\bar{h}) \sigma_{xx,n}(\bar{h}) - (\partial_x h_L) u_{x,m}(-\bar{h}) \sigma_{xx,n}(-\bar{h}) \right) \\
&= \frac{1}{2} (\partial_x \mathcal{J}_n) \delta_{nm} + \frac{1}{2} \left(\left\langle \partial_x \vec{X}_m \left| \frac{ik_n Z_{c,n}}{ik_n Z_{c,n}} \vec{Y}_n \right. \right\rangle - \left\langle \frac{ik_m}{ik_m} \vec{X}_m \left| \partial_x \left(\frac{Z_{c,n}}{Z_{c,n}} \vec{Y}_n \right) \right. \right\rangle \right) \\
&\quad + \frac{1}{2} \left((\partial_x h_U) u_{x,m}(\bar{h}) \sigma_{xx,n}(\bar{h}) - (\partial_x h_L) u_{x,m}(-\bar{h}) \sigma_{xx,n}(-\bar{h}) \right) \\
&= \frac{1}{2} (\partial_x \mathcal{J}_n) \delta_{nm} + \frac{1}{2} \frac{\partial_x Z_{c,n}}{Z_{c,n}} \mathcal{J}_n \delta_{nm} \\
&\quad + \frac{1}{2Z_{c,n}} \left(\frac{1}{ik_n} \langle \partial_x \vec{X}_m | ik_n Z_{c,n} \vec{Y}_n \rangle - \frac{1}{ik_m} \langle ik_m \vec{X}_m | \partial_x (Z_{c,n} \vec{Y}_n) \rangle \right) \\
&\quad + \frac{1}{2} \left((\partial_x h_U) u_{x,m}(\bar{h}) \sigma_{xx,n}(\bar{h}) - (\partial_x h_L) u_{x,m}(-\bar{h}) \sigma_{xx,n}(-\bar{h}) \right) \\
&= \frac{1}{2} (\partial_x \mathcal{J}_n) \delta_{nm} + \frac{1}{2} \frac{\partial_x Z_{c,n}}{Z_{c,n}} \mathcal{J}_n \delta_{nm} \\
&\quad + \frac{1}{2} \left((\partial_x h_U) u_{x,m}(\bar{h}) \sigma_{xx,n}(\bar{h}) - (\partial_x h_L) u_{x,m}(-\bar{h}) \sigma_{xx,n}(-\bar{h}) \right) \\
&\quad + \frac{1}{2Z_{c,n}} \left(\underbrace{\frac{1}{ik_n} \langle \partial_x \vec{X}_m | \mathbf{G} \vec{X}_n \rangle - \frac{1}{ik_m} \langle \mathbf{F} Z_{c,m} \vec{Y}_m | \partial_x (Z_{c,n} \vec{Y}_n) \rangle}_{=\mathcal{B}} \right)
\end{aligned} \tag{B.3}$$

If $\vec{\mathcal{Z}}_1 = (z_{11}, z_{12})^\top$ and $\vec{\mathcal{Z}}_2 = (z_{21}, z_{22})^\top$ are two arbitrary vectors, the operators \mathbf{F} and \mathbf{G} given in (3.12) and (3.13) have the following properties (the corresponding proof can be found in [17])

$$\langle \mathbf{F} \vec{\mathcal{Z}}_1 | \vec{\mathcal{Z}}_2 \rangle = \langle \vec{\mathcal{Z}}_1 | \mathbf{F} \vec{\mathcal{Z}}_2 \rangle + f_1 [z_{11} z_{22} - z_{12} z_{21}]_{h_L}^{h_U} + f_2 [z_{12} \partial_y z_{22} - (\partial_y z_{12}) z_{22}]_{h_L}^{h_U} \tag{B.4}$$

$$\langle \vec{\mathcal{Z}}_1 | \mathbf{G} \vec{\mathcal{Z}}_2 \rangle = \langle \mathbf{G} \vec{\mathcal{Z}}_1 | \vec{\mathcal{Z}}_2 \rangle - [z_{12} z_{21} - z_{11} z_{22}]_{h_L}^{h_U}. \tag{B.5}$$

If the term \mathcal{B} , which still has to be evaluated in (B.3), is written as

$$\begin{aligned}
\mathcal{B} &= \frac{1}{2ik_n} \left(\langle \partial_x \vec{X}_m | \mathbf{G} \vec{X}_n \rangle + \langle \partial_x \vec{X}_m | \mathbf{G} \vec{X}_n \rangle \right) \\
&\quad - \frac{1}{2ik_m} \left(\langle \mathbf{F} Z_{c,m} \vec{Y}_m | \partial_x (Z_{c,n} \vec{Y}_n) \rangle + \langle \mathbf{F} Z_{c,m} \vec{Y}_m | \partial_x (Z_{c,n} \vec{Y}_n) \rangle \right),
\end{aligned} \tag{B.6}$$

(B.4), (B.5) and the identity (3.8) can be used to obtain

$$\begin{aligned}
\mathcal{B} &= \frac{1}{2ik_n} \left(\langle \partial_x \vec{X}_m | \mathbf{G} \vec{X}_n \rangle + \langle \mathbf{G} \partial_x \vec{X}_m | \vec{X}_n \rangle \right) \\
&+ \frac{1}{2ik_n} \left((\partial_x h_U)(\partial_y \sigma_{xy,m})(\bar{h}) u_{x,n}(\bar{h}) - (\partial_x h_L)(\partial_y \sigma_{xy,m})(-\bar{h}) u_{x,n}(-\bar{h}) \right) \\
&- \frac{1}{2ik_m} \left(\langle \mathbf{F} Z_{c,m} \vec{Y}_m | \partial_x(Z_{c,n} \vec{Y}_n) \rangle + \langle Z_{c,m} \vec{Y}_m | \mathbf{F} \partial_x(Z_{c,n} \vec{Y}_n) \rangle \right) \\
&+ \frac{1}{2ik_m} (\partial_x h_U) Z_{c,m} u_{y,m}(\bar{h}) Z_{c,n} (\partial_y \sigma_{yy,n})(\bar{h}) \\
&- \frac{1}{2ik_m} (\partial_x h_L) Z_{c,m} u_{y,m}(-\bar{h}) Z_{c,n} (\partial_y \sigma_{yy,n})(-\bar{h})
\end{aligned} \tag{B.7}$$

With \mathbf{G} applied as given in (3.13), we obtain

$$\begin{aligned}
\langle \partial_x \vec{X}_m | \mathbf{G} \vec{X}_n \rangle + \langle \mathbf{G} \partial_x \vec{X}_m | \vec{X}_n \rangle &= 2\rho\omega^2 \langle \partial_x u_{x,m} | u_{x,n} \rangle + \frac{2}{\mu} \langle \partial_x \sigma_{xy,m} | \sigma_{xy,n} \rangle \\
&+ \langle \partial_x u_{x,m} | \partial_y \sigma_{xy,n} \rangle + \langle \partial_y \partial_x \sigma_{xy,m} | u_{x,n} \rangle \\
&- \langle \partial_x \sigma_{xy,m} | \partial_y u_{x,n} \rangle - \langle \partial_y \partial_x u_{x,m} | \sigma_{xy,n} \rangle.
\end{aligned} \tag{B.8}$$

Limiting (B.8) to $n = m$ and using the commutator (B.1) finally leads to

$$\begin{aligned}
\langle \partial_x \vec{X}_n | \mathbf{G} \vec{X}_n \rangle + \langle \mathbf{G} \partial_x \vec{X}_n | \vec{X}_n \rangle &= \partial_x \langle \vec{X}_n | \mathbf{G} \vec{X}_n \rangle \\
&- \rho\omega^2 \left((\partial_x h_U) u_{x,n}^2(\bar{h}) - (\partial_x h_L) u_{x,n}^2(-\bar{h}) \right) \\
&- (\partial_x h_U) u_{x,n}(\bar{h}) (\partial_y \sigma_{xy,n})(\bar{h}) \\
&+ (\partial_x h_L) u_{x,n}(-\bar{h}) (\partial_y \sigma_{xy,n})(-\bar{h}).
\end{aligned} \tag{B.9}$$

In a similar way we find

$$\begin{aligned}
\langle \mathbf{F} Z_{c,n} \vec{Y}_n | \partial_x(Z_{c,n} \vec{Y}_n) \rangle + \langle Z_{c,n} \vec{Y}_n | \mathbf{F} \partial_x(Z_{c,n} \vec{Y}_n) \rangle &= \partial_x \langle Z_{c,n} \vec{Y}_n | \mathbf{F} Z_{c,n} \vec{Y}_n \rangle \\
&+ \rho\omega^2 Z_{c,n}^2 (\partial_x h_U) u_{y,n}^2(\bar{h}) \\
&- \rho\omega^2 Z_{c,n}^2 (\partial_x h_L) u_{y,n}^2(-\bar{h}) \\
&+ ik_n Z_{c,n} (\partial_x h_U) u_{x,n}(\bar{h}) \sigma_{xx,n}(\bar{h}) \\
&- ik_n Z_{c,n} (\partial_x h_L) u_{x,n}(-\bar{h}) \sigma_{xx,n}(-\bar{h}) \\
&+ Z_{c,n}^2 (\partial_x h_U) u_{y,n}(\bar{h}) (\partial_y \sigma_{yy,n})(\bar{h}) \\
&- Z_{c,n}^2 (\partial_x h_L) u_{y,n}(-\bar{h}) (\partial_y \sigma_{yy,n})(-\bar{h})
\end{aligned} \tag{B.10}$$

and thus

$$\begin{aligned}
\mathcal{B} &= \frac{i\rho\omega^2}{2k_n} \left[(\partial_x h_U) (u_{x,n}^2(\bar{h}) + Z_{c,n}^2 u_{y,n}^2(\bar{h})) - (\partial_x h_L) (u_{x,n}^2(-\bar{h}) + Z_{c,n}^2 u_{y,n}^2(-\bar{h})) \right] \\
&- \frac{Z_{c,n}}{2} \left[(\partial_x h_U) u_{x,n}(\bar{h}) \sigma_{xx,n}(\bar{h}) - (\partial_x h_L) u_{x,n}(-\bar{h}) \sigma_{xx,n}(-\bar{h}) \right]
\end{aligned} \tag{B.11}$$

If (B.11) is inserted into (B.3) we obtain the expression for diagonal elements of \mathbf{N}_1 given in (3.40). The diagonal elements for \mathbf{N}_4 as given in (3.41) are obtained by following the same steps as outlined for \mathbf{N}_1 while starting from (3.38) instead of (3.35).

In order to find closed analytical expressions for the off-diagonal elements of \mathbf{N}_1 , it is convenient to rewrite (B.3) as

$$\begin{aligned}
2(k_m^2 - k_n^2) \mathcal{J}_n N_{1,nm} &= (k_n^2 - k_m^2) ((\partial_x h_U) u_{x,m}(\bar{h}) \sigma_{xx,n}(\bar{h}) - (\partial_x h_L) u_{x,m}(-\bar{h}) \sigma_{xx,n}(-\bar{h})) \\
&\quad + (k_n^2 - k_m^2) \left(\underbrace{\frac{\partial_x \mathcal{J}_n \delta_{nm}}{2}}_{=0 \text{ for } n \neq m} + \langle \partial_x \vec{X}_m | \vec{Y}_n \rangle - \langle \vec{X}_m | \partial_x \vec{Y}_n \rangle \right) \\
&= (k_n^2 - k_m^2) ((\partial_x h_U) u_{x,m}(\bar{h}) \sigma_{xx,n}(\bar{h}) - (\partial_x h_L) u_{x,m}(-\bar{h}) \sigma_{xx,n}(-\bar{h})) \\
&\quad + \langle \partial_x \vec{X}_m | k_n^2 \vec{Y}_n \rangle - \langle k_m^2 \partial_x \vec{X}_m | \vec{Y}_n \rangle \\
&\quad - \langle \vec{X}_m | k_n^2 \partial_x \vec{Y}_n \rangle + \langle k_m^2 \vec{X}_m | \partial_x \vec{Y}_n \rangle \\
&= (k_n^2 - k_m^2) ((\partial_x h_U) u_{x,m}(\bar{h}) \sigma_{xx,n}(\bar{h}) - (\partial_x h_L) u_{x,m}(-\bar{h}) \sigma_{xx,n}(-\bar{h})) \\
&\quad + \langle \partial_x \vec{X}_m | k_n^2 \vec{Y}_n \rangle - \langle \partial_x (k_m^2 \vec{X}_m) | \vec{Y}_n \rangle + 2k_m (\partial_x k_m) \underbrace{\langle \vec{X}_m | \vec{Y}_n \rangle}_{=0 \text{ for } n \neq m} \\
&\quad - \langle \vec{X}_m | \partial_x (k_n^2 \vec{Y}_n) \rangle + 2k_n (\partial_x k_n) \underbrace{\langle \vec{X}_m | \vec{Y}_n \rangle}_{=0 \text{ for } n \neq m} + \langle k_m^2 \vec{X}_m | \partial_x \vec{Y}_n \rangle \\
&= (k_n^2 - k_m^2) ((\partial_x h_U) u_{x,m}(\bar{h}) \sigma_{xx,n}(\bar{h}) - (\partial_x h_L) u_{x,m}(-\bar{h}) \sigma_{xx,n}(-\bar{h})) \\
&\quad - \left. \begin{aligned} &\langle \partial_x \vec{X}_m | \mathbf{GF} \vec{Y}_n \rangle + \langle \partial_x (\mathbf{FG} \vec{X}_m) | \vec{Y}_n \rangle \\ &+ \langle \vec{X}_m | \partial_x (\mathbf{GF} \vec{Y}_n) \rangle - \langle \mathbf{FG} \vec{X}_m | \partial_x \vec{Y}_n \rangle \end{aligned} \right\} = \mathcal{B}
\end{aligned} \tag{B.12}$$

By using the properties (B.4) and (B.5) of \mathbf{F} and \mathbf{G} as well as the matrix forms (3.12) and (3.13), (3.20) and the identity (3.8), it can be shown that

$$\begin{aligned}
\mathcal{B} &= \frac{ik_n}{Z_{c,n}} [(\partial_x \sigma_{xy}, m) u_{x,n} + u_{x,m} (\partial_x \sigma_{xy,n})]_{h_L}^{h_U} \\
&\quad - ik_m Z_{c,m} [(\partial_x \sigma_{yy}, m) u_{y,n} + u_{y,m} (\partial_x \sigma_{yy,n})]_{h_L}^{h_U}.
\end{aligned} \tag{B.13}$$

Considering the commutator (B.1) and the boundary conditions of traction free surfaces (B.13) translates into

$$\begin{aligned}
\mathcal{B} = & -\frac{ik_n}{Z_{c,n}}(\partial_x h_U) \left((\partial_y \sigma_{xy,m})(\bar{h})u_{x,n}(\bar{h}) + u_{x,m}(\bar{h})(\partial_y \sigma_{xy,n})(\bar{h}) \right) \\
& + \frac{ik_n}{Z_{c,n}}(\partial_x h_L) \left((\partial_y \sigma_{xy,m})(-\bar{h})u_{x,n}(-\bar{h}) + u_{x,m}(-\bar{h})(\partial_y \sigma_{xy,n})(-\bar{h}) \right) \\
& + ik_m Z_{c,m}(\partial_x h_U) \left((\partial_y \sigma_{yy,m})(\bar{h})u_{y,n}(\bar{h}) + u_{y,m}(\bar{h})(\partial_y \sigma_{yy,n})(\bar{h}) \right) \\
& - ik_m Z_{c,m}(\partial_x h_L) \left((\partial_y \sigma_{yy,m})(-\bar{h})u_{y,n}(-\bar{h}) + u_{y,m}(-\bar{h})(\partial_y \sigma_{yy,n})(-\bar{h}) \right).
\end{aligned} \tag{B.14}$$

From (3.12), (3.13), (3.20) and the identity (3.8) we find

$$\partial_y \sigma_{yy,n} = -\rho\omega^2 u_{y,n} - \frac{ik_n}{Z_{c,n}} \sigma_{xy,n} \tag{B.15}$$

and

$$\partial_y \sigma_{xy,n} = -\rho\omega^2 u_{x,n} - ik_m Z_{c,m} \sigma_{xx,n} \tag{B.16}$$

which leads to

$$\begin{aligned}
\mathcal{B} = & -2i\rho\omega^2 k_m Z_{c,m} \left((\partial_x h_U)u_{y,m}(\bar{h})u_{y,n}(\bar{h}) - (\partial_x h_L)u_{y,m}(-\bar{h})u_{y,n}(-\bar{h}) \right) \\
& + 2i\rho\omega^2 \frac{k_n}{Z_{c,n}} \left((\partial_x h_U)u_{x,m}(\bar{h})u_{x,n}(\bar{h}) - (\partial_x h_L)u_{x,m}(-\bar{h})u_{x,n}(-\bar{h}) \right) \\
& - (k_n^2 + k_m^2) \left((\partial_x h_U)u_{x,m}(\bar{h})\sigma_{xx,n}(\bar{h}) - (\partial_x h_L)u_{x,m}(-\bar{h})\sigma_{xx,n}(-\bar{h}) \right).
\end{aligned} \tag{B.17}$$

If (B.17) is inserted back into (B.12), the expressions (3.42) and (3.44) are obtained to describe the off-diagonal elements in \mathbf{N}_1 . The expressions (3.43) and (3.45) for the off-diagonal elements in \mathbf{N}_4 are obtained by performing the same calculation steps while starting from (3.38) instead of (3.35).

B.2 Cylindrical rods

For cylindrical rods the entries of matrix \mathbf{N}_1 and matrix \mathbf{N}_4 are given by (4.60) and (4.63). In order to find a closed analytical expression for these entries, the scalar products $\langle \partial_z \vec{X}_m | \vec{Y}_n \rangle$ and $\langle \partial_z \vec{Y}_m | \vec{X}_n \rangle$ have to be evaluated which correspond to a double integral over r and φ . Since the scope of this work is restricted to axially symmetric guided waves, the integration over φ is trivial and simply leads to a factor 2π . The integration in r -direction runs from the central axis of the rod $r = 0$ to its outer radius $r = R$.

The commutator between the differential and integral operator is

$$\left[\partial_z f(r, z), \int_0^R f(r, z) r dr \right] = (\partial_z R) R f(R, z). \tag{B.18}$$

Combining this commutator with the biorthogonality relation (3.19) expressed in cylindrical coordinates yields

$$(\partial_z \mathcal{J}_n) \delta_{nm} = \langle \partial_z \vec{X}_n | \vec{Y}_m \rangle + \langle \vec{X}_n | \partial_z \vec{Y}_m \rangle + 2\pi (\partial_z R) R \vec{X}_n(R) \vec{Y}_m(R). \quad (\text{B.19})$$

If the boundary condition of traction free surfaces $\sigma_{rz,n}(R) = 0$ is taken into account and steps similar to those outlined in (B.3) are performed, we obtain

$$\begin{aligned} -\mathcal{J}_n N_{1,nm} = & \frac{1}{2} (\partial_z \mathcal{J}_n) \delta_{nm} + \frac{1}{2} \frac{\partial_z Z_{c,n}}{Z_{c,n}} \mathcal{J}_n \delta_{nm} + \pi (\partial_z R) R u_{z,m}(R) \sigma_{zz,n}(R) \\ & + \frac{1}{2Z_{c,n}} \left(\underbrace{\frac{1}{ik_n} \langle \partial_z \vec{X}_m | \mathbf{G} \vec{X}_n \rangle - \frac{1}{ik_m} \langle \mathbf{F} Z_{c,m} \vec{Y}_m | \partial_z (Z_{c,n} \vec{Y}_n) \rangle}_{=\mathcal{B}} \right) \end{aligned} \quad (\text{B.20})$$

Similar to (B.4) and (B.5) the matrix operators \mathbf{F} and \mathbf{G} for cylindrical rods have the properties

$$\langle \mathbf{F} \vec{\mathcal{L}}_1 | \vec{\mathcal{L}}_2 \rangle = \langle \vec{\mathcal{L}}_1 | \mathbf{F} \vec{\mathcal{L}}_2 \rangle + 2\pi [f_1 r (z_{11} z_{22} - z_{12} z_{21}) + f_2 (z_{12} \partial_z (r z_{22}) - (\partial_z (r z_{12})) z_{22})]_0^R \quad (\text{B.21})$$

$$\langle \vec{\mathcal{L}}_1 | \mathbf{G} \vec{\mathcal{L}}_2 \rangle = \langle \mathbf{G} \vec{\mathcal{L}}_1 | \vec{\mathcal{L}}_2 \rangle - 2\pi [r (z_{12} z_{21} - z_{11} z_{22})]_0^R. \quad (\text{B.22})$$

If \mathcal{B} is rewritten as in (B.6), the properties (B.21) and (B.22) and the identity (4.42) can be used to obtain

$$\begin{aligned} \mathcal{B} = & \frac{1}{2ik_n} \left(\langle \partial_z \vec{X}_m | \mathbf{G} \vec{X}_n \rangle + \langle \mathbf{G} \partial_z \vec{X}_m | \vec{X}_n \rangle \right) \\ & - \frac{1}{2ik_m} \left(\langle \mathbf{F} Z_{c,m} \vec{Y}_m | \partial_z (Z_{c,n} \vec{Y}_n) \rangle + \langle Z_{c,m} \vec{Y}_m | \mathbf{F} \partial_z (Z_{c,n} \vec{Y}_n) \rangle \right) \\ & - \frac{\pi}{ik_n} R u_{z,n}(R) \partial_z \sigma_{rz,m}(R) - \frac{\pi}{ik_m} R Z_{c,m} u_{r,m}(R) \partial_z (Z_{c,n} \sigma_{rr,n}(R)). \end{aligned} \quad (\text{B.23})$$

Using the commutator

$$\left[\partial_z f(r, z), \int_0^R f(r, z) dr \right] = (\partial_z R) f(R, z) \quad (\text{B.24})$$

it can be shown that

$$[r u_{z,n} \partial_z \sigma_{rz,m}]_0^R = -(\partial_z R) R u_{z,n}(R) (\partial_r \sigma_{rz,m})(R) \quad (\text{B.25})$$

and

$$[r Z_{c,m} u_{r,n} \partial_z (Z_{c,n} \sigma_{rr,n})]_0^R = -(\partial_z R) R Z_{c,m} u_{r,m}(R) Z_{c,n} (\partial_r \sigma_{rr,n})(R) \quad (\text{B.26})$$

and thus

$$\begin{aligned}
\mathcal{B} &= \frac{1}{2ik_n} \left(\langle \partial_z \vec{X}_m | \mathbf{G} \vec{X}_n \rangle + \langle \mathbf{G} \partial_z \vec{X}_m | \vec{X}_n \rangle \right) \\
&\quad - \frac{1}{2ik_m} \left(\langle \mathbf{F} Z_{c,m} \vec{Y}_m | \partial_z (Z_{c,n} \vec{Y}_n) \rangle + \langle Z_{c,m} \vec{Y}_m | \mathbf{F} \partial_z (Z_{c,n} \vec{Y}_n) \rangle \right) \\
&\quad + \frac{\pi}{ik_n} (\partial_z R) R u_{z,n}(R) (\partial_r \sigma_{rz,m})(R) + \frac{\pi}{ik_m} (\partial_z R) R Z_{c,m} u_{r,m}(R) Z_{c,n} (\partial_r \sigma_{rr,n})(R).
\end{aligned} \tag{B.27}$$

With \mathbf{G} applied as given in (4.50), we obtain

$$\begin{aligned}
\langle \partial_z \vec{X}_m | \mathbf{G} \vec{X}_n \rangle + \langle \mathbf{G} \partial_z \vec{X}_m | \vec{X}_n \rangle &= 2\rho\omega^2 \langle \partial_z u_{z,m} | u_{z,n} \rangle + \frac{2}{\mu} \langle \partial_z \sigma_{rz,m} | \sigma_{rz,n} \rangle \\
&\quad + \left\langle \partial_z u_{z,m} \left| \frac{1}{r} \partial_r (\sigma_{rz,n}) \right. \right\rangle + \left\langle \frac{1}{r} \partial_r (r \partial_z \sigma_{rz,m}) \left| u_{z,n} \right. \right\rangle \\
&\quad - \langle \partial_z \sigma_{rz,m} | \partial_r u_{z,n} \rangle - \langle \partial_r \partial_z u_{z,m} | \sigma_{rz,n} \rangle.
\end{aligned} \tag{B.28}$$

Limiting (B.28) to $n = m$ and using the commutators (B.18) and (B.24) subsequently leads to

$$\begin{aligned}
\langle \partial_z \vec{X}_n | \mathbf{G} \vec{X}_n \rangle + \langle \mathbf{G} \partial_z \vec{X}_n | \vec{X}_n \rangle &= \partial_z \langle \vec{X}_n | \mathbf{G} \vec{X}_n \rangle \\
&\quad - 2\pi\rho\omega^2 (\partial_z R) R u_{z,n}^2(R) \\
&\quad - 2\pi (\partial_z R) R u_{z,n}(R) (\partial_z \sigma_{rz,n})(R).
\end{aligned} \tag{B.29}$$

A similar calculation yields

$$\begin{aligned}
\langle \mathbf{F} Z_{c,n} \vec{Y}_n | \partial_z (Z_{c,n} \vec{Y}_n) \rangle + \langle Z_{c,n} \vec{Y}_n | \mathbf{F} \partial_z (Z_{c,n} \vec{Y}_n) \rangle &= \partial_z \langle Z_{c,n} \vec{Y}_n | \mathbf{F} Z_{c,n} \vec{Y}_n \rangle \\
&\quad + 2\pi\rho\omega^2 Z_{c,n}^2 (\partial_z R) R u_{r,n}^2(R) \\
&\quad + 2\pi ik_n (\partial_z R) R u_{z,n}(R) \sigma_{zz,n}(R) \\
&\quad + 2\pi Z_{c,n}^2 (\partial_z R) R u_{r,n}(R) (\partial_r \sigma_{rr,n})(R) \\
&\quad + 4\pi\mu Z_{c,n}^2 (\partial_z R) u_{r,n}(R) (\partial_r u_{r,n})(R) \\
&\quad - 4\pi\mu Z_{c,n}^2 \frac{\partial_z R}{R} u_{r,n}^2(R).
\end{aligned} \tag{B.30}$$

If (B.29) and (B.30) are inserted into (B.27), \mathcal{B} can be written as

$$\begin{aligned}
\mathcal{B} &= \frac{i\pi}{k_n} (\partial_z R) R \rho\omega^2 (u_{z,n}^2(R) + Z_{c,n}^2 u_{r,n}^2(R)) - \pi (\partial_z R) R Z_{c,n} u_{z,n}(R) \sigma_{zz,n}(R) \\
&\quad + 2\mu \frac{i\pi}{k_n} (\partial_z R) R Z_{c,n}^2 u_{r,n}(R) \left(\partial_r \frac{u_{r,n}}{r} \right) (R).
\end{aligned} \tag{B.31}$$

With the identity (4.42) and $\sigma_{rr,n}(R) = 0$ as well as $f_1 = \lambda/(\lambda + 2\mu)$ and $f_2 = 4\mu(\lambda + \mu)/(\lambda + 2\mu)$, we can rewrite

$$\begin{aligned}
u_{r,n}(R) \left(\partial_r \frac{u_{r,n}}{r} \right) (R) &= u_{r,n}(R) \left(-\frac{u_{r,n}(R)}{R^2} + \frac{1}{R} (\partial_r u_{r,n})(R) \right) \\
&= -\frac{u_{r,n}(R)}{R} \left(\frac{f_1}{f_2} \sigma_{zz,n}(R) + \left(2 - \frac{2\mu}{f_2} \right) \frac{u_{r,n}(R)}{R} \right) \\
&= \frac{-1}{4\mu(\lambda + \mu)} \frac{1}{R} \left(\lambda u_{r,n}(R) \sigma_{rr,n}(R) + \frac{2\mu}{R} (3\lambda + 2\mu) u_{r,n}^2(R) \right).
\end{aligned} \tag{B.32}$$

From (B.32), (B.31) and (B.20) the expression for diagonal elements of \mathbf{N}_1 given in (4.64) is obtained. The diagonal elements for \mathbf{N}_4 as given in (4.65) are obtained by following the same steps as outlined for \mathbf{N}_1 while starting from (4.63) instead of (4.60).

In order to find closed analytical expressions for the off-diagonal elements of \mathbf{N}_1 , (B.20) is rewritten as

$$\begin{aligned}
2(k_m^2 - k_n^2) \mathcal{J}_n N_{1,nm} &= \underbrace{(\partial_z \mathcal{J}_n) \delta_{nm}}_{=0} + 2(k_n^2 - k_m^2) \pi (\partial_z R) R u_{z,m}(R) \sigma_{zz,n}(R) \\
&\quad + \underbrace{(k_n^2 - k_m^2) \left(\langle \partial_z \vec{X}_m | \vec{Y}_n \rangle - \langle \vec{X}_m | \partial_z \vec{Y}_n \rangle \right)}_{=\mathcal{B}}.
\end{aligned} \tag{B.33}$$

Taking the same steps as outlined in (B.12), it can be shown that

$$\mathcal{B} = \langle \vec{X}_m | \partial_z (\mathbf{G} \mathbf{F} \vec{Y}_n) \rangle - \langle \mathbf{F} \mathbf{G} \vec{X}_m | \partial_z \vec{Y}_n \rangle - \langle \partial_z \vec{X}_m | \mathbf{G} \mathbf{F} \vec{Y}_n \rangle + \langle \partial_z (\mathbf{F} \mathbf{G} \vec{X}_m) | \vec{Y}_n \rangle \tag{B.34}$$

By using the properties (B.21) and (B.22) of \mathbf{F} and \mathbf{G} as well as the matrix forms (4.49) and (4.50), (3.20) and the identity (4.42), the expression (B.34) can be transformed into

$$\begin{aligned}
\mathcal{B} &= 2\pi \frac{ik_n}{Z_{c,n}} [r(u_{z,n}(\partial_z \sigma_{rz,m}) + (\partial_z \sigma_{rz,n})u_{z,m})]_0^R \\
&\quad - 2\pi ik_m Z_{c,m} [r(u_{r,n}(\partial_z \sigma_{rr,m}) + (\partial_z \sigma_{rr,n})u_{r,m})]_0^R.
\end{aligned} \tag{B.35}$$

Considering the commutators (B.18) and (B.24) as well as the boundary conditions of traction free surfaces this translates into

$$\begin{aligned}
\mathcal{B} &= 2\pi ik_m Z_{c,m} (\partial_z R) R \left(u_{r,n}(R) (\partial_r \sigma_{rr,m})(R) + (\partial_r \sigma_{rr,n})(R) u_{r,m}(R) \right) \\
&\quad - 2\pi \frac{ik_n}{Z_{c,n}} (\partial_z R) R \left(u_{z,n}(R) (\partial_r \sigma_{rz,m})(R) + (\partial_r \sigma_{rz,n})(R) u_{z,m}(R) \right).
\end{aligned} \tag{B.36}$$

From (4.49), (4.50), (3.20) and the identity (4.42) we find

$$\begin{aligned} \mathcal{B} = & 2\pi(\partial_z R)R \left\{ 2i\rho\omega^2 \left(\frac{k_n u_{z,n}(R) u_{z,m}(R)}{Z_{c,n}} - k_m Z_{c,m} u_{r,n}(R) u_{r,m}(R) \right) \right. \\ & - k_n^2 \sigma_{zz,n}(R) u_{z,m}(R) - k_n k_m \frac{Z_{c,m}}{Z_{c,n}} u_{z,n}(R) \sigma_{zz,m}(R) \\ & \left. - ik_m Z_{c,m} 2\mu \left(u_{r,n}(R) \left(\partial_r \frac{u_{r,m}}{r} \right) (R) \left(\partial_r \frac{u_{r,n}}{r} \right) (R) u_{r,m}(R) \right) \right\}. \end{aligned} \quad (\text{B.37})$$

If the procedure shown in (B.32) is used to eliminate differentiation in r -direction and (B.37) is subsequently inserted back into (B.33), this results in the expression for the off-diagonal elements in \mathbf{N}_1 given in (4.66). The expression (4.67) for the off-diagonal elements in \mathbf{N}_4 is obtained by performing the same calculation steps while starting from (4.63) instead of (4.60).

B.3 Hollow Cylinders

For hollow cylinders the entries of matrix \mathbf{N}_1 and matrix \mathbf{N}_4 are given by (4.78) and (4.81). The closed analytical expression for these entries are found by evaluating the double integral over r and φ in the scalar products $\langle \partial_z \vec{X}_m | \vec{Y}_n \rangle$ and $\langle \partial_z \vec{Y}_m | \vec{X}_n \rangle$. Due to the restriction to axially symmetric guided waves, the integration over φ only accounts for a factor of 2π . The integration in r -direction runs from the inner radius $r = R_I$ to its outer radius $r = R_O$.

The commutator between the differential and integral operator is

$$\left[\partial_z f(r, z), \int_{R_I}^{R_O} f(r, z) r dr \right] = (\partial_z R_O) R_O f(R_O, z) - (\partial_z R_I) R_I f(R_I, z). \quad (\text{B.38})$$

Viewing the case of cylindrical rods, we have already established that a second commutator (B.24) will be required at a later stage in the calculations. For hollow cylinders this second commutator takes the form

$$\left[\partial_z f(r, z), \int_{R_I}^{R_O} f(r, z) dr \right] = (\partial_z R_O) f(R_O, z) - (\partial_z R_I) f(R_I, z) \quad (\text{B.39})$$

Combining the first commutator (B.38) with the biorthogonality relation (3.19) expressed in cylindrical coordinates yields

$$\begin{aligned} (\partial_z \mathcal{J}_n) \delta_{nm} = & \langle \partial_z \vec{X}_n | \vec{Y}_m \rangle + \langle \vec{X}_n | \partial_z \vec{Y}_m \rangle \\ & + 2\pi \left((\partial_z R_O) R_O \vec{X}_n(R_O) \vec{Y}_m(R_O) - (\partial_z R_I) R_I \vec{X}_n(R_I) \vec{Y}_m(R_I) \right). \end{aligned} \quad (\text{B.40})$$

If the boundary conditions of traction free surfaces $\sigma_{rz,n}(R_O) = 0$ and $\sigma_{rz,n}(R_I) = 0$ are taken into account, we obtain

$$\begin{aligned}
-\mathcal{I}_n N_{1,nm} &= \frac{1}{2}(\partial_z \mathcal{I}_n) \delta_{nm} + \frac{1}{2} \frac{\partial_z Z_{c,n}}{Z_{c,n}} \mathcal{I}_n \delta_{nm} \\
&+ \pi \left((\partial_z R_O) R_O u_{z,m}(R_O) \sigma_{zz,n}(R_O) - (\partial_z R_I) R_I u_{z,m}(R_I) \sigma_{zz,n}(R_I) \right) \\
&+ \frac{1}{2Z_{c,n}} \underbrace{\left(\frac{1}{ik_n} \langle \partial_z \vec{X}_m | \mathbf{G} \vec{X}_n \rangle - \frac{1}{ik_m} \langle \mathbf{F} Z_{c,m} \vec{Y}_m | \partial_z (Z_{c,n} \vec{Y}_n) \rangle \right)}_{=\mathcal{B}}
\end{aligned} \tag{B.41}$$

by repeating steps similar to those outlined in (B.3) as we did for the case of cylindrical rods. For hollow cylinders, the properties of the matrix operators \mathbf{F} and \mathbf{G} for cylindrical rods (B.21) and (B.22) are modified into

$$\begin{aligned}
\langle \mathbf{F} \mathcal{Z}_1 | \mathcal{Z}_2 \rangle &= \langle \mathcal{Z}_1 | \mathbf{F} \mathcal{Z}_2 \rangle + 2\pi f_1 [r(z_{11}z_{22} - z_{12}z_{21})]_{R_I}^{R_O} \\
&+ 2\pi f_2 [z_{12}\partial_z(rz_{22}) - (\partial_z(rz_{12}))z_{22}]_{R_I}^{R_O}
\end{aligned} \tag{B.42}$$

and

$$\langle \mathcal{Z}_1 | \mathbf{G} \mathcal{Z}_2 \rangle = \langle \mathbf{G} \mathcal{Z}_1 | \mathcal{Z}_2 \rangle - 2\pi [r(z_{12}z_{21} - z_{11}z_{22})]_{R_I}^{R_O}. \tag{B.43}$$

We can now use the properties (B.42) and (B.43) and the identity (4.42) to rewrite \mathcal{B} as has been done in (B.6) and obtain

$$\begin{aligned}
\mathcal{B} &= \frac{1}{2ik_n} \left(\langle \partial_z \vec{X}_m | \mathbf{G} \vec{X}_n \rangle + \langle \mathbf{G} \partial_z \vec{X}_m | \vec{X}_n \rangle \right) \\
&- \frac{1}{2ik_m} \left(\langle \mathbf{F} Z_{c,m} \vec{Y}_m | \partial_z (Z_{c,n} \vec{Y}_n) \rangle + \langle Z_{c,m} \vec{Y}_m | \mathbf{F} \partial_z (Z_{c,n} \vec{Y}_n) \rangle \right) \\
&- \frac{\pi}{ik_m} \left(R_O Z_{c,m} u_{r,m}(R_O) \partial_z (Z_{c,n} \sigma_{rr,n}(R_O)) - R_I Z_{c,m} u_{r,m}(R_I) \partial_z (Z_{c,n} \sigma_{rr,n}(R_I)) \right) \\
&- \frac{\pi}{ik_n} \left(R_O u_{z,n}(R_O) \partial_z \sigma_{rz,m}(R_O) - R_I u_{z,n}(R_I) \partial_z \sigma_{rz,m}(R_I) \right).
\end{aligned} \tag{B.44}$$

Using the commutators (B.38) and (B.39), we find

$$\begin{aligned}
[r u_{z,n} \partial_z \sigma_{rz,m}]_{R_I}^{R_O} &= -(\partial_z R_O) R_O u_{z,n}(R_O) (\partial_r \sigma_{rz,m})(R_O) \\
&+ (\partial_z R_I) R_I u_{z,n}(R_I) (\partial_r \sigma_{rz,m})(R_I)
\end{aligned} \tag{B.45}$$

and

$$\begin{aligned}
[r Z_{c,m} u_{r,n} \partial_z (Z_{c,n} \sigma_{rr,n})]_{R_I}^{R_O} &= -(\partial_z R_O) R_O Z_{c,m} u_{r,m}(R_O) Z_{c,n} (\partial_r \sigma_{rr,n})(R_O) \\
&+ (\partial_z R_I) R_I Z_{c,m} u_{r,m}(R_I) Z_{c,n} (\partial_r \sigma_{rr,n})(R_I)
\end{aligned} \tag{B.46}$$

and subsequently

$$\begin{aligned}
\mathcal{B} = & \frac{1}{2ik_n} \left(\langle \partial_z \vec{X}_m | \mathbf{G} \vec{X}_n \rangle + \langle \mathbf{G} \partial_z \vec{X}_m | \vec{X}_n \rangle \right) \\
& - \frac{1}{2ik_m} \left(\langle \mathbf{F} Z_{c,m} \vec{Y}_m | \partial_z (Z_{c,n} \vec{Y}_n) \rangle + \langle Z_{c,m} \vec{Y}_m | \mathbf{F} \partial_z (Z_{c,n} \vec{Y}_n) \rangle \right) \\
& + \frac{\pi}{ik_n} \left((\partial_z R_O) R_O u_{z,n}(R_O) (\partial_r \sigma_{rz,m})(R_O) - (\partial_z R_I) R_I u_{z,n}(R_I) (\partial_r \sigma_{rz,m})(R_I) \right) \\
& + \frac{\pi}{ik_m} (\partial_z R_O) R_O Z_{c,m} u_{r,m}(R_O) Z_{c,n} (\partial_r \sigma_{rr,n})(R_O) \\
& - \frac{\pi}{ik_m} (\partial_z R_I) R_I Z_{c,m} u_{r,m}(R_I) Z_{c,n} (\partial_r \sigma_{rr,n})(R_I).
\end{aligned} \tag{B.47}$$

The expression (B.28) remains valid for the case of hollow cylinders. If (B.28) is limited to $n = m$ and the commutators (B.38) and (B.39) are used, we find

$$\begin{aligned}
\langle \partial_z \vec{X}_n | \mathbf{G} \vec{X}_n \rangle + \langle \mathbf{G} \partial_z \vec{X}_n | \vec{X}_n \rangle = & \partial_z \langle \vec{X}_n | \mathbf{G} \vec{X}_n \rangle \\
& - 2\pi \rho \omega^2 \left((\partial_z R_O) R_O u_{z,n}^2(R_O) - (\partial_z R_I) R_I u_{z,n}^2(R_I) \right) \\
& - 2\pi (\partial_z R_O) R_O u_{z,n}(R_O) (\partial_z \sigma_{rz,n})(R_O) \\
& + 2\pi (\partial_z R_I) R_I u_{z,n}(R_I) (\partial_z \sigma_{rz,n})(R_I).
\end{aligned} \tag{B.48}$$

and with a similar calculation

$$\begin{aligned}
\langle \mathbf{F} Z_{c,n} \vec{Y}_n | \partial_z (Z_{c,n} \vec{Y}_n) \rangle + \langle Z_{c,n} \vec{Y}_n | \mathbf{F} \partial_z (Z_{c,n} \vec{Y}_n) \rangle = & \partial_z \langle Z_{c,n} \vec{Y}_n | \mathbf{F} Z_{c,n} \vec{Y}_n \rangle \\
& + 2\pi \rho \omega^2 Z_{c,n}^2 \left((\partial_z R_O) R_O u_{r,n}^2(R_O) - (\partial_z R_I) R_I u_{r,n}^2(R_I) \right) \\
& + 2\pi ik_n \left((\partial_z R_O) R_O u_{z,n}(R_O) \sigma_{zz,n}(R_O) - (\partial_z R_I) R_I u_{z,n}(R_I) \sigma_{zz,n}(R_I) \right) \\
+ 2\pi Z_{c,n}^2 \left((\partial_z R_O) R_O u_{r,n}(R_O) (\partial_r \sigma_{rr,n})(R_O) - (\partial_z R_I) R_I u_{r,n}(R_I) (\partial_r \sigma_{rr,n})(R_I) \right) & \\
+ 4\pi \mu Z_{c,n}^2 \left((\partial_z R_O) u_{r,n}(R_O) (\partial_r u_{r,n})(R_O) - (\partial_z R_I) u_{r,n}(R_I) (\partial_r u_{r,n})(R_I) \right) & \\
- 4\pi \mu Z_{c,n}^2 \left(\frac{\partial_z R_O}{R_O} u_{r,n}^2(R_O) - \frac{\partial_z R_I}{R_I} u_{r,n}^2(R_I) \right). &
\end{aligned} \tag{B.49}$$

If (B.48) and (B.49) are inserted into (B.47), \mathcal{B} can be written as

$$\begin{aligned}
\mathcal{B} = & -\pi \left((\partial_z R_O) R_O Z_{c,n} u_{z,n}(R_O) \sigma_{zz,n}(R_O) - (\partial_z R_I) R_I Z_{c,n} u_{z,n}(R_I) \sigma_{zz,n}(R_I) \right) \\
& + 2\mu \frac{i\pi}{k_n} (\partial_z R_O) R_O Z_{c,n}^2 u_{r,n}(R_O) \left(\partial_r \frac{u_{r,n}}{r} \right) (R_O) \\
& - 2\mu \frac{i\pi}{k_n} (\partial_z R_I) R_I Z_{c,n}^2 u_{r,n}(R_I) \left(\partial_r \frac{u_{r,n}}{r} \right) (R_I) \\
& + \frac{i\pi}{k_n} (\partial_z R_O) R_O \rho \omega^2 \left(u_{z,n}^2(R_O) + Z_{c,n}^2 u_{r,n}^2(R_O) \right) \\
& - \frac{i\pi}{k_n} (\partial_z R_I) R_I \rho \omega^2 \left(u_{z,n}^2(R_I) + Z_{c,n}^2 u_{r,n}^2(R_I) \right).
\end{aligned} \tag{B.50}$$

With the identity (4.42) and the boundary conditions $\sigma_{rr,n}(R_O) = 0$ and $\sigma_{rr,n}(R_I) = 0$ as well as $f_1 = \lambda/(\lambda + 2\mu)$ and $f_2 = 4\mu(\lambda + \mu)/(\lambda + 2\mu)$, we can rewrite

$$u_{r,n}(R_O) \left(\partial_r \frac{u_{r,n}}{r} \right) (R_O) = \frac{-1}{4\mu(\lambda + \mu)} \left(\lambda \frac{u_{r,n}(R_O) \sigma_{rr,n}(R_O)}{R_O} + 2\mu(3\lambda + 2\mu) \frac{u_{r,n}^2(R_O)}{R_O^2} \right) \tag{B.51}$$

and

$$u_{r,n}(R_I) \left(\partial_r \frac{u_{r,n}}{r} \right) (R_I) = \frac{-1}{4\mu(\lambda + \mu)} \left(\lambda \frac{u_{r,n}(R_I) \sigma_{rr,n}(R_I)}{R_I} + 2\mu(3\lambda + 2\mu) \frac{u_{r,n}^2(R_I)}{R_I^2} \right) \tag{B.52}$$

using a similar procedure as in (B.32).

If only the special case of constant inner radius R_I and thus $\partial_z R_I = 0$ is viewed, the expression for diagonal elements of \mathbf{N}_1 given in (4.82) can be obtained from (B.51), (B.50) and (B.41). The diagonal elements for \mathbf{N}_4 as given in (4.83) are obtained by following the same steps as outlined for \mathbf{N}_1 while starting from (4.81) instead of (4.78).

In order to find closed analytical expressions for the off-diagonal elements of \mathbf{N}_1 , (B.41) is rewritten as

$$\begin{aligned}
2(k_m^2 - k_n^2) \mathcal{J}_n N_{1,nm} = & \underbrace{(\partial_z \mathcal{J}_n) \delta_{nm}}_{=0} + \underbrace{(k_n^2 - k_m^2) \left(\langle \partial_z \vec{X}_m | \vec{Y}_n \rangle - \langle \vec{X}_m | \partial_z \vec{Y}_n \rangle \right)}_{=\mathcal{B}} \\
& + 2(k_n^2 - k_m^2) \pi (\partial_z R_O) R_O u_{z,m}(R_O) \sigma_{zz,n}(R_O) \\
& - 2(k_n^2 - k_m^2) \pi (\partial_z R_I) R_I u_{z,m}(R_I) \sigma_{zz,n}(R_I).
\end{aligned} \tag{B.53}$$

The expression given in (B.34) for \mathcal{B} still holds for the case of hollow cylinders. By using the properties (B.42) and (B.43) of \mathbf{F} and \mathbf{G} as well as the matrix forms (4.49) and (4.50), (3.20) and the identity (4.42), this expression can be transformed into

$$\begin{aligned}
\mathcal{B} = & 2\pi \frac{ik_n}{Z_{c,n}} \left[r(u_{z,n}(\partial_z \sigma_{rz,m}) + (\partial_z \sigma_{rz,n}) u_{z,m}) \right]_{R_I}^{R_O} \\
& - 2\pi ik_m Z_{c,m} \left[r(u_{r,n}(\partial_z \sigma_{rr,m}) + (\partial_z \sigma_{rr,n}) u_{r,m}) \right]_{R_I}^{R_O}.
\end{aligned} \tag{B.54}$$

Considering the commutators (B.38) and (B.39) as well as the boundary conditions of traction free surfaces (B.54) translates into

$$\begin{aligned}
\mathcal{B} = & 2\pi i k_m Z_{c,m} (\partial_z R_O) R_O \left(u_{r,n}(R_O) (\partial_r \sigma_{rr,m})(R_O) + (\partial_r \sigma_{rr,n})(R_O) u_{r,m}(R_O) \right) \\
& - 2\pi i k_m Z_{c,m} (\partial_z R_I) R_I \left(u_{r,n}(R_I) (\partial_r \sigma_{rr,m})(R_I) + (\partial_r \sigma_{rr,n})(R_I) u_{r,m}(R_I) \right) \\
& - 2\pi \frac{i k_n}{Z_{c,n}} (\partial_z R_O) R_O \left(u_{z,n}(R_O) (\partial_r \sigma_{rz,m})(R_O) + (\partial_r \sigma_{rz,n})(R_O) u_{z,m}(R_O) \right) \\
& + 2\pi \frac{i k_n}{Z_{c,n}} (\partial_z R_I) R_I \left(u_{z,n}(R_I) (\partial_r \sigma_{rz,m})(R_I) + (\partial_r \sigma_{rz,n})(R_I) u_{z,m}(R_I) \right).
\end{aligned} \tag{B.55}$$

Using (4.49), (4.50), (3.20) and the identity (4.42), \mathcal{B} can finally be expressed as

$$\begin{aligned}
\mathcal{B} = & 2\pi (\partial_z R_O) R_O \left\{ 2i\rho\omega^2 \left(\frac{k_n u_{z,n}(R_O) u_{z,m}(R_O)}{Z_{c,n}} - k_m Z_{c,m} u_{r,n}(R_O) u_{r,m}(R_O) \right) \right. \\
& - k_n^2 \sigma_{zz,n}(R_O) u_{z,m}(R_O) - k_n k_m \frac{Z_{c,m}}{Z_{c,n}} u_{z,n}(R_O) \sigma_{zz,m}(R_O) \\
& \left. - i k_m Z_{c,m} 2\mu \left(u_{r,n}(R_O) \left(\partial_r \frac{u_{r,m}}{r} \right) (R_O) \left(\partial_r \frac{u_{r,n}}{r} \right) (R_O) u_{r,m}(R_O) \right) \right\} \\
& - 2\pi (\partial_z R_I) R_I \left\{ 2i\rho\omega^2 \left(\frac{k_n u_{z,n}(R_I) u_{z,m}(R_I)}{Z_{c,n}} - k_m Z_{c,m} u_{r,n}(R_I) u_{r,m}(R_I) \right) \right. \\
& - k_n^2 \sigma_{zz,n}(R_I) u_{z,m}(R_I) - k_n k_m \frac{Z_{c,m}}{Z_{c,n}} u_{z,n}(R_I) \sigma_{zz,m}(R_I) \\
& \left. - i k_m Z_{c,m} 2\mu \left(u_{r,n}(R_I) \left(\partial_r \frac{u_{r,m}}{r} \right) (R_I) \left(\partial_r \frac{u_{r,n}}{r} \right) (R_I) u_{r,m}(R_I) \right) \right\}.
\end{aligned} \tag{B.56}$$

If the differentiation in r -direction is eliminated as shown in (B.51) and (B.52) and (B.56) is subsequently inserted back into (B.53), the special case of constant inner radius R_I results in the expression for the off-diagonal elements in \mathbf{N}_1 given in (4.84). The expression (4.85) for the off-diagonal elements in \mathbf{N}_4 is obtained by performing the same calculation while starting from (4.81) instead of (4.78).

Appendix C

Analytical expressions for Q_1 and Q_2

Using the shortened notation

$$\tilde{A}_1 = k^2 - \beta^2 \quad (C.1)$$

$$\tilde{A}_2 = -4k^2\alpha \quad (C.2)$$

$$B_{J\alpha} = A_1 R_O J_0(\alpha R_O) + 2\alpha J_1(\alpha R_O) \quad (C.3)$$

$$B_{Y\alpha} = A_1 R_O Y_0(\alpha R_O) + 2\alpha Y_1(\alpha R_O) \quad (C.4)$$

$$B_{J\beta} = \beta R_O J_0(\beta R_O) - J_1(\beta R_O) \quad (C.5)$$

$$B_{Y\beta} = \beta R_O Y_0(\beta R_O) - Y_1(\beta R_O) \quad (C.6)$$

$$C_{J\beta Y\beta} = J_1(\beta R_O) Y_1(\beta R_I) - Y_1(\beta R_O) J_1(\beta R_I) \quad (C.7)$$

$$C_{Y\beta J\alpha} = Y_1(\beta R_O) J_1(\alpha R_I) - J_1(\alpha R_O) Y_1(\beta R_I) \quad (C.8)$$

$$C_{J\alpha J\beta} = J_1(\alpha R_O) J_1(\beta R_I) - J_1(\beta R_O) J_1(\alpha R_I) \quad (C.9)$$

$$C_{Y\beta Y\alpha} = Y_1(\beta R_O) Y_1(\alpha R_I) - Y_1(\alpha R_O) Y_1(\beta R_I) \quad (C.10)$$

$$C_{Y\alpha J\beta} = Y_1(\alpha R_O) J_1(\beta R_I) - J_1(\beta R_O) Y_1(\alpha R_I) \quad (C.11)$$

$$C_{J\alpha Y\alpha} = J_1(\alpha R_O) Y_1(\alpha R_I) - Y_1(\alpha R_O) J_1(\alpha R_I), \quad (C.12)$$

the terms Q_1 and Q_2 used in (4.69)-(4.72) can be expressed as

$$Q_1 = -\frac{\tilde{A}_1 B_{J\alpha} C_{J\beta Y\beta} + \tilde{A}_2 B_{J\beta} C_{Y\beta J\alpha} + \tilde{A}_2 B_{Y\beta} C_{J\alpha J\beta}}{\tilde{A}_1 B_{Y\alpha} C_{J\beta Y\beta} + \tilde{A}_2 B_{J\beta} C_{Y\beta Y\alpha} + \tilde{A}_2 B_{Y\beta} C_{Y\alpha J\beta}} \quad (C.13)$$

and

$$Q_2 = \frac{\tilde{A}_1 B_{J\alpha} C_{Y\alpha J\beta} - \tilde{A}_1 B_{Y\alpha} C_{J\alpha J\beta} + \tilde{A}_2 B_{J\beta} C_{J\alpha Y\alpha}}{\tilde{A}_1 B_{J\alpha} C_{Y\beta Y\alpha} - \tilde{A}_1 B_{Y\alpha} C_{Y\beta J\alpha} - \tilde{A}_2 B_{Y\beta} C_{J\alpha Y\alpha}}. \quad (C.14)$$

Nomenclature

π	Ratio of a circle's circumference to its diameter
e	Euler's number
i	Imaginary unit
$\mathbb{1}$	Identity matrix
δ_{nm}	Kronecker's delta
\int	Integral
div	Divergence operator
grad	Gradient operator
∂_j	Derivative with respect to a spatial coordinate
∂_t	Derivative with respect to time
\sum	Sum
$\vec{\nabla}$	Nabla operator
r, φ, z	Cylindrical coordinates
x, y, z	Cartesian coordinates
t	Time
Δf	Discretization step size for frequencies
Δt	Discretization step in time dependent simulations
Δx	Discretization step size in x -direction
Δz	Discretization step size in z -direction
λ, μ	Lamé constants
\mathbf{C}	Elastic tensor

ν	Poisson ratio
ρ	Material density
ϵ	Strain tensor
ϵ_{ij}	Elements of the strain tensor
σ	Stress tensor
σ_{ij}	Elements of the stress tensor
cosh	Hyperbolic cosine
sinh	Hyperbolic sine
tanh	Hyperbolic tangent
\hat{H}_n, \tilde{H}_n	Functions mixing first and second kind Bessel functions of n th order
Q_1, Q_2	Weight between Bessel functions of first and second kind in the implementation for hollow cylinders determined from boundary conditions
J_n	Bessel functions of first kind and n th order
Y_n	Bessel functions of second kind and n th order
f, g	Arbitrary functions
f_1, f_2, γ	Functions of the Lamé constants
h	Thickness of a plate
h_L	Lower surface of a plate
h_U	Upper surface of a plate
R	Radius of a cylindrical rod
R_I	Inner radius of a hollow cylinder
R_O	Outer radius of a hollow cylinder
$\bar{\alpha}, \bar{\beta}, \alpha, \beta$	Modified wavenumbers
c_L	Phase velocity of longitudinal waves in an isotropic infinite medium
c_T	Phase velocity of shear waves in an isotropic infinite medium
k	Wave number
k_L	Wave number of the longitudinal wave in an infinite linear elastic medium

k_T	Wave number of the transverse wave in an infinite linear elastic medium
\vec{u}	Displacement vector
u_j	Elements of the displacement vector
ω	Radial frequency
f	Frequency
Φ, \vec{H}	Scalar and vector potential in a Helmholtz decomposition
H_j	Elements of the vector potential in a Helmholtz decomposition
A_n -mode	Antisymmetric Lamb-mode of n th order
S_n -mode	Symmetric Lamb-mode of n th order
$L(0, n)$ -mode	Axially symmetric longitudinal mode of n th order
$T(0, n)$ -mode	Axially symmetric torsional mode of n th order
$F(m, n)$ -mode	Flexural mode of m th circumferential and n th radial order
$\Delta k/k$	Relative error in wave numbers
O, P	Matrix operators in the linearized spectral decomposition
ψ_n, χ_n	Orthogonal bases in the spectral decomposition method
$\vec{\mathcal{X}}, \vec{\mathcal{Y}}$	Subvectors in the linearized spectral decomposition
\vec{U}, \vec{V}	Vectors of expansion coefficients in the spectral decomposition
K	Eigenvalues in the linearized spectral decomposition
N	Number of calculated modes
U_n, V_n	Expansion coefficients in the spectral decomposition
ϑ	Mixing angle of a mixed boundary condition
S_ϑ	Sine of the mixing angle of a mixed boundary condition
A, B, C, D	Spectral decomposition matrices
$A_{nm}, B_{nm}, C_{nm}, D_{nm}$	Elements of spectral decomposition matrices
F, G	Matrix operators in the multimodal method
\mathcal{I}_n	Normalization function used in the multimodal method
\mathcal{S}	Stress field at the waveguide's surface

\mathcal{U}, \mathcal{V}	Displacement fields at the waveguide's surface
\vec{a}, \vec{b}	Vectors of expansion coefficients in the multimodal method
\vec{X}, \vec{Y}	Subvectors in the multimodal method containing one stress and one displacement component
a_n, b_n	Expansion coefficients in the multimodal method
c_n^+, c_n^-	Coefficients of right and left going waves in the multimodal method
$\mathbf{N}_1, \mathbf{N}_2, \mathbf{N}_3, \mathbf{N}_4$	Matrices describing coupling and propagation of modes in the multimodal method
$N_{1,nm}, N_{2,nm}, N_{3,nm}, N_{4,nm}$	Elements of coupling and propagation matrices in the multimodal method
\mathbf{Z}	Impedance matrix
\mathbf{Z}_c	Characteristic impedance matrix
$Z_{c,n}$	Diagonal elements of the characteristic impedance matrix

Bibliography

- [1] H. Wüstenberg, A. Erhard, N. Bertus, T. Hauser, H. Hintze, and M. Schüßler, “Recent advances in ultrasonic inspection of railway -axles and - wheels,” *NDT.net*, vol. 6, no. 2, 2001.
- [2] P. Marty and G. Engl, “Latest development in the UT inspection of train wheels and axles,” in *18th World Conference on Nondestructive Testing*, 2012.
- [3] Z. Su, L. Ye, and Y. Lu, “Guided lamb waves for identification of damage in composite structures: a review,” *J. Sound Vib.*, vol. 295, pp. 753–780, 2006.
- [4] S. Banerjee, F. Ricci, E. Monaco, and A. Mal, “A wave propagation and vibration-based approach for damage identification in structural components,” *J. Sound Vib.*, vol. 322, pp. 167–183, 2009.
- [5] R. Gangadharan, D. Mahapatra, S. Gopalakrishnan, C. Murthy, and M. Bhat, “On the sensitivity of elastic waves due to structural damages: time-frequency based indexing method,” *J. Sound Vib.*, vol. 320, pp. 915–941, 2009.
- [6] A. Baltazar, C. Hernandez-Salazar, and B. Manzanares-Martinez, “Study of wave propagation in a multiwire cable to determine structural damage,” *NDT&E Int.*, vol. 43, pp. 726–732, 2010.
- [7] J. Prager, H. Gravenkamp, M. Rahman, and E. Köppe, “Einsatz geführter Wellen für die Ultraschallprüfung - Guided waves for non-destructive testing using ultrasound,” *Tech. Mess.*, vol. 79, no. 5, pp. 251–261, 2012.
- [8] J. Exner, “Simulation und Analyse der Ultraschallausbreitung in Hohlwellen,” master’s thesis (Diplomarbeit), Humboldt-Universität zu Berlin, Germany, Feb. 2012.
- [9] M. Grzeszkowski, “Entwurf eines Systems zur Strukturüberwachung von Eisenbahnradsatzwellen,” master’s thesis, Technische Universität Berlin, Germany, Oct. 2014.
- [10] M. Grzeszkowski and J. Prager, “Monitoring of the structural integrity of wheelset axles using guided waves,” in *7th European Workshop on Structural Health Monitoring*, 2014.
- [11] C. Fuller, “The effects of wall discontinuities on the propagation of flexural waves in cylindrical shells,” *J. Sound Vib.*, vol. 75, no. 2, pp. 207–228, 1980.

- [12] M. Perel, J. Kaplunov, and G. Rogerson, “An asymptotic theory for internal reflection in weakly inhomogeneous elastic waveguides,” *Wave Motion*, vol. 41, pp. 95–108, 2005.
- [13] C. Song and J. Wolf, “The scaled boundary finite-element method - alias consistent infinitesimal finite-element cell method - for elastodynamics,” *Comput. Methods Appl. Mech. Engrg.*, vol. 147, pp. 329–355, 1997.
- [14] J. Wolf and C. Song, “The scaled boundary finite-element method - a primer: derivations,” *Comput. Struct.*, vol. 78, pp. 191–210, 2000.
- [15] C. Song and J. Wolf, “The scaled boundary finite-element method - a primer: solution procedures,” *Comput. Struct.*, vol. 78, pp. 211–225, 2000.
- [16] H. Gravenkamp, *Numerical methods for the simulation of ultrasonic guided waves*. dissertation, Technischen Universität Carolo-Wilhelmina zu Braunschweig, 2014.
- [17] V. Pagneux and A. Maurel, “Lamb wave propagation in elastic waveguides with variable thickness,” *Proc. R. Soc. A*, vol. 462, pp. 1315–1339, 2006.
- [18] W. Bi, V. Pagneux, D. Lafarge, and Y. Aurégan, “Modelling of sound propagation in a non-uniform lined duct using a multi-modal propagation method,” *J. Sound Vib.*, vol. 289, pp. 1091–1111, 2006.
- [19] W. Bi and D. Lafarge, “Sound propagation in ducts lined with porous materials by a multi-modal marching method,” in *27th AIAA Aeroacoustics Conference*, 2006.
- [20] W. Bi, “Calculation of modes in circumferentially nonuniform lined ducts,” *J. Acoust. Soc. Am.*, vol. 123, no. 5, pp. 2603–2612, 2008.
- [21] W. Bi, V. Pagneux, D. Lafarge, and Y. Aurégan, “An improved multimodal method for sound propagation in nonuniform lined ducts,” *J. Acoust. Soc. Am.*, vol. 122, no. 1, pp. 280–290, 2007.
- [22] W. Bi, “On the calculation of modes in circumferentially nonuniform lined intakes,” in *28th AIAA Aeroacoustics Conference*, 2007.
- [23] V. Pagneux, “Multimodal admittance method in waveguides and singularity behavior at high frequencies,” *J. Comput. Appl. Math.*, vol. 234, pp. 1834–1841, 2010.
- [24] A. Maurel, J. Mercier, and V. Pagneux, “Improved multimodal admittance method in varying cross section waveguides,” *Proc. R. Soc. A*, vol. 470, no. 20130448, 2014.
- [25] J. Mercier and A. Maurel, “Improved multimodal methods for the acoustic propagation in waveguides with a wall impedance and a uniform flow,” in *22nd International Congress on Sound and Vibration*, 2015.
- [26] C. Kittel, *Einführung in die Festkörperphysik*. München: Oldenburg Verlag, 2006.

- [27] D. Royer and E. Dieulesaint, *Elastic waves in solids I: Free and guided propagation*. Heidelberg: Springer, 2000.
- [28] L. Pochhammer, “Ueber die Fortpflanzungsgeschwindigkeit kleiner Schwingungen in einem unbegrenzten isotropen Kreiscylinder,” *J. Reine Angew. Math.*, vol. 81, pp. 324–336, 1876.
- [29] C. Chree, “Longitudinal vibrations of a circular bar,” *Quar. Journ. Math.*, vol. 21, pp. 287–298, 1886.
- [30] H. Lamb, “On waves in an elastic plate,” *Proc. R. Soc. Lond. A*, vol. 93, pp. 114–128, 1917.
- [31] J. Zemanek, “An experimental and theoretical investigation of elastic wave propagation in a cylinder,” *J. Acoust. Soc. Am.*, vol. 51, no. 1, pp. 265–283, 1972.
- [32] D. Gazis, “Exact analysis of the plain-strain vibrations of thick-walled hollow cylinders,” *J. Acoust. Soc. Am.*, vol. 30, no. 8, pp. 786–794, 1958.
- [33] D. Gazis, “Three-dimensional investigation of the propagation of waves in hollow circular cylinders. I. Analytical foundation,” *J. Acoust. Soc. Am.*, vol. 31, no. 5, pp. 568–573, 1959.
- [34] D. Gazis, “Three-dimensional investigation of the propagation of waves in hollow circular cylinders. II. Numerical results,” *J. Acoust. Soc. Am.*, vol. 31, no. 5, pp. 573–578, 1959.
- [35] J. Greenspon, “Vibrations of a thick-walled cylindrical shell - comparison of the exact theory with approximate theories,” *J. Acoust. Soc. Am.*, vol. 32, no. 5, pp. 571–578, 1960.
- [36] J. Greenspon, “Axially symmetric vibrations of a thick cylindrical shell in an acoustic medium,” *J. Acoust. Soc. Am.*, vol. 32, no. 8, pp. 1017–1025, 1960.
- [37] J. Greenspon, “Vibrations of thick and thin cylindrical shells surrounded by water,” *J. Acoust. Soc. Am.*, vol. 33, no. 10, pp. 1321–1328, 1961.
- [38] J. Achenbach, *Wave Propagation in Elastic Solids*. North-Holland Publishing Company, 1973.
- [39] M. E.-C. E. Kettani, F. Luppé, and A. Gulliet, “Guided waves in a plate with linearly varying thickness: experimental and numerical results,” *Ultrasonics*, vol. 42, pp. 807–812, 2004.
- [40] V. Maupin, “Surface waves across 2-d structures: a method based on coupled local modes,” *Geophys. J. +*, vol. 93, pp. 173–185, 1988.

- [41] V. Galanenko, “On coupled modes theory of two-dimensional wave motion in elastic waveguides with slowly varying parameters in curvilinear orthogonal coordinates,” *J. Acoust. Soc. Am.*, vol. 103, no. 4, pp. 1752–1762, 1998.
- [42] V. Pagneux, N. Amir, and J. Kergomard, “A study of wave propagation in varying cross-section waveguides by modal decomposition. part i. theory and validation,” *J. Acoust. Soc. Am.*, vol. 100, no. 4, pp. 2034–2048, 1996.
- [43] V. Pagneux, N. Amir, and J. Kergomard, “A study of wave propagation in varying cross-section waveguides by modal decomposition. part ii. results,” *J. Acoust. Soc. Am.*, vol. 101, no. 5, pp. 2504–2517, 1997.
- [44] A. Puckett, *An experimental and theoretical investigation of axially symmetric wave propagation in thick cylindrical waveguides*. dissertation, University of Maine, 2004.
- [45] L. Tang and J. Cheng, “Numerical analysis on laser-generated guided elastic waves in a hollow cylinder,” *J. Nondestruct. Eval.*, vol. 21, no. 2, pp. 45–53, 2002.
- [46] C. Höhne, J. Prager, and H. Gravenkamp, “Computation of dispersion relations for axially symmetric guided waves in cylindrical structures by means of a spectral decomposition method,” *Ultrasonics*, vol. 63, pp. 54–64, 2015.
- [47] B. Pavlakovic, M. Lowe, D. Alleyne, and P. Cawley, *Disperse: A General Purpose Program for Creating Dispersion Curves*, pp. 185–192. Plenum Press, 1997.
- [48] F. Seco and A. Jiménez, *Modelling the Generation and Propagation of Ultrasonic Signals in Cylindrical Waveguides*, ch. 1. Intech Open Access Publisher, 2012.
- [49] M. Lowe, “Matrix techniques for modeling ultrasonic waves in multilayered media,” *IEEE T. Ultrason. Ferr.*, vol. 42, no. 4, pp. 525–542, 1995.
- [50] L. Gavric, “Finite element computation of dispersion properties of thin walled waveguides,” *J. Sound Vib.*, vol. 173, no. 1, pp. 113–124, 1994.
- [51] B. Mace, D. Duhamel, M. Brennan, and L. Hinke, “Finite element prediction of wave motion in structural waveguides,” *J. Acoust. Soc. Am.*, vol. 117, no. 5, pp. 2835–2843, 2005.
- [52] S. Sorohan, N. Constantin, and V. A. M. Găvan, “Extraction of dispersion curves for waves propagating in free complex waveguides by standard finite element codes,” *Ultrasonics*, vol. 51, pp. 503–515, 2011.
- [53] T. Hayashi, W. Song, and J. Rose, “Guided wave dispersion curves for a bar with an arbitrary cross-section, a rod and rail example,” *Ultrasonics*, vol. 41, pp. 175–183, 2003.
- [54] M. Mazzotti, A. Marzani, I. Bartoli, and V. E., “Guided wave dispersion analysis for prestressed viscoelastic waveguides by means of the SAFE method,” *Int. J. Solids Struct.*, vol. 49, pp. 2359–2372, 2012.

- [55] A. Marzani, E. Viola, I. Bartoli, F. L. di Scalea, and P. Rizzo, “A semi-analytical finite element formulation for modeling stress wave propagation in axisymmetric damped waveguides,” *J. Sound Vib.*, vol. 318, pp. 488–505, 2008.
- [56] I. Bartoli, A. Marzani, F. L. di Scalea, and E. Viola, “Modeling wave propagation in damped waveguides of arbitrary cross-section,” *J. Sound Vib.*, vol. 295, pp. 685–707, 2006.
- [57] M. Mazzotti, I. Bartoli, and V. E., “A coupled safe-2.5d bem approach for the analysis of damped leaky guided waves in embedded waveguides of arbitrary cross-section,” *Ultrasonics*, vol. 53, pp. 1227–1241, 2013.
- [58] H. Gravenkamp, H. Man, C. Song, and J. Prager, “The computation of dispersion relations for three dimensional elastic waveguides using the scaled boundary finite element method,” *J. Sound Vib.*, vol. 332, pp. 3756–3771, 2013.
- [59] H. Gravenkamp, C. Song, and J. Prager, “A numerical approach for the computation of dispersion relations for plate structures using the scaled boundary finite element method,” *J. Sound Vib.*, vol. 331, pp. 2543–2557, 2012.
- [60] H. Gravenkamp, C. Birk, and C. Song, “The computation of dispersion relations for axisymmetric waveguides using the scaled boundary finite element method,” *Ultrasonics*, vol. 54, pp. 1373–1385, 2014.
- [61] H. Gravenkamp, F. Bause, and C. Song, “On the computation of dispersion curves for axisymmetric elastic waveguides using the scaled boundary finite element method,” *Comput. Struct.*, vol. 131, pp. 46–55, 2014.
- [62] V. Pagneux and A. Maurel, “Determination of lamb mode eigenvalues,” *J. Acoust. Soc. Am.*, vol. 110, no. 3, pp. 1307–1317, 2001.
- [63] A. Adamou and R. Craster, “Spectral methods for modelling guided waves in elastic media,” *J. Acoust. Soc. Am.*, vol. 116, no. 3, pp. 1524–1535, 2004.
- [64] C. Chapman and S. Sorokin, “The finite-product method in the theory of waves and stability,” *Proc. R. Soc. A*, vol. 466, pp. 471–491, 2010.
- [65] V. Pagneux and A. Maurel, “Scattering matrix properties with evanescent modes for waveguides in fluids and solids,” *J. Acoust. Soc. Am.*, vol. 116, no. 4, pp. 1913–1920, 2004.
- [66] M. Razzaghi, “A computational solution for a matrix riccati differential equation,” *Numer. Math.*, vol. 32, pp. 271–279, 1979.
- [67] G. Freiling, “A survey of nonsymmetric riccati equations,” *Linear Algebra Appl.*, vol. 351-352, pp. 243–270, 2002.
- [68] C. Garret and R. Li, “Gip integrators for matrix riccati differential equations,” *Appl. Math. Comput.*, vol. 241, pp. 283–297, 2014.

- [69] J. Schiff and S. Shnider, “A natural approach to the numerical integration of riccati differential equations,” *SIAM J. Numer. Anal.*, vol. 36, pp. 1392–1413, 1999.
- [70] A. Iserles, A. Marthinsen, and S. N. rsett, “On the implementation of magnus series for linear differential equations,” *BIT Numer. Math.*, vol. 39, no. 2, pp. 281–304, 1999.
- [71] C. Moler and C. van Loan, “Nineteen dubious ways to compute the exponential of a matrix, twenty-five years later,” *SIAM Rev.*, vol. 45, no. 1, pp. 3–49, 2003.
- [72] G. Teschl, “Ordinary differential equations and dynamical systems,” 2012. <http://www.mat.univie.ac.at/~gerald/ftp/book-ode/ode.pdf> 364 pages, last accessed: 22.08.2014.
- [73] W. Rosenheinrich, “Table of some indefinite integrals of bessel functions,” April 2014. <http://www.fh-jena.de/rsh/Forschung/Stoer/besint.pdf> 291 pages, last accessed: 19.08.2014.
- [74] C. Höhne and J. Prager, “Simulation of ultrasound propagation in waveguides with non-constant thickness by a multimodal approach,” in *7th Forum Acusticum*, 2014.
- [75] C. Höhne and J. Prager, “Multimodal method for the simulation of guided wave propagation in cylindrical rods with varying cross-section,” in *22nd International Congress on Sound and Vibration*, 2015.

List of publications from this work

- P1** C. Höhne and J. Prager, “Simulation of ultrasound propagation in waveguides with non-constant thickness by a multimodal approach,” in 7th Forum Acusticum, 2014.
- P2** C. Höhne and J. Prager, “Multimodal method for the simulation of guided wave propagation in cylindrical rods with varying cross-section,” in 22nd International Congress on Sound and Vibration, 2015.
- P3** C. Höhne, J. Prager, and H. Gravenkamp, “Computation of dispersion relations for axially symmetric guided waves in cylindrical structures by means of a spectral decomposition method,” *Ultrasonics*, vol. 63, pp. 54-64, 2015.

List of Figures

1.1	General layout of a wheelset-axle as used in trains.	4
2.1	Illustration of displacements in a) symmetric Lamb-modes (<i>S</i> -modes) and b) antisymmetric Lamb-modes (<i>A</i> -modes).	10
2.2	Multimodal approach at a transition between different cross-sections.	17
2.3	Complex dispersion curves of a) symmetric and b) antisymmetric Lamb-modes in an isotropic homogeneous plate.	22
2.4	Real dispersion curves of symmetric and antisymmetric Lamb-modes in an isotropic homogeneous plate as plot of phase velocities over frequency thickness product.	23
3.1	Section of the real parts of dispersion curves in a plate with a) regular and b) irregular Cutoffs.	36
3.2	Implementation of pulse propagation including a) modelling of an excitation pulse, b) reducing the spectrum to a finite number of frequencies and c) reconstructing the pulse excitation as superposition of continuous wave solutions.	38
3.3	Displacement field in <i>x</i> -direction for $\omega = 0.5$ MHz with red for positive and blue for negative displacement.	39
3.4	Displacement field in <i>x</i> -direction for $\omega = 1.37$ MHz with red for positive and blue for negative displacement.	39
3.5	Displacement field in <i>x</i> -direction for $\omega = 1.5$ MHz with red for positive and blue for negative displacement.	40
4.1	Cylindrical rod with varying thickness.	47
4.2	Hollow cylinder with varying thickness.	50
5.1	Dispersion curves for real valued wave numbers corresponding to a plate with symmetrically varying thickness for an excitation frequency of $\omega = 0.5$ MHz.	56
5.2	Displacement field in <i>x</i> -direction in a plate with symmetrically varying thickness for an excitation frequency of $\omega = 0.5$ MHz simulated with a) multimodal method and b) COMSOL with red for positive and blue for negative displacement.	57

5.3	Dispersion curves for real valued wave numbers corresponding to a plate with symmetrically varying thickness for an excitation frequency of $\omega = 1.37$ MHz.	57
5.4	Displacement field in x -direction in a plate with symmetrically varying thickness for an excitation frequency of $\omega = 1.37$ MHz simulated with a) multimodal method and b) ANSYS with red for positive and blue for negative displacement.	58
5.5	Dispersion curves for real valued wave numbers corresponding to a plate with symmetrically varying thickness for an excitation frequency of $\omega = 1.5$ MHz.	58
5.6	Displacement field in x -direction in a plate with symmetrically varying thickness for an excitation frequency of $\omega = 1.5$ MHz simulated with a) multimodal method and b) ANSYS with red for positive and blue for negative displacement.	59
5.7	Dispersion curves for real valued wave numbers corresponding to a plate with asymmetrically varying thickness for an excitation frequency of $\omega = 0.5$ MHz.	60
5.8	Displacement field in x -direction in a plate with asymmetrically varying thickness for an excitation frequency of $\omega = 0.5$ MHz simulated with a) multimodal method and b) COMSOL with red for positive and blue for negative displacement.	60
5.9	Dispersion curves for real valued wave numbers corresponding to a cylindrical rod with varying thickness for an excitation frequency of $\omega = 1.25$ MHz.	61
5.10	Displacement field in r -direction in a cylindrical rod with varying thickness for an excitation frequency of $\omega = 1.25$ MHz simulated with a) multimodal method and b) ANSYS with red for positive and blue for negative displacement.	62
5.11	Dispersion curves for real valued wave numbers corresponding to a cylindrical rod with varying thickness for an excitation frequency of $\omega = 2.5$ MHz.	62
5.12	Displacement field in r -direction in a cylindrical rod with varying thickness for an excitation frequency of $\omega = 2.5$ MHz simulated with a) multimodal method and b) ANSYS with red for positive and blue for negative displacement.	63
5.13	Dispersion curves for real valued wave numbers corresponding to a cylindrical rod with varying thickness for an excitation frequency of $\omega = 2.75$ MHz.	63
5.14	Displacement field in r -direction in a cylindrical rod with varying thickness for an excitation frequency of $\omega = 2.75$ MHz simulated with a) multimodal method and b) ANSYS with red for positive and blue for negative displacement.	64

5.15	Dispersion curves for real valued wave numbers corresponding to a cylindrical rod with varying thickness for an excitation frequency of $\omega = 3.75$ MHz.	64
5.16	Displacement field in r -direction in a cylindrical rod with varying thickness for an excitation frequency of $\omega = 3.75$ MHz simulated with a) multimodal method and b) ANSYS with red for positive and blue for negative displacement.	65
5.17	Dispersion curves of the cylindrical rod with varying radius for an excitation frequency of $\omega = 3.75$ MHz split into a) real part and b) imaginary part of the wave numbers plotted over frequency-radius product.	65
5.18	Dispersion curves for real valued wave numbers corresponding to a hollow cylinder with varying outer radius for an excitation frequency of $\omega = 0.95$ MHz.	67
5.19	Displacement field in r -direction in a hollow cylinder with varying outer radius for an excitation frequency of $\omega = 0.95$ MHz simulated with a) multimodal method and b) ANSYS with red for positive and blue for negative displacement.	67
5.20	Dispersion curves for real valued wave numbers corresponding to a hollow cylinder with varying outer radius for an excitation frequency of $\omega = 1.55$ MHz.	68
5.21	Displacement field in r -direction in a hollow cylinder with varying outer radius for an excitation frequency of $\omega = 1.55$ MHz simulated with a) multimodal method and b) ANSYS with red for positive and blue for negative displacement.	68
5.22	Dispersion curves for real valued wave numbers corresponding to a hollow cylinder with varying outer radius for an excitation frequency of $\omega = 2.2$ MHz.	69
5.23	Displacement field in r -direction in a hollow cylinder with varying outer radius for an excitation frequency of $\omega = 2.2$ MHz simulated with a) multimodal method and b) ANSYS with red for positive and blue for negative displacement.	69
6.1	Inner radius and various values for the thickness of wheelset-axles.	75

List of Tables

5.1	Computation times for the simulation of S_0 pulse propagation through plates.	70
5.2	Computation times for the simulation of $L(0, 0)$ pulse propagation through cylindrical rods.	71